DETERMINATION OF THE EQUIVALENT STRESS-STRAIN CURVES OF DUCTILE METALS THROUGH IMAGE ANALYSIS

A Thesis Submitted to
the Graduate School of
İzmir Institute of Technology
in Partial Fulfillment of the Requirements for the Degree of

MASTER OF SCIENCE

in Mechanical Engineering

by
Mehmet ÇAKMAK

June 2024
İZMİR

We approve the thesis of **Mehmet ÇAKMAK**

Examining Committee Members:

Prof. Dr. Mustafa GÜDEN
Department of Mechanical Engineering, İzmir Institute of Technology

Prof. Dr. Hasan YILDIZ
Department of Mechanical Engineering, Ege University

Asst. Prof. Dr. Halil TETİK
Department of Mechanical Engineering, İzmir Institute of Technology

12 June 2024

Prof. Dr. Mustafa GÜDEN
Advisor, Department of Mechanical Engineering
İzmir Institute of Technology

Prof. Dr. Alper TAŞDEMİRCİ
Co-Advisor, Department of Mechanical Engineering
İzmir Institute of Technology

Prof. Dr. M. İ. Can DEDE
Head of the Department of Mechanical Engineering
İzmir Institute of Technology

Prof. Dr. Mehtap EANES
Dean of the Graduate School
İzmir Institute of Technology

ACKNOWLEDGEMENTS

Firstly, I would like to extend my heartfelt thanks to my advisor, Prof. Mustafa GÜDEN, for his technical insights, practical approaches, and encouraging guidance throughout my master's study. I am grateful to him for allowing me to join his research team and for his contributions to both my personal and professional development. It is a great honor to have him as my advisor and to work alongside him. Secondly, thank to my co-advisor Prof. Dr. Alper TAŞDEMİRCİ for his supports. I am also thankful to TUBITAK (Scientific and Technical Council of Turkey) and 1505 – University-Industry Cooperation Support Program for support of the study.

Thirdly, I would like to thank all the members of Dynamic Testing and Modeling Laboratory, IZTECH for the positive work atmosphere and memorable times. Thanks to all members of the Dynamic Testing and Modelling Laboratory: Fakı Murat YILDIZTEKİN, Gülden ÇİMEN, Hacer İrem ERTEN KAPLAN, İbrahim Berk AKDOĞAN, Seven Burçin ÇELLEK, Samedhan YILDIIM, Mehmet Yalçın SIRMALILAR, Hamza GÜNGÖR, Arslan BIN RIAZ, and Mian IMRAN for their endless support and collaboration.

Lastly, I would like to express my deepest gratitude to my family for their unwavering support and love throughout my master's journey. My family has been my greatest source of strength with their belief in me and their emotional support during my entire educational journey. It is thanks to their presence, love, and sacrifices that I have reached this point. I will always strive to make them proud.

ABSTRACT

DETERMINATION OF THE EQUIVALENT STRESS-STRAIN CURVES OF DUCTILE METALS THROUGH IMAGE ANALYSIS

This thesis presents a methodology for determining the equivalent stress-strain and the failure strain-stress triaxiality curves of ductile metallic materials using the advanced computing and image analysis methods. The determined curves were then used to calculate the parameters of the Johnson and Cook (JC) flow stress and damage models. A code was developed in Python to perform the numerical calculations and image analysis using the Python's libraries and image analysis tools. The main entries to the code were the experimental force-displacement curves at different strain rates, the experimental failure strain-stress triaxiality curve at a reference quasi-static strain rate, the experimental failure strain-strain rate curve at a constant stress triaxiality and the video images of the deforming test specimens. The correctness and reliability of the developed code in predicting the equivalent stress-strain curves and the parameters of the JC flow stress and damage models were clearly demonstrated for the selected 316L and AISI 4340 alloys. The code could also be easily adopted to other well-now constitutive equations commonly used in the finite element software. Finally, the results of present study contribute to the field of mechanical engineering by providing a robust tool for the materials characterization essential for designing and optimizing engineering components subjected to complex states of stresses.

Keywords: Bridgman Correction, MLR Correction, Python, 316L, AISI 4340, Mechanical Properties, Johnson-Cook Strength Model, Johnson-Cook Damage Model

ÖZET

SÜNEK METALLERİN EŞDEĞER GERİLME-GERİNİM EĞRİLERİNİN GÖRÜNTÜ ANALİZİ YOLUYLA BELİRLENMESİ

Bu tez ileri hesaplama ve görüntü analiz teknikleri kullanarak sünek metallerin eşdeğer gerilim-gerinim ve kırılma gerinimi-üç eksenli gerilme eğrilerini belirlemek için yeni bir metodoloji sunmaktadır. Belirlenen eğriler daha sonra Johnson-Cook (JC) gerilme ve hasar denklemleri parametrelerini belirlemek için kullanılmıştır. Tüm numerik hesaplamalar ve görüntü analizi Python Kütüphanesi ve görüntü analiz araçları kullanılarak yapılmıştır. Kodun ana gidileri deneysel farklı gerinin hızlardaki kuvvet-deplasman verileri, statik kırılma gerinimi-üç eksenli gerilme verileri, farklı gerinim hızlarındaki kırılma gerinimi verileri ve kırılma test numunesinin deformasyon görüntü videolardır. Kullanılan metodoloji eşdeğer gerilim-gerinim eğrilerini ve JC gerilme ve hasar denklemleri parametrelerini tahmin etmekteki doğruluğu ve etkinliği 316L ve AISI 4340 alaşımları için açıkça gösterilmiştir. Geliştirilen kod yapısal analizde kullanılan sonlu elaman yazılımlarında kullanılan birçok yapısal denkleme de kolayca uygulanabilmektir. Son olarak, bu çalışma hassas malzeme özelliklerinin performans ve güvenlik açısından kritik olduğu çeşitli mühendislik alanlarındaki potansiyel uygulamalarla birlikte, sünek metallerin mekanik davranışını anlamak ve tahmin etmek için kapsamlı bir yaklaşım sunmaktadır.

Anahtar Kelimeler: Bridgman Düzeltmesi, MLR Düzeltmesi, Python, 316L, AISI 4340, Mekanik Özellikler, JC Mukavemet Modeli, JC Hasar Modeli

TABLE OF CONTENTS

LIST OF FIGURES

Figure **Page**

Figure **Page**

Figure **Page**

Figure **Page**

Figure **Page**

Figure **Page**

LIST OF TABLES

Table **Page**

CHAPTER 1

INTRODUCTION

The fidelity of the finite element models used to predict the response of structures against external loads depends on the correctness of the material flow stress and damage models implemented in the models. Both, the flow stress and damage model parameters, are extracted from the experimental stress-strain curves and fracture strains through curve fittings. A flow stress model, also called a constitutive equation, defines the material stress as functions of strain, strain rate and temperature. As will be given in the following chapters, there have been significant variations between the material model parameters of the same alloy reported in the literature. These variations are believed due to partly the errors involved in the curve fittings to the experimental data. The curve fittings include the calculation of the Bridgman correction factor, average stresses and strains, fracture strains, strain rate sensitivity parameters and etc. The automation of data processing will definitely reduce the extent of these errors/variations arising from the human factor.

The calculations of the Bridgman correction factor (B) given in Equation 2.21 require an accurate measurement of the R value (the radius of curvature of necking), and an accurate measurement of the value of a (the radius of curvature of necking). The measurements of the values of R and a are usually made from the video records of deformed sample in an image analysis program. The variations in between the measurements of different users are therefore quite common. On the other side, the determination of the Johnson and Cook (JC) flow stress and damage parameters involves several different curve fittings. The fittings are performed using a graphic program while the data read from the curves are entered by the user. As will be elaborated later, several steps are needed to obtain the material equation parameters. All these fittings are prone to the variations in the determined parameters between the different users.

The main aim of this thesis is to develop a computer code to determine the Bridgman's correction factor, equivalent stress-strain curves and the JC flow stress and damage model parameters. In this way, the effect of human factor is tried to be eliminated in the data processing stage. A library of the JC parameters of common engineering materials was also included in the code. The correctness and reliability of the used

methodology (a code) in predicting equivalent stress-strain curves and the JC flow stress and damage model parameter were investigated for the selected 316L and AISI 4340 alloys. The developed code could also be easily adopted to other constitutive equations widely used in the finite element software for the structural analysis.

The content of the thesis is as follows. In the first chapter, a background is given on the standard tension test and the calculations of stress and strain and the Bridgman correction factor, both of which are used to calculate the equivalent stresses. In the second chapter, the details of the JC flow stress and damage models and their parameter calculations are presented. Chapter 3 explains the experimental techniques for testing 316L and AISI 4340 alloys and the numerical methodology used in the calculations. The code interface design is explained in Chapter 4. Chapter 5 compares the results of experimentally and numerically determined material model parameters for the selected two alloys. And, the conclusions are made in Chapter 6.

CHAPTER 2

LITERATURE REVIEW

2.1. Tension Test Method

Tension test is usually used to assess the mechanical properties of materials under uniaxial loading conditions. In this test, a test specimen is inserted between the grips of a tension test machine. The test machine mainly consists of two frames, a moving cross-head and a load cell as seen in Figure 2.1. The test specimen is usually fixed at its lower end (bottom) and pulled from the upper end by the upward motion of the cross-head. The cross-head speed presented by the letter of c in Figure 2.1 determines the displacement rate of the test specimen. In a constant cross-head speed test machine, the load on test specimen is measured by the load cell. Both time (t) and force (F) values are recorded in the test and the displacement (ΔL), also called stroke, is calculated from the following relation, $\Delta L = ct$. The calculated displacement (total displacement) is included both the specimen and machine displacement, $\Delta L_{specimen} + \Delta L_{machine}$ (the test machine is also extended during the specimen extension). The accurate strain measurement of the test specimen hence requires a separate, external measurement from the test specimen. Common methods of the external strain measurement include the use of strain gages, clip-on extensometers and video extensometers. Strain gages are glued onto the surface of test specimen while a video extensometer detects the displacement from the markers deliberately placed on the test specimen surface.

The load cell is a critical component and usually placed above the specimen (Figure 2.1). It converts the mechanical force into an electrical signal, which can then be read and recorded. The precision of load cell directly affects the accuracy of the stress calculations. The moving cross-head is typically driven by a motor and a series of gears or hydraulics that allow for the precise control of the speed and extent of the movement. This controlled movement provides a constant strain rate during test. Standard size test specimens are usually used in the tension test, including round, sheet and plate-like specimens. The ASTM E8M “Standard Test Methods for Tension Testing of Metallic

Materials" defines the tension test specimen geometries and dimensions for metallic materials [1] . The ASTM E8M test specimen geometry and dimensions of round dog-bone specimens are seen in Figure 2.2. In the same figure, *G* is the gage length, *D* is the diameter and *R* is the radius of the fillet of test specimen. The use of a standard test specimens size confirms the validity of tests.

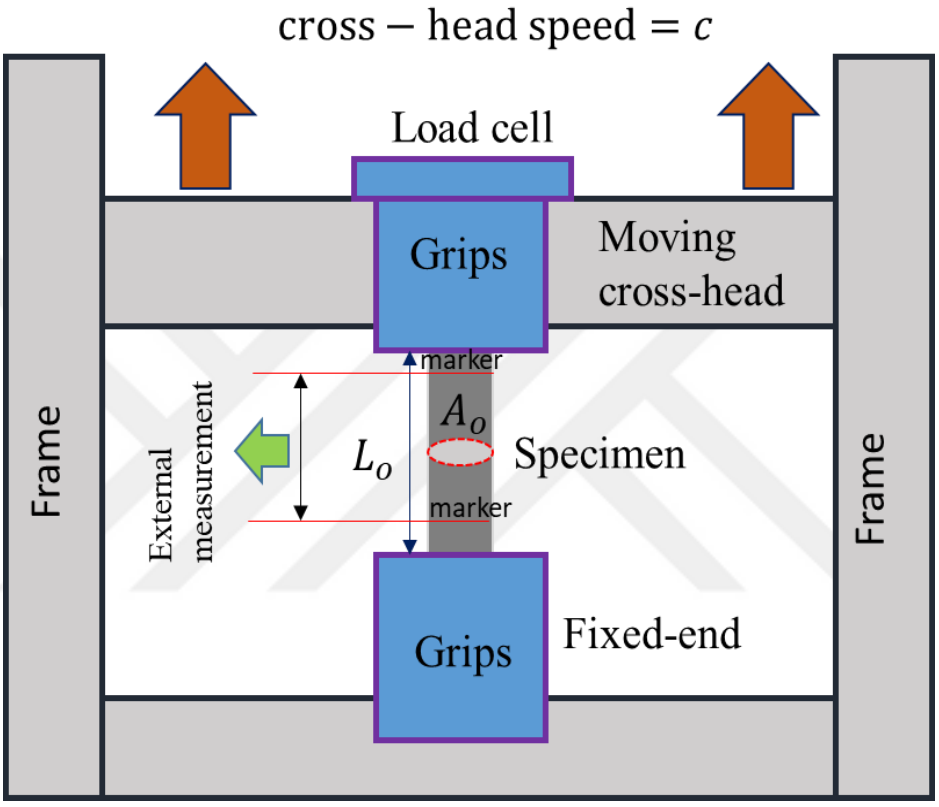

Figure 2.1. A schematic of tensile test machine and test specimen

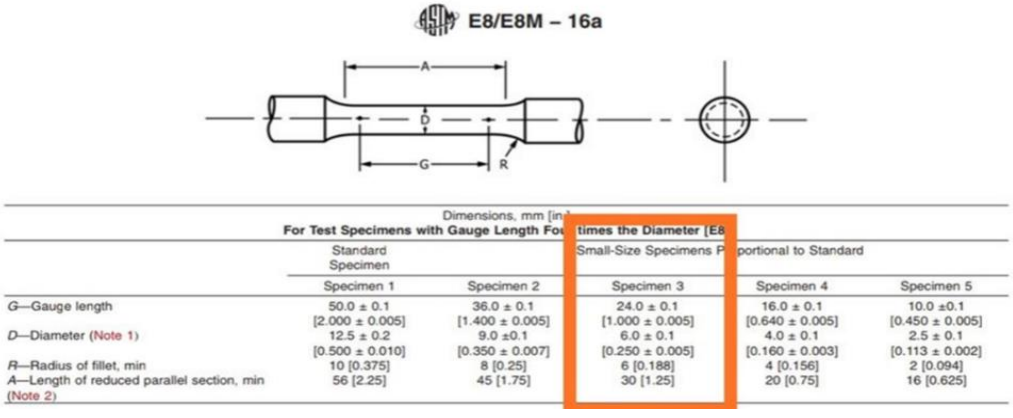
E8/E8M – 16a

Dimensions, mm [in.]

	For Test Specimens with Gauge Length Fo times the Diameter [E8				
	Standard Specimen		Small-Size Specimens P portional to Standard		
	Specimen 1	Specimen 2	Specimen 3	Specimen 4	Specimen 5
G—Gauge length	50.0 ± 0.1 [2.000 ± 0.005]	36.0 ± 0.1 [1.400 ± 0.005]	24.0 ± 0.1 [1.000 ± 0.005]	16.0 ± 0.1 [0.640 ± 0.005]	10.0 ±0.1 [0.450 ± 0.005]
D—Diameter (Note 1)	12.5 ± 0.2 [0.500 ± 0.010]	9.0 ±0.1 [0.350 ± 0.007]	6.0 ± 0.1 [0.250 ± 0.005]	4.0 ± 0.1 [0.160 ± 0.003]	2.5 ± 0.1 [0.113 ± 0.002]
R—Radius of fillet, min	10 [0.375]	8 [0.25]	6 [0.188]	4 [0.156]	2 [0.094]
A—Length of reduced parallel section, min (Note 2)	56 [2.25]	45 [1.75]	30 [1.25]	20 [0.75]	16 [0.625]

Figure 2.2. Round dog-bone test specimen dimensions based on ASTM E8M [1]

The engineering stress (S) in a tension test is

$$S = \frac{F}{A_o} \tag{2.1}$$

where A_o is the initial cross-sectional area of test specimen. Similarly, the engineering strain (e), a dimensionless quantity representing the deformation, is calculated as

$$e = \frac{l_i - l_o}{l_0} = \frac{\Delta l}{l_0} \tag{2.2}$$

Here, l_i is the instantaneous length and l_o is the initial length of test specimen. Materials exhibit different stress-strain behaviors under tensile loads. A room temperature engineering stress-strain curve of a common ductile engineering metal (stainless steel 316L) at a quasi-static strain rate is shown in Figure 2.3, together with the deformation pictures of the test specimen at different strains. Until the yield point (at which the plastic deformation starts) the deformation is assumed to be elastic (Figure 2.3). Elastic deformation is a reversible process; the test specimen under load recovers its original shape when the applied load is released. Most materials including metals and ceramics obey the Hooke's Law in the elastic region. According to this law, strain is linearly proportional to stress as

$$S = Ee \tag{2.3}$$

where E denotes the modulus of elasticity or elastic modulus. A magnified elastic region of the curve shown in Figure 2.3 is further depicted in Figure 2.4. As shown in the same figure, the elastic modulus is determined as the slope of the curve in the elastic region. The yield point is determined using two methods. In the first method, a tangent line is drawn to the linear region and the intercept of this line with the stress-strain curve gives the proportional limit. In the second method, a parallel line is drawn to the initial slope at a strain of *0.002* and the intercept of this line with the curve gives the offset strength. Note that the transition from the linear elastic to plastic deformation is gradual and the lower limit of stress is not sharply defined. After yielding, it is assumed that the plastic deformation starts. In the plastic region, the specimen deforms homogeneously until the

maximum stress. The homogeneous or uniform deformation is that the decrease in the diameter of test specimen as the length increases is the same along the test specimen length. At the maximum stress, the deformation starts to localize in a section of the test specimen and a necked region is formed (Figure 2.3). Thereafter, the deformation proceeds at the necked region and the stress values decrease after necking until the fracture as seen in Figure 2.3. Necking phenomenon is also observed in plate-like flat test specimens as depicted in Figure 2.5.

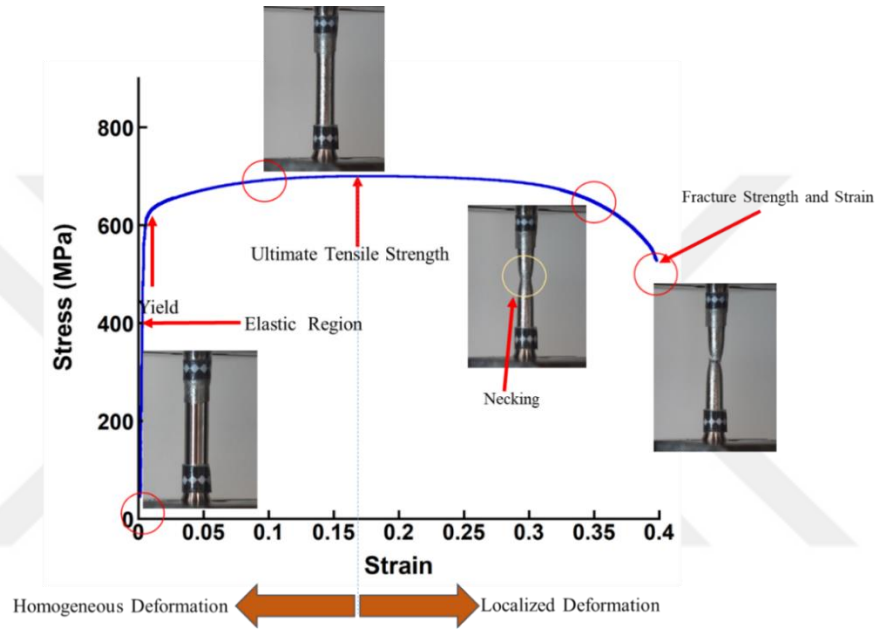

Figure 2.3. A tensile stress-strain curve of 316L, following a linear elastic deformation the specimen shows a large plastic deformation by forming a necking

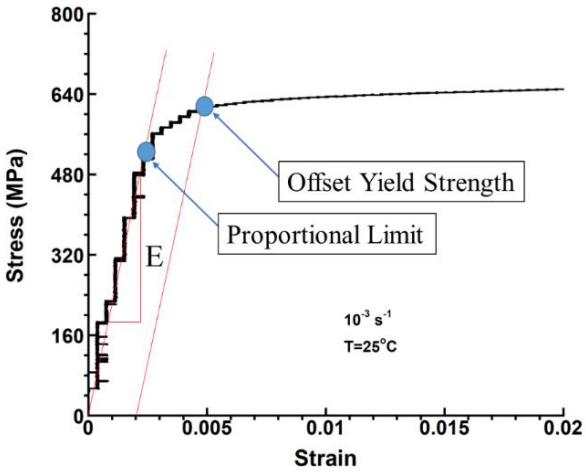

Figure 2.4. Magnified elastic region of the stress-strain curve in Figure 2.3.

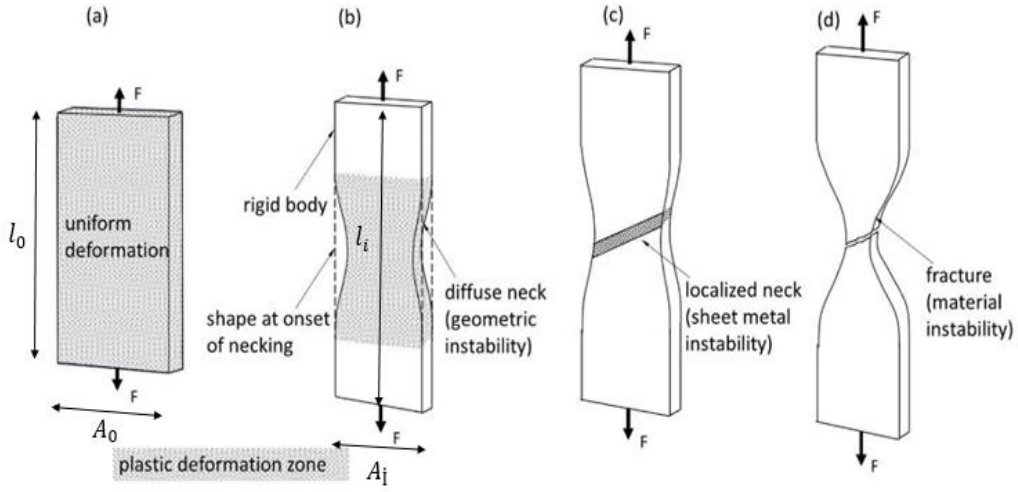

Figure 2.5. Tensile test phases in a flat specimen: (a) uniform deformation, (b) geometric instability, (c) localized necking and (d) cracking (Source: Cacko, R. et al., 2005 [2])

The initial cross-sectional area decreases while the length increases in the uniform deformation region. Hence, the sample cross-sectional area (A_i) and the sample length (l_i) are different from the initial measurements. Due to the reduction in cross-sectional area during tensile testing, the material experiences a higher actual or true stress than engineering stress calculated using the initial area. True stress (σ) is calculated as

$$\sigma = \frac{F}{A_i} \tag{2.4}$$

Engineering stress and strain are adequate for describing the material behavior up to the yield point, but beyond yielding, true stress and strain become more representative of the material response. In the calculation of true strain (ε), ach small extension (δl) is divided by the instantaneous length (l_i) at which that extension occurs. As the specimen elongates and the gage length increases, each subsequent calculation of strain uses the new elongated length as

$$\varepsilon = \frac{\delta l}{l_0} + \frac{\delta l}{l_1} + \frac{\delta l}{l_2} + \cdots = \sum_i \left(\frac{\delta l}{l_i}\right) \tag{2.5}$$

where $l_1 = l_0 + \delta l$, $l_1 = l_0 + \delta l$, and so forth. The differential form of the equation is

$$d\varepsilon = \frac{dl}{l} \tag{2.6}$$

Integrating this expression from an initial length of l_0 to a final length of l_i gives true strain as

$$\varepsilon = ln(\frac{l_i}{l_0}) \tag{2.7}$$

Above equation characterizes true strain as the natural logarithm of the ratio of the instantaneous length to the original length. Given that the deformation is uniform along the gage length, and assuming volume constancy ($A_0 l_0 = A_i l_i$), Equation (2.4) can be rearranged to relate engineering stress to true stress as

$$\sigma = \frac{F}{A_i} = \frac{F}{A_0}\frac{A_0}{A_i} = S(\frac{A_0}{A_i}) \tag{2.8}$$

Equation (2.8) highlights that true stress is always greater than engineering stress because A_i decreases as the material is stretched, making $\frac{A_0}{A_i}$ greater than 1. The ratio $\frac{A_0}{A_i}$ can be related to the true strain by considering the uniform strain condition. If $l_i = l_0 + \Delta L$, and assuming volume constancy, the ratio of the areas can be expressed as

$$\frac{A_0}{A_i} = \frac{l_i}{l_0} = [1 + (\Delta l / l_0)] \tag{2.9}$$

Given that engineering strain (e) is $\Delta l / l_0$, we can link true stress to engineering stress and strain as

$$\sigma = S(1 + e) \tag{2.10}$$

The true stress exceeds engineering stress for tensile tests because the strain (e) is positive. Conversely, if the material are compressed, the strain is negative (since $e<0$),

and the engineering stress is greater than the true stress. True strain is defined logarithmically as

$$\varepsilon = \ln(1 + e) \tag{2.11}$$

indicating a natural logarithmic relationship with the engineering strain.

Equation (2.11) further elucidates the relationship between true strain and engineering strain, specifically for the conditions of uniform gage length deformation often seen in tensile testing. This relationship implies that, for small strains typically encountered in the elastic deformation phase, true strain and engineering strain are approximately equal because the logarithm of a value close to one ($1 + x$, where x is a small number) is approximately x itself. However, as the material undergoes plastic deformation and the strains become larger, the difference between true and engineering strains becomes more pronounced.

The stress-strain curve, typically depicted in engineering stress and strain terms, shows that the engineering stress reaches a maximum at the strain e_{UTS}, which is known as the ultimate tensile strength (UTS) as shown in Figure 2.3. This point on the curve represents the maximum engineering stress the material can sustain. Beyond the ultimate tensile strength, continued straining leads to a reduction in the applied force required to continue deforming the material. As necking progresses, the cross-sectional area of the material at the neck decreases, which is not accounted for in the calculation of engineering stress, hence the observed decrease in force. True stress, on the other hand, continues to increase with strain since it is based on the actual cross-sectional area, which is decreasing during the necking process as depicted in Figure 2.6. The necking phenomenon is characterized by a reduction in the load-carrying area, while the true stress (based on the actual, reduced area at the neck) continues to increase until failure. In cylindrical bars or tensile specimens, necking manifests as a distinct narrowing of the specimen, as shown in Figure 2.3 and Figure 2.6.

As the material undergoes plastic deformation, particularly during necking, the deformation becomes highly non-uniform. In this stage, engineering stress and strain, which are based on the original cross-sectional area and gage length, are no longer accurate representations of the material behavior. The true stress after necking can then be estimated as

$$\sigma = \frac{\mathrm{F}}{A_i} \tag{2.12}$$

True strain is calculated as

$$\varepsilon = ln\left(\frac{A_0}{A_i}\right) \tag{2.13}$$

The calculations of true and engineering stresses and strains in the tension stress-strain curve are shown in Figure 2.7.

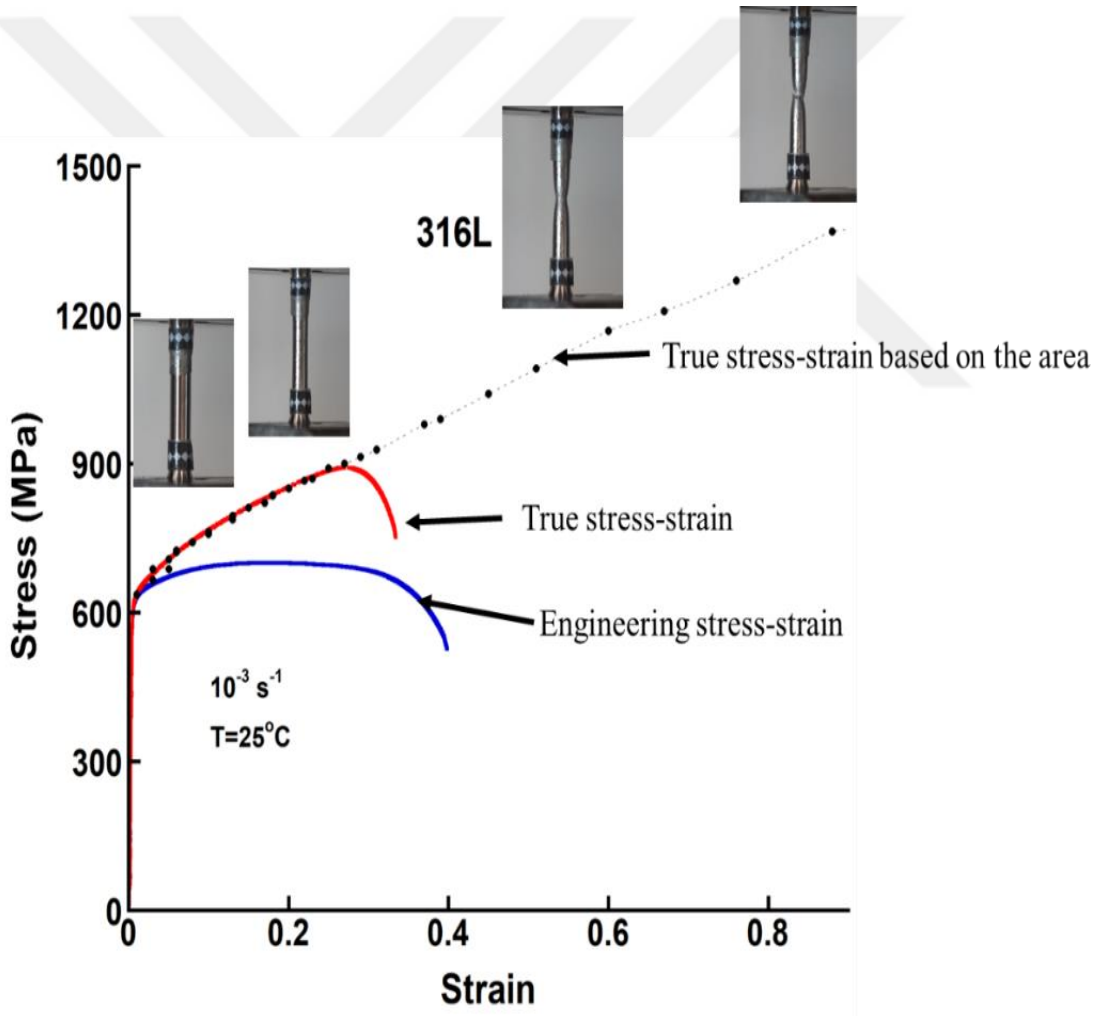

Figure 2.6. The tensile stress-strain curve of 316L, engineering and true-stress-strain curves

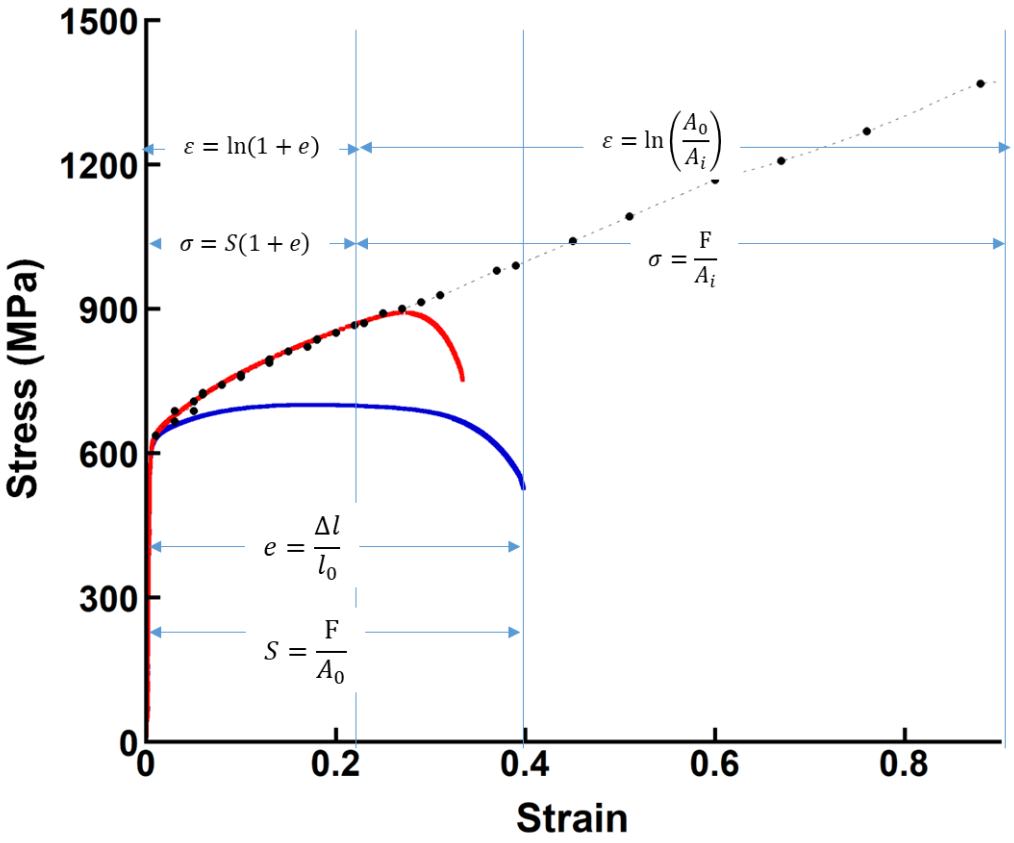

Figure 2.7. Calculations of true and engineering stress and strains

For plastic deformation, empirical equations are often employed to describe the flow behavior. One of the most widely used empirical formulations to describe the plastic deformation behavior of solids is the strain-hardening equation

$$\sigma = K\boldsymbol{\varepsilon^n} \tag{2.14}$$

where *K* is the strength coefficient, and *n* is the strain-hardening coefficient. This equation captures the relationship between stress and strain in the plastic region of deformation. The strain-hardening coefficient is indicative of how much additional stress is required to produce subsequent deformation in the material. A higher value of *n* signifies a strong work-hardening response, meaning the material will exhibit significant increase in the strength with plastic deformation. The strength coefficient is a scaling factor that represents the true stress necessary to produce a unit true strain (when $\varepsilon = 1$) [3].

2.2. The Bridgman's Correction

The state of the stress after necking is tri-axial (3D). The emergence of necking generates radial and tangential stresses, which in turn elevate the longitudinal stress needed to sustain plastic deformation[4]. The Bridgman's [5] method is used to determine the equivalent stress (σ_e) after necking. Before necking, σ_e=σ_{Avg}; where σ_{Avg} is the average stress in the long axis (z) and is

$$\sigma_{Avg} = \frac{F}{A_n} \tag{2.15}$$

where A_n is the smallest area in the necking region. The Bridgman formulation is based on an assumption that the strain distribution is homogeneous in the minimum cross-sectional area. The minimum cross-section is the section of the material that undergoes the most significant thinning during necking. Figure 2.8 is a schematic representation of a necking in a smooth round bar under tensile stress. In the same figure, σ_r is the radial, σ_θ is the hoop and σ_z is the axial stresses in the necking, a is the radius of the cross-sectional area of the neck; and R is the local radius of the neck. The radial, hoop and axial stresses of a round specimen sequentially are given as [5]

$$\sigma_r = \sigma_\theta = \frac{\sigma_{Avg}}{(1+\frac{2R}{a})}\left(\frac{ln\left(\frac{a^2+2aR-r^2}{2aR}\right)}{ln(1+\frac{2R}{a})}\right) \tag{2.16}$$

$$\sigma_z = \frac{\sigma_{Avg}}{(1+\frac{2R}{a})}\left(\frac{1+ln\left(\frac{a^2+2aR-r^2}{2aR}\right)}{ln(1+\frac{2R}{a})}\right) \tag{2.17}$$

At the minimum cross-section, the shear stresses are zero and the radial, hoop and axial stresses are the principal stresses. For this case, the von Misses equivalent stress (σ_{eq}) is given in Equation (2.18). Inserting Equations (2.16) and (2.17) into (2.19) gives.

$$\sigma_{eq} = \frac{1}{\sqrt{2}}\sqrt{[(\sigma_z - \sigma_r)^2 + (\sigma_r - \sigma_\theta)^2 + (\sigma_\theta - \sigma_z)^2]} \tag{2.18}$$

$$\sigma_{eq} = \frac{\sigma_{Avg}}{\left(1+\frac{2R}{a}\right)ln\left(1+\frac{a}{2R}\right)} \tag{2.19}$$

Using Equation 2.19, Equations 2.15 and 2.16 are re-written as

$$\sigma_r = \sigma_\theta = \sigma_{eq} ln\left(\frac{a^2+2aR-r^2}{2aR}\right) \tag{2.20}$$

$$\sigma_z = \sigma_{eq}\left[1 + ln\left(\frac{a^2+2aR-r^2}{2aR}\right)\right]$$

On the external surface, the axial stress component σ_z is equal to the average axial stress σ_{Avg} because the radial stress σ_r and the hoop stress σ_θ become negligible at the center of the necking region during plastic deformation. This relationship is clearly illustrated in Figure 2.9, which shows the average and equivalent stress-strain curves along with the corresponding stress distributions in the necking region. The stress distribution within the necking region has two phases. In phase I, the average axial stress σ_{Avg} represents the uniform load across the cross-section, and the equivalent stress σ_{eq} equals σ_{Avg} . As deformation progresses to phase II, localized necking leads to a non-uniform stress distribution.

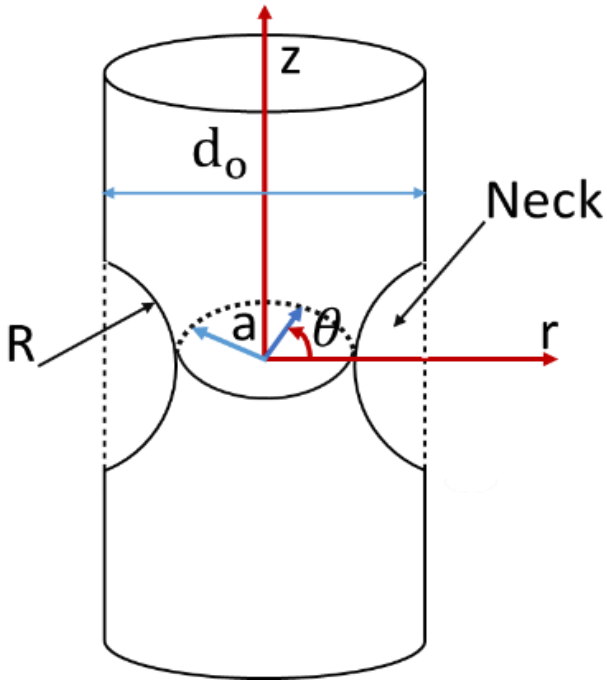

Figure 2.8. Tensile necking region in a round bar (Source: Bao et al., 2005)

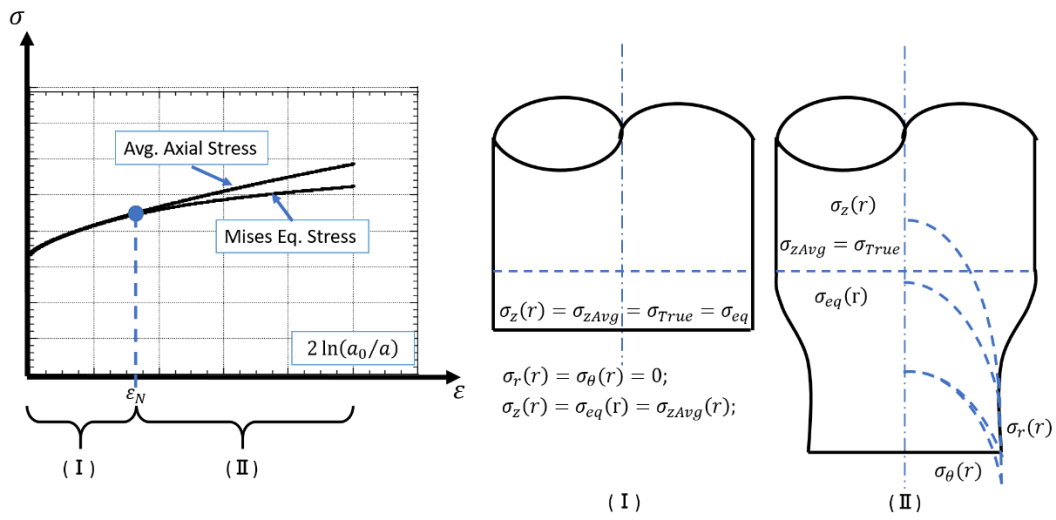

Figure 2.9. The average and equivalent stress-strain curves and the corresponding stress distributions (Source: Mirone G. et al., 2010 [6])

In Equation (2.19), the term on the right side denominator is regarded as the Bridgman's correction factor, B, which is implemented to offset the impacts of stress triaxiality present in the necking area as

$$B = \frac{1}{\left(1+\frac{2R}{a}\right)ln\left(1+\frac{a}{2R}\right)} \tag{2.21}$$

Equation (2.19) can be rewritten in simple terms as

$$\sigma_{eq} = B\sigma_{Avg} \tag{2.22}$$

Equation (2.22) points that the true stress within the necking area is equivalent to the von Mises equivalent stress, in accordance with the von Mises plasticity criterion[7]. Consequently, the principal longitudinal true stress in the necking zone is deducible through the application of Equations (2.17) and (2.18)

$$\sigma_z = \sigma_e + \sigma_r = \sigma_e + \sigma_\theta \tag{2.23}$$

The stress triaxiality (σ^*) at the centre of a neck region in a tensile test specimen is hence

$$\sigma^* = \frac{\sigma_h}{\sigma_{eq}} = \frac{1}{3} + \ln\left(1 + \frac{a}{2R}\right) \tag{2.24}$$

where σ_h is the hydrostatic stress. The equivalent strain (ε_e) on the necking region is

$$d\varepsilon_{eq} = \frac{\sqrt{2}}{3}\sqrt{[(d\varepsilon_z - d\varepsilon_r)^2 + (d\varepsilon_r - d\varepsilon_\theta)^2 + (d\varepsilon_\theta - \sigma d\varepsilon_z)^2]} \quad (2.25)$$

Considering plastic deformation, the relation between radial and axial strain is

$$d\varepsilon_r = d\varepsilon_r = -0.5 d\varepsilon_z \quad (2.26)$$

Inserting Equation (2.26) into Equation (2.25) gives the equivalent strain (ε_{eq}) as

$$\varepsilon_{eq} = \varepsilon_z = ln\left(\frac{A_0}{A_i}\right) = 2ln\left(\frac{d_o}{d_i}\right) \quad (2.27)$$

where, d_o and d_i are the initial and instantaneous radius (or necking radius) of the test specimen, respectively.

Murata et al.[8] conducted virtual tensile tests on smooth round bar specimens, employing pre-determined flow stress-strain curves based on Swift and Voce models. The average stress derived from these simulated tests was adjusted using the Bridgman correction method. Their findings indicated that the flow stress, as corrected by Bridgman's method, tended to overestimate the reference flow stress. Furthermore, they executed actual tensile tests on low carbon steel SS400 (as per JIS standards). For these tests, the average stress was corrected using both an inverse method and the Bridgman method. The outcomes revealed that the flow stress values obtained through the Bridgman correction were higher than those derived from the inverse method they proposed. Similarly, La Rosa et al.[9] carried out real tensile tests on D98 steel, determining the flow stress through the Bridgman method. The resulting flow stress-strain curve served as a benchmark and was input into numerical tensile tests. From these simulations, the average true stress was calculated and adjusted using the Bridgman method for a comparison with the original input flow stress. As depicted in Figure 2.10, a notable discrepancy emerged between the input flow stress and the flow stress corrected by the Bridgman method, particularly at larger strains. This error was observed to increase to approximately 10% when the strain approached a value of 1.35. Generally, it is acknowledged that the accuracy of the Bridgman correction diminishes at high strain levels. The primary sources

of these errors are linked to the assumption that both equivalent stress and strain remain consistent across the minimum cross-sectional area of the specimen. Numerical studies have revealed that the distribution of stress, strain, and stress triaxiality across this minimal cross-sectional area significantly deviates from the predictions of the Bridgman analytical model [6, 10, 11].

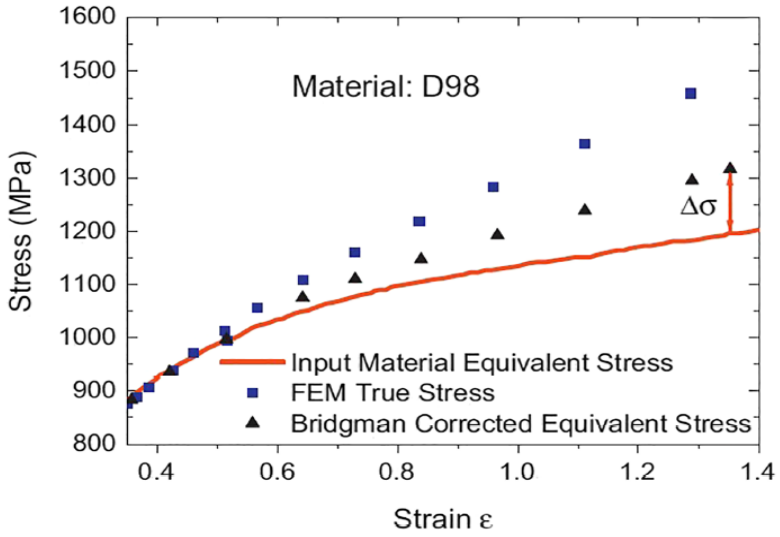

Figure 2.10. A Comparative analysis of the input equivalent stress for the material and the stress corrected using the Bridgman method (Source: La Rosa, G. et al., 2003 [9])

2.3. The MLR Correction Method

The Bridgman method assesses the flow stress for a cylindrical tensile test specimen post-necking and provides an adjustment formula to recalibrate the experimentally derived average true stress to the von Mises equivalent stress for the post-necking elastoplastic properties. The post-necking is of significant importance for many ductile materials that show large strains at failure. The implementation of Bridgeman's correction methodology necessitates recording the neck contour since the equation incorporates the real-time minimum radius and the curvature of necking for the cylindrical test samples. The MLR function, introduced by Mirone[10, 12, 13], offers an advantage over the Bridgman method as it eliminates the need for the intensive experimental procedures inherent in the latter. Furthermore, when compared to

Bridgman's approach, which exhibits error margins between 5% and 13%, the MLR methodology demonstrates more precise results, with errors ranging between 3% and 5%.

The MLR correction facilitates the transformation of the average true stress into the equivalent stress in the conditions of quasi-static loading [10] as

$$\sigma_{eq} = \sigma_{Avg} MLR\,(\varepsilon_{eq} - \varepsilon_N) \tag{2.28}$$

where ε_N is the necking strain [12], and

$$MLR(\varepsilon_{eq} - \varepsilon_N) = 0.9969 - 0.6058\,(\varepsilon_{eq} - \varepsilon_N)^2 + 0.6317\,(\varepsilon_{eq} - \varepsilon_N)^3 - 0.2107\,(\varepsilon_{eq} - \varepsilon_N)^4 \tag{2.29}$$

The MLR method is designed to produce a graphic depiction of the stress distribution across the material cross-section in post-necking conditions. This is achieved by charting the trend of the ratio of the averaged equivalent stress over the entire cross-section to the averaged true stress (σ_{eq}/σ_{Avg}) against the backdrop of the difference in strain values ($\varepsilon_{eq} - \varepsilon_N$). This graphical illustration endeavors to provide a more detailed understanding of the stress-strain relationship in materials especially when they are subjected to extreme deformation that results in necking. The effectiveness of the MLR correction method has been confirmed across smooth cylindrical samples of varying dimensions, composed of over 15 different isotropic metals. This range includes a variety of steels, pure copper, aluminum, and others, all subjected to monotonic loading conditions where isotropic hardening is a valid assumption[6]. In the graphical illustration denoted as Figure 2.11[12], one can observe the correlation between the ratio of stresses and the disparity in strain values across a range of materials. The pair of MLR functions are contingent upon the present value of logarithmic plastic strain, denoted as ($\varepsilon_{eq} \approx 2\ln(a_0/a)$), and also on the strain value at the onset of necking, (ε_N), which is a constant specific to the material [10].

Mirone et al. [14] have demonstrated that the MLR correction for post-necking, is equally applicable to dynamic strain scenarios. This adaptability permits the conversion of true stress-strain curves obtained from Split Hopkinson Tension Bar (SHTB) experiments into precise estimations of von Mises stress curves under conditions of high strain rates.

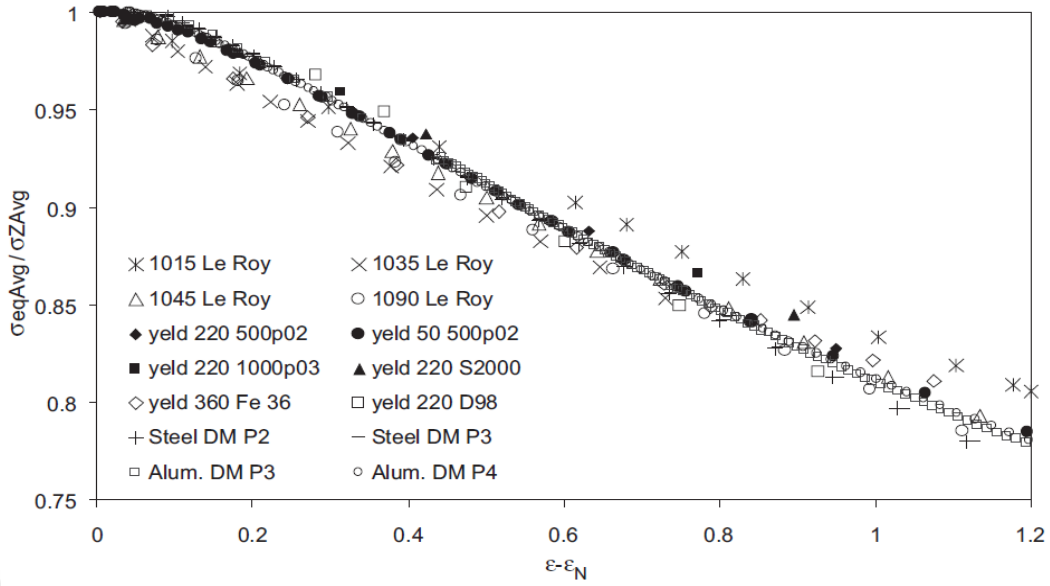

Figure 2.11. Progression of the average equivalent stress to average true stress ratio as a function of the normalized plastic strain (Source: Mirone, G. et al., 2004 [12])

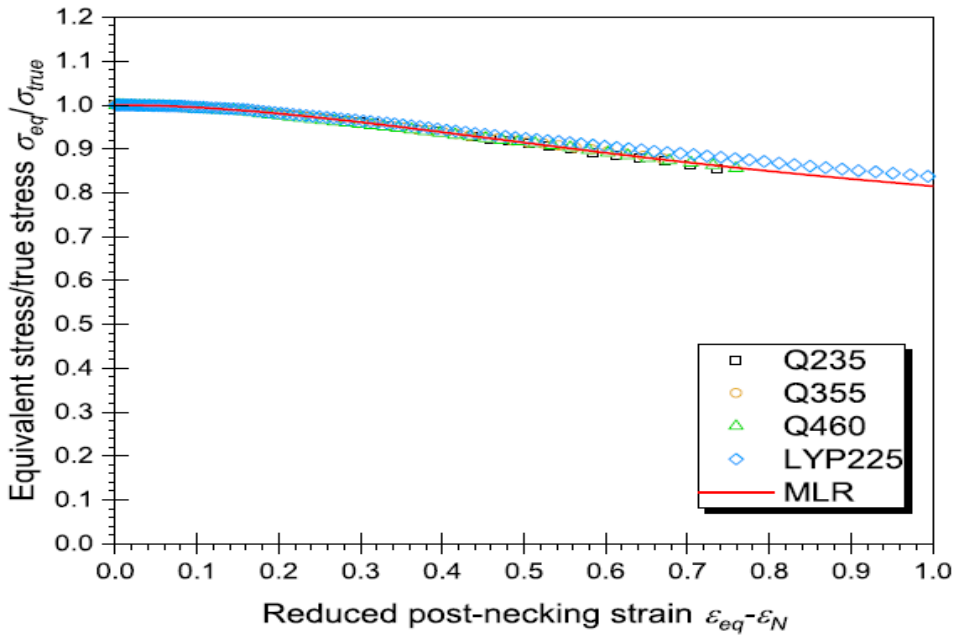

Figure 2.12. Contrast of the data relating to the ratio of equivalent stress to true stress against the adjusted strain values post-necking and the application of MLR correction (Source: Versaillot, P. D. et al., 2021 [15])

Additional corroboration was however shown to be essential prior to the application of the MLR correction for structural steels [16]. Z. Yao et al.[15] noted that the

MLR correction method accurately forecasts the actual material behavior of structural steels subsequent to necking. The disparity between the observed responses of the Q235, Q355, and Q460 steel grades and the predictions made by the MLR model was found to be minimal. Hence, it is generally considered that the MLR function is suitable for adjusting the true stress in structural steel analyses. Figure 2.12 presents a graphical representation that demonstrates the correlation between the MLR adjusted values for these materials and the ratio of equivalent stress to true stress (σ_{eq}/σ_{Avg}) against the modified strain resulting from necking ($\varepsilon_{eq} - \varepsilon_N$)[15]. The MLR method was tested on three different steel specimens, each with a length of 25 mm and a cross-section of 5 mm. The steels used were Steel 1015, Steel 1045, and Steel 1090. To derive the true stress-strain curves, Finite Element Analysis (FEA) was employed using the MARC FE code, which accounted for the material's typical non-linear behavior and the extensive displacement fields[12]. Figure 2.13 illustrates the comparison of the true stress-strain curves obtained using the MLR correction against the traditional engineering curves[12]. Utilizing the relationship of $\sigma_{eq} - \varepsilon_e$, derived from the MLR equation, researchers can estimate the distribution of triaxiality on the neck section. This estimation is critical for assessing the impact of necking on the damage behavior of ductile metals, especially in understanding void growth behavior under stress conditions.

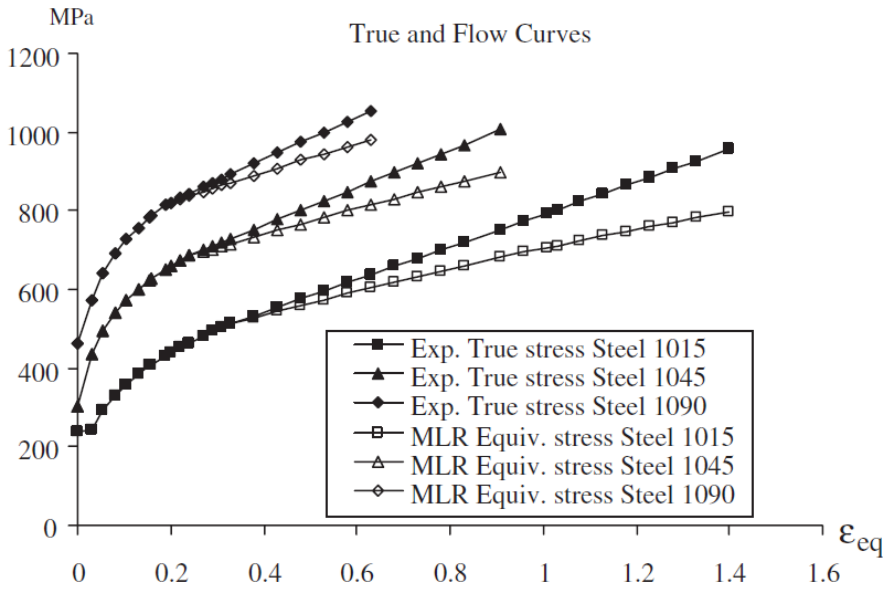

Figure 2.13. True curves of Steel 1015, Steel 1045, and Steel 1090
(Source: Mirone, G. et al., 2004 [12])

2.4. The Constitutive Equations

The deformation behavior of metals and alloys is complex as it is highly sensitive to loading type, strain, strain rate and temperature. Constitutive equations are the mathematical expressions that correlate stress with strain, strain rate, and temperature. The general form of these equations can be written as

$$\sigma = f(\varepsilon, \dot{\varepsilon}, T) \tag{2.30}$$

These constitutive equations are expected to be comprehensive to include both quasi-static and dynamic loading, robust, computationally efficient, and reliant on a minimal set of readily available constants. Metals exhibit variations in mechanical properties such as strength and ductility depending on loading rates and temperatures. Therefore, integrating strain rate dependency is vital in designing structural components subjected to high-velocity impacts, explosions, and other dynamic conditions. Various constitutive models that require a relatively limited number of material constants are available for use in numerical simulations. Meyers[17] and Langrand et al.[18] have reviewed constitutive equations designed for high-strain rate scenarios. The JC[19], Modified Johnson-Cook (MJC) and Zerilli and Armstrong[20] are shown among the mostly widely used ones in dynamic loading.

2.5. The Johnson – Cook Strength Model

The Johnson and Cook[19] formulated the JC model in 1983 and published the model parameters of 12 distinct metals. The model is well-suited for metals deforming under large strains, high strain rates, and elevated temperatures. Subsequent studies include the work of Noble et al. [21] on iron, Kay et al. [22] on a titanium and an aluminum alloy, Nemat-Nasser and et al. [23] on a structural steel, Klepaczko et al. [24] on two different structural steels and Scapin et al. [25] on an alumina dispersion-strengthened copper.

A dimensionless equivalent plastic strain rate $\dot{\varepsilon}_{ep}^{*}$ is defined in Equation (2.31).

$$\dot{\varepsilon}_{ep}^{*} = \frac{\dot{\varepsilon}_{ep}}{\dot{\varepsilon}_0} \tag{2.31}$$

In above, $\dot{\varepsilon}_{ep}$ is the equivalent plastic strain rate and $\dot{\varepsilon}_0$ is the reference strain rate. A homologous or homogeneous temperature, symbolized by T^*, is given as

$$T^* = \frac{T - T_r}{T_m - T_r} \tag{2.32}$$

T denotes the temperature at which material testing is conducted, T_r is established as a room temperature, and T_m corresponds to the melting temperature of the material. By taking ε_{ep} as the equivalent plastic strain the JC is expressed as

$$\sigma_e = \left(A + B\varepsilon_{ep}^n\right)\left[1 + cIn\left(\dot{\varepsilon}_{ep}^*\right)\right][1 - (T^*)^m] \tag{2.33}$$

Parameters A, B, and n are associated with the yield strength and the strain-hardening behavior of the material, c is indicative of the rate-hardening effect, and m characterizes the thermal softening of the material. The initial term in Equation (2.33) indicates the work hardening behavior of the material when subjected to the nominal strain rate, whereas the subsequent terms correspond to the material's sensitivity to strain rate and temperature, respectively. The model, in its current form, presumes that the influences of strain rate and temperature are mutually exclusive; however, in practice, materials often exhibit a strain rate sensitivity that is inherently temperature-dependent.

The modified JC equation is further provided for the complex parabolic stress-strain relations as given below

$$\sigma_e = \left(\left(A + B\varepsilon_{ep}^n\right) + Q_1(1 - \exp(C_1\varepsilon)) + Q_2(1 - \exp(C_2\varepsilon))\right)\left[1 + \dot{\varepsilon}_{ep}^*\right]^c[1 - (T^*)^m] \tag{2.34}$$

where Q_1, Q_2, C_1 and C_2 are the parameters that are determined from the experimental stress-strain curves.

The parameters *A, B, n, C,* and *m* of the JC strength equation are usually determined by performing various tests and fitting the equations to the experimental data as one example is shown in Figures 2.14(a-d). The determinations of the JC parameters in Figures 2.14(a-d) are as follows.

1) At room and reference strain rate, the second and third terms of Equation (2.33) are 1. Then, the yield strength in the reference curve gives the value of A (Figure 2.14(a)).
2) From the reference curve, the slope and intercept of a plot of $\ln(\sigma_e - A)$ vs. $ln\varepsilon_{ep}$ gives sequentially the value of n and B based the following relation: $\ln(\sigma_e - A) = lnB + n\, ln\varepsilon_{ep}$ (Figure 2.14(b))
3) Similarly, at the reference strain rate, the slope of $ln\left(1 - \frac{\sigma_e}{A+B\varepsilon_{ep}^n}\right)$ vs. $ln(T^*)$ gives the value of m (Figure 2.14(c)).
4) Finally, at the reference strain rate, the slope of $\left(\frac{\sigma_e}{A+B\varepsilon_{ep}^n} - 1\right)$ vs. $In\left(\dot{\varepsilon}_{ep}^*\right)$ gives the value of C (Figure 2.14(d)).

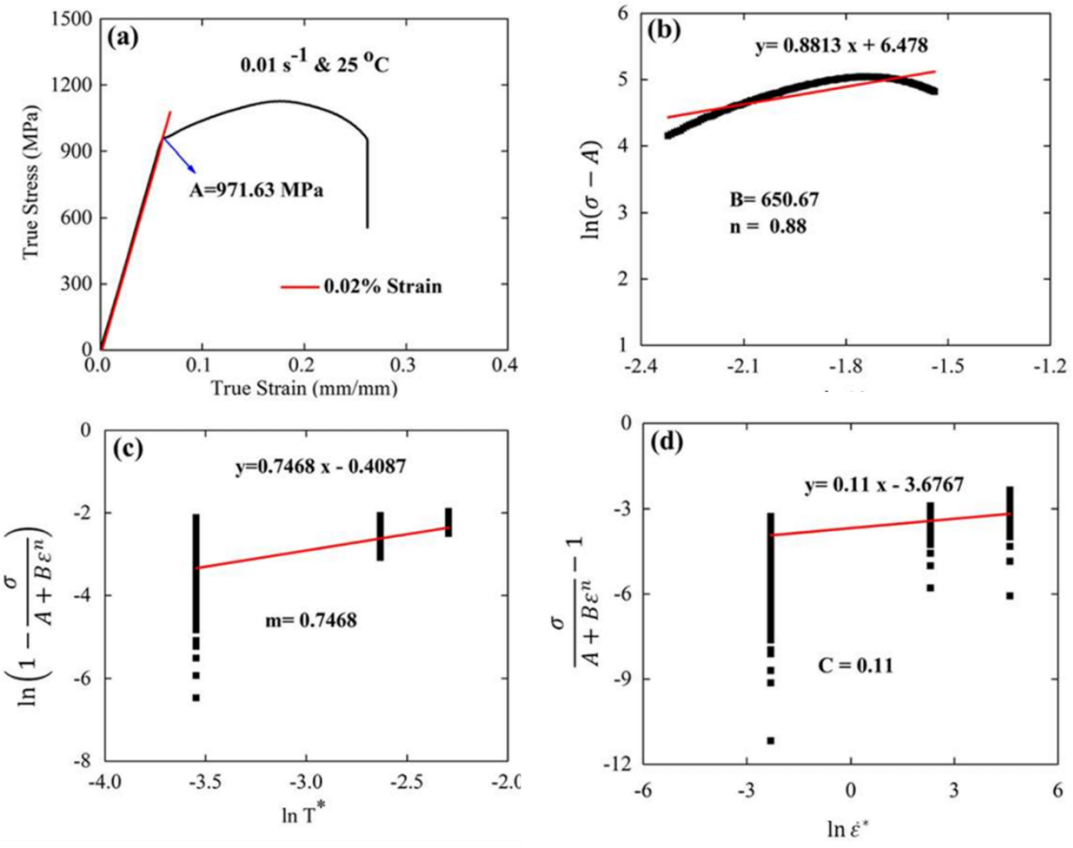

Figure 2.14. Estimation of JC model parameters: (a) *A* as the 0.02% yield stress, (b) the strain hardening modulus, *B*, and the strain hardening coefficient, *n*, (c) the thermal softening coefficient, *m*, and (d) the strain rate sensitivity coefficient, *c*, for quasi-static tensile loading (Source: Deb et al., 2022 [26]).

Examples of the studies on the JC flow stress parameter determination can be widened while few of them will be summarized in this part. Jaspers and Dautzenberg et al.[27] conducted SHPB compression tests on AISI 1045 steel and AA 6082-T6, and identified the JC constitutive model parameters for these materials. Lee and Lin [28] conducted an investigation into the high-temperature deformation behavior of Ti64 alloy utilizing SHPB tests. The tests were conducted at a constant strain rate of 2000 s^{-1}, with an initial temperature ranging from 700 to 1100°C. They obtained the parameters for the JC model by fitting the experimental data. Additionally, they reported another set of parameters obtained at the strain rates between 500 and 3000 s^{-1} and temperatures ranging from room temperature to 1100°C [29]. Manes and L. Peroni et al. [30] introduced a combined experimental and numerical technique, employing an inverse approach, for identifying material model parameters. They applied this method to characterize the Al 6061-T6 alloy by conducting tests using the SHPB. Banerjee and S. Dhar et al. [31] determined the material constants for the JC model applicable to armor steel by conducting uniaxial tensile tests across a range of strain rates using Finite Element simulations within the ABAQUS platform. Michal Grazka et al. [32] determined the JC parameters for copper and aluminum through a combination of Modified Hopkinson Bar testing, Taylor impact experiments, and Finite Element Analysis.

Given that empirical constitutive equations are fundamentally a process of curve fitting; they offer a straightforward calibration approach requiring only a minimal set of experimental data. This typically involves the acquisition of a limited number of stress-strain curves at various strain rates and temperatures for model calibration. Kay et al.[22] defined a new set of material constants for the JC model, considering both high strain rates (2500 s^{-1}) and low strain rates (10^{-4} s^{-1}) based on the data from Lee and Lin [28, 29]. Meyer and Kleponis et al. [33] determined the JC parameters for Ti-64 at constant strain rates of 10^{-4}, 10^{-1}, and 2150 s^{-1} at room temperature. Seo et al.[34] predicted the flow behavior of Ti-64 alloy at the strain rates of 1400 s^{-1} and temperatures up to 1000°C. Kotkunde et al. [35] conducted tests on the same material at low strain rates (10^{-5}, 10^{-4}, 10^{-3}, and 10^{-2} s^{-1}) and elevated temperatures (323–673 K) using constitutive modeling based on isothermal uniaxial tensile tests. Wang et al. [36] the automated ball indentation (ABI) technique was employed to investigate the flow behavior of Ti-64 alloy across a wide range of temperatures (293 K, 493 K, 693 K, and 873 K) and low strain rates (10^{-6}, 10^{-5}, and 10^{-4} s^{-1}). The experimental true stress–plastic strain data obtained from the ABI tests

were utilized to characterize the material behavior of Ti-64 alloy. Specifically, the JC material model was applied to predict the flow behavior of the alloy under conditions of low strain rates and elevated temperatures. To validate the accuracy of the JC material model, finite element analysis was conducted to confirm the fitting parameters. Figure 2.15(a-c) show sequentially the experimental and the JC model FEA stress-strain curves at 3 different strain rates at different temperatures in the same study. Additionally, a comparative study was conducted to assess the performance of various JC models in predicting the behavior of Ti-64 alloy under the specified conditions.

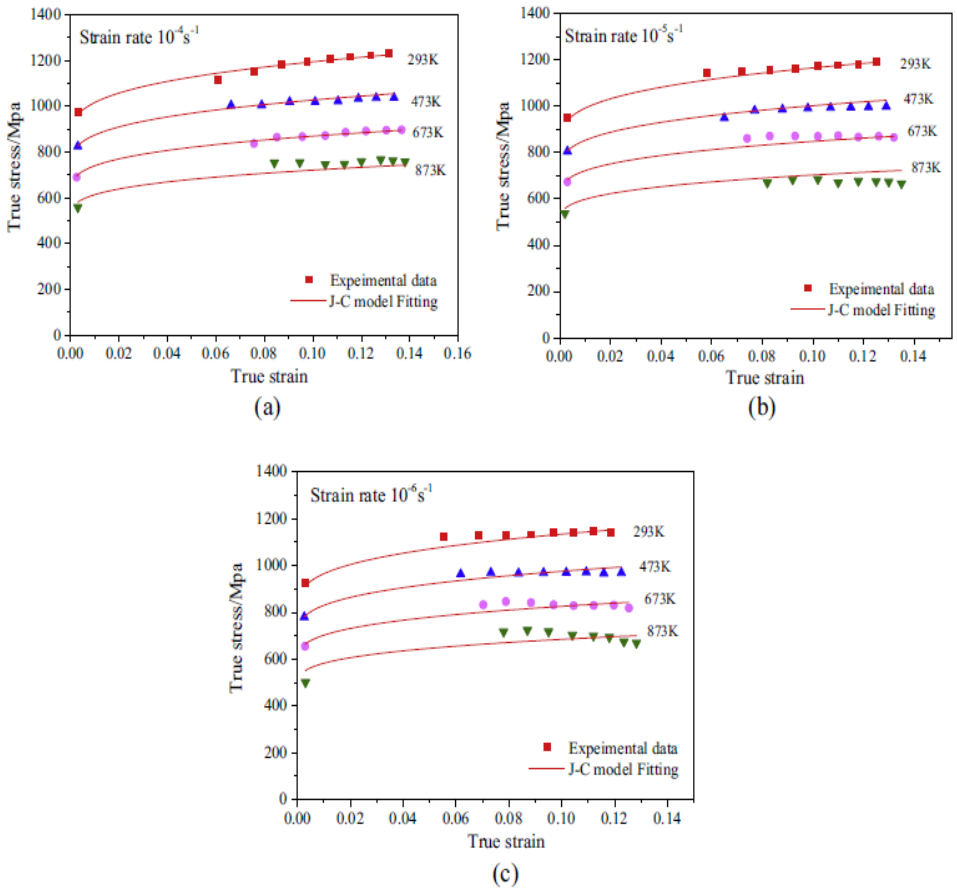

Figure 2.15. Comparison of flow stress curves under different strain rates: (a) at a strain rate of 10^{-4} s^{-1}, (b) at a strain rate of 10^{-5} s^{-1}, and (c) at a strain rate of $10^{-6}s^{-1}$, between experimental data and JC fitting (Source: Wang et al., 2015 [36]).

2.6. The Johnson – Cook Damage Model

The JC damage/fracture model[37] was developed in 1985 and represents an empirical cumulative fracture model that establishes correlations among the impact of strain rate, stress triaxiality, and temperature on fracture strain. The progression of damage that develops with the applied stress in a mechanical test can be observed in Figure 2.16. In sections a–b, the material undergoes elastic deformation. Upon surpassing the yield stress (σ_y) at point b–c, the material transitions into a phase of stable plastic deformation, where the influence of strain hardening predominates. The material initiates failure at point c, marked by the onset of plastic instability. Subsequently, as the equivalent stress decreases, the material enters the phase of failure evolution (sections c–d), characterized by more pronounced thermal softening behavior. Upon reaching point d on the stress–strain curve, the material experiences complete failure [38, 39].

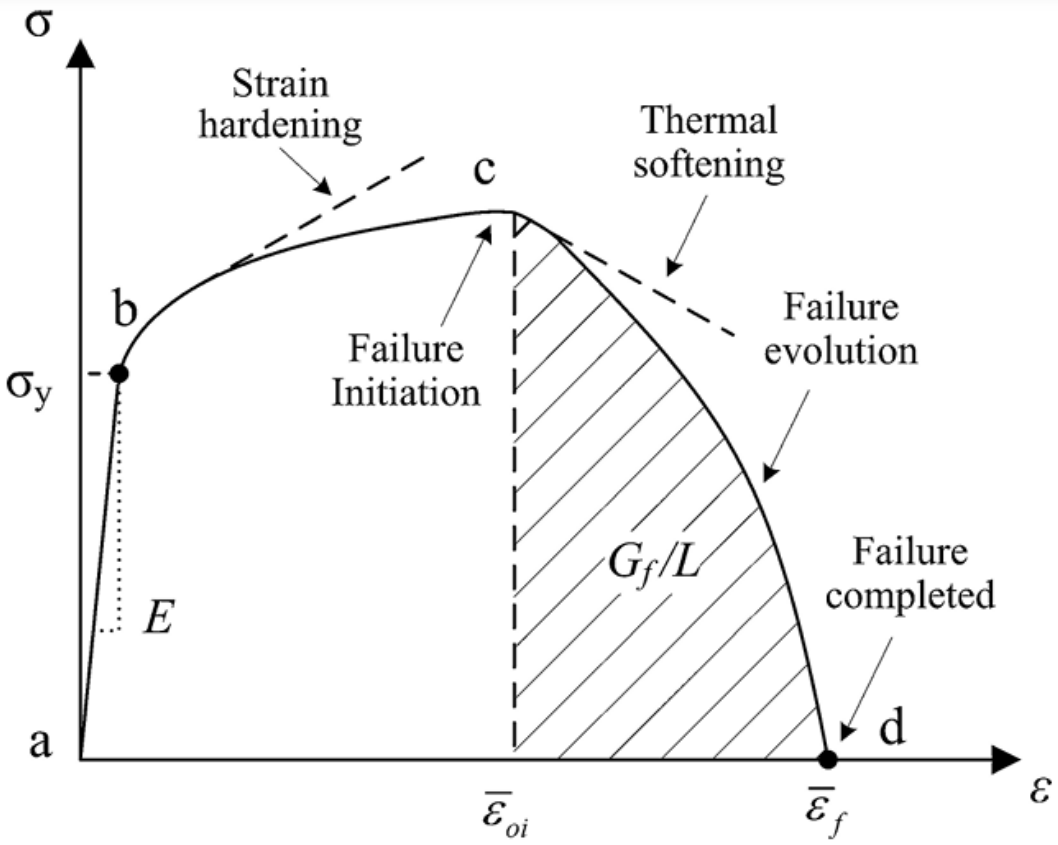

Figure 2.16. Stress-strain graph of material failure process (Source: Chen et al., 2011[38]).

This model[37] is founded upon a linear assumption of damage accumulation criteria, as demonstrated in Equation (2.35).

$$D = \sum \frac{\Delta \varepsilon_{ep}}{\varepsilon_{ef}} \tag{2.35}$$

where, $\Delta \varepsilon_{ep}$ represents the incremental alteration in the equivalent plastic strain during the deformation process, while ε_{ef} denotes the corresponding strain at the point of material failure. It is noteworthy that the damage parameter, denoted as '*D*,' spans a range between 0 and 1, with material failure occurring when *D* reaches or exceeds 1. In Figure 2.16, $D = 0$ at the point c and $D = 1$ at the point d. The formulation of the JC failure model is presented as follows:

$$\varepsilon_{ef} = [D_1 + D_2 exp(D_3 \sigma^*)]\left[1 + D_4 In\left(\dot{\varepsilon}^*_{ep}\right)\right][1 + D_5(T^*)] \tag{2.36}$$

where, D_1, D_2 and D_3 are the triaxial stress state parameters, D_4 is the strain rate parameter, D_5 is the temperature parameter, and σ^* is the stress triaxiality given in Equation (2.24). The value of D_3 was reported *1.5* for spherical void development [40].

Low strain rate tests were conducted using both smooth and notched tensile specimens. Subsequently, a curve fitting procedure was employed to establish relationships between failure strain and stress triaxiality, resulting in the determination of values for parameters D_1, D_2 and D_3. Parameter D_4, representing the strain rate dependency, was derived from the slope of this curve. Additionally, the temperature-dependent fracture strain parameter, D_5, was computed by fitting the failure strain data collected at various temperatures.

Majzoobi and Dehgolan et al.[41] conducted a calibration of the material parameters for the JC fracture model using a combined method involving experimental, numerical, and optimization techniques. Parameters D_1, D_2 and D_3 were determined through a quasi-static tensile test with a notched bar, while D_4 was obtained from a dynamic test with a notched bar utilizing a high-rate testing device known as the flying wedge. Dzugan et al. [42] performed a calibration of fracture parameters based on the fracture locus for typical steel used in the nuclear power plant industry. Their calibration process involved three types of tests, including tensile tests with notched round bars, punch tests, and a

specially designed test using a specimen with double curvature. All these tests were conducted under quasi-static conditions at room temperature. Consequently, only parameters D_1, D_2 and D_3 were calibrated in this study. Banerjee et al.[31] conducted an investigation into the behavior of armor steel material, seeking to analyze and predict its response under various dynamic loading conditions. Their developed JC constitutive and damage model exhibited a reasonable concordance between simulations of Charpy impact tests and experimental outcomes. Xueping Zhang et al.[43] delved into the hard turning process, aiming to predict the impacts of cutting parameters and tool geometry. Their work leveraged the JC damage model, yielding results that exhibited enhanced agreement with experimental observations. Buzyurkin et al.[44] focused on the fracture behavior of titanium alloys, utilizing experimental data from diverse dynamic loading scenarios.

The reported JC flow stress and damage model parameters of Ti64, 316L and AISI 4340 alloys are tabulated in Table 1 and Table 2, respectively. As noted in the same tables, Ti64 alloy is the most widely investigated alloy for the determination of the JC parameters and AISI 4340 alloy is the least studied one. In any case, the variations of the parameters between different studies are clearly seen in the same tables.

Table 1. The JC flow stress parameters of Ti64, 316L and AISI 4340 alloys

Study	***A (MPa)***	***B (MPa)***	***n***	***C***	***m***	$\dot{\varepsilon}_o$	**Mat**
Johnson et al.[19]	862	331.2	0.34	0.0120	0.8	1	Ti64
Meyer et al.[33]	896	656	0.50	0.0128	0.8	1	Ti64
Lee et al.[29]	724.7	683.1	0.47	0.035	1.0	0.00001	Ti64
Lee et al.[28]	782.7	498.4	0.28	0.028	1.0	0.00001	Ti64
Leseur et al.[45]	1098	1092	0.93	0.014	1.1	1	Ti64
Seo et al.[34]	997.9	653.1	0.45	0.0198	0.7	1	Ti64
Khan et al.[46]	1080	1036	0.6349	0.0139	0.7794	1	Ti64
	1104	1007	0.5975	0.01304	0.7701	1	
Calamaz et al.[47]	968	380	0.421	0.0197	0.577	0.1	Ti64
Ozel et al.[48]	803.5	544.57	0.3616	0.05	1.041	1	Ti64
	883.99	598.87	0.3616	0.0335	1.041	1	Ti64
	987.8	761.5	0.4143	0.01516	1.516	1	
Dorogoy et al.[49]	880	695	0.36	0.04	0.8	1	Ti64
Dumitrescu [50]	870	990	1.01	0.008	1.4	1	Ti64
Dabboussi et al.[51]	1050	955	0.63	0.011	1	1	Ti64
Wang et al.[36]	838.5	712.4	0.3	0.011	0.89	1	Ti64
Raut et al.[52]	969.36	528.636	0.5747	0.0937	0.4938	0.0001	Ti64
	969.36	464.053	0.5325	0.0939	0.4937	0.0001	Ti64
	969.36	544.57	0.693	0.12	0.4958	0.0001	

(cont. on next page)

Table 1. (cont.)

Chen et al.[38]	860	683	0.47	0.035	1	1	Ti64
Pittala et al.[53]	0	1508	0.049	0.067	0.71	1	Ti64
Guo et al.[54]	955	770	0.557	0.012	-	0.0001	Ti64
Deb et al.[26]	971.63	650.688	0.88	0.073	0.75	0.01	Ti64
Tao et al.[55]	814	700	0.69	0.0218	0.893	0.01	Ti64
Hammer et al.[56]	1062	431	0.5	0.016	0.69	1	Ti64
Huang et al.[57]	891.5	630.3	0.547	0.034	0.9432	1	Ti64
Wang et al.[58]	1019.5	674.1	0.92	0.03	0.457	0.001	Ti64
Perosanz et al.[59]	732	780	0.53	0.022	0.78	0.001	Ti64
	800	700	0.6	0.02	0.75	0.001	Ti64
	880	780	0.65	0.015	0.79	0.001	
Verleysen et al.[60]	951	892	0.7	0.015	0.71	1	Ti64
Harzallah et al.[61]	880	582	0.353	0.041	0.6337	1	Ti64
Lin et al.[62]	1035	331	0.635	0.04	1.7	1	Ti64
Chen et al.[63]	831.35	857.932	0.302	0.015	0.724	0.01	Ti64
Kotkunde et al.[35]	869.4	649.5	0.3867	0.0093	0.7579	0.001	Ti64
Wu, H. et al.[64]	1000	780	0.47	0.033	1.02	1	Ti64
Wu, S. et al.[65]	895.2	910.1	0.749	0.033	1.045	0.00042	Ti64
Yang et al.[66]	910	870	0.68	0.02	0.71	0.001	Ti64
Hu H., et al.[67]	797.46	305.7	0.2857	0.0196	-	1	Ti64
	771.78	269.3	0.2242	0.012	-	1	Ti64
	941.33	470.55	0.4655	0.0242	-	1	
Yatnalkar et al.[68]	920	380	0.578	0.042	0.633	0.001	Ti64
Perez et al.[69]	1055	426	0.5033	0.023	0.8	1	Ti64
Peng et al.[70]	356.09	1264.35	0.77	0.008	1.28	0.0005	316L
Karkalos et al.[71]	310.8	881.38	0.178	0.19	1.25	1	316L
Chandrasekaran et al.[72]	305	1161	0.61	0.01	0.517	1	316L
	305	441	0.1	0.057	1.041	1	316L
Umbrello et al.[73]	301	1472	0.807	0.09	0.623	0.001	316L
Tounsi et al.[74]	514	514	0.508	0.042	0.533	0.001	316L
Tamer et al.[75]	286.947	1187.96	0.6457	0.00657	1	0.001	316L
Li et al.[76]	583	5086	1.37	0.01805	0.77	0.001	316L
Svoboda et al.[77]	111	358	0.49	0.257	0.805	1	316L
Dharavath et al.[78]	107	364	0.35	0.16	0.75	0.001	316L
Klocke et al.[79]	331	1125	0.91	0.1	0.74	1	316L
Yang et al.[80]	380	825	0.726	0.115	1	1	316L
Liu et al.[81]	200	1298	0.75	0.02	1	1	316L
Alkhatib et al. [82]	595	1635	0.98	0.0113	1	0.001	316L
Flores-Johnson et al.[83]	238	1202.4	0.675	0.0224	1.083	0.001	316L
Benmeddour et al.[84]	412	761	0.51	0.038	0.52	1	316L
Wang et al.[85]	284	913	0.609	0.1	1	1	316L
Meng et al.[86]	2100	1750	0.65	0.0028	0.75	1	4340

(cont. on next page)

Table 1. (cont.)

Shyan Lee et al.[87]	950	725	0.375	0.015	0.625	1	4340
Sulaiman et al.[88]	792	510	0.26	0.014	1.02	1	4340
Gopikrishnan P., et al.[89]	1366	867	0.93	0.02581	1.03	1	4340
Keith et al.[90]	396	820	0.397	0.014	1.001	1	4340
Ning et al.[91]	850	356	0.304	0.072	0.513	1	4340
Joo et al.[92]	1160	416	0.284	0.0124	1	1	4340
Sattouf et al.[93]	829	483	0.0138	0.2523	1.0764	0.001	4340
	644	500	0.142	0.2851	1.0228	0.001	
	810	507	0.0154	0.2412	1.0316	0.001	
Goh et al.[94]	719	456	0.093	0.008	1.03	0.001	4340

Table 2. The JC damage parameters of Ti64, 316L and AISI 4340 alloys

Study	D_1	D_2	D_3	D_4	D_5	$\dot{\varepsilon}_{ref}$	**Mat**
Hammer et al.[56]	-0.8	1.18	-0.15	-0.012	2.1	1	Ti64
Johnson et al.[37]	-0.09	0.25	-0.5	0.014	3.87	1	Ti64
Huang et al.[57]	0.01546	1.349	-2.144	0.04323	0.6815	1	Ti64
Wang et al.[58]	0.021	0.132	-1.1	0.0238	3.451	0.001	Ti64
Kay et al.[22]	-0.09	0.27	0.48	0.014	3.87	1	Ti64
Chen et al. [95]	-0.09	0.25	-0.5	-0.023	3.214	0.01	Ti64
Bobbili et al.[96]	-0.012	0.31	0.24	0.018	2.3	1	Ti64
Perosanz et al.[59]	0.55	0.8	0.6	-0.028	1.2	0.001	Ti64
	0.22	0.65	0.6	-0.022	4.9	0.001	
	0.11	0.2	0.6	0.013	4.9	0.001	
Chen et al. [97]	0.01192	1.5	3.7653	-0.0335	2.1724	-	Ti64
Verleysen et al.[60]	-0.078	0.282	0.479	0.029	3.87	1	Ti64
Sancho et al.[98]	0.07	0.2	0.6	0.03	4.9	0.001	Ti64
Tamer et al.[75]	0.443192	147.017	-20.623	-0.03491	0	0.001	316
Benson et al.[99]	0.05	3.44	-2.12	0.002	0.61	1	4340

2.7. The Zerilli and Armstrong Model

The Zerilli and Armstrong[20] (ZA) constitutive models are widely applied to forecast the response of materials under high deformation rates. It is founded on the principles of dislocation mechanics, particularly when at varying temperatures and strain rates due to impacts or deformation. This theoretical model combines strain strengthening, rate-dependent hardening, and thermal softening factors to forecast the behavior of metals. The volume which is swept by dislocations in plastic deformation is taken in the model as the activation volume. The activation volume in body-centered cubic (BCC) materials in the order of 5 to $100b^3$ (b is the Burger's vector) and it is,

however, 10-100 times larger in face-centered-cubic (FCC) materials than in the BCC[100]. The activation volume is found to be independent of strain in BCC materials [100] while the activation volume in FCC metals decreases as the strain increases [101, 102]. Consequently, this difference leads to different formulations for FCC and BCC materials within the ZA model. The first constitutive formulations were specific to FCC and BCC crystal structures and later it was extended to hexagonal close-packed (HCP) metals, showing intermediate deformation properties to FCC and BCC materials [103].

The BCC model is given as [20 104]

$$\sigma_e = \sigma_a + Bexp(-\beta T) + A{\varepsilon_{ep}}^n \tag{2.37}$$

where

$$\beta = \beta_0 + \beta_1 \ln \dot{\varepsilon}_{ep} \tag{2.38}$$

The material constants used in the models include σ_α, B, β_0, β_1, A, n, a_0, and a_1. In above equation, σ_a is the athermal component of stress (strain rate and temperature independent), the constants A and n relate to the hardening due to strain while a_0 and β_0 reflect the parameters for thermal softening. The focus of our interest lies in a_1 and β_1 which are indicative of the material's sensitivity to the rate of strain. The dislocation movement within BCC metals primarily interacts with the lattice potential, and thermally activated movements are strain-independent. This implies that strain hardening for BCC metals does not vary with strain rate or temperature. In FCC metals, strain hardening is influenced by the rate of strain and temperature due to thermally activated dislocation intersections[20]. The FCC model is given as

$$\sigma_e = \sigma_a + A{\varepsilon_{ep}}^n exp(-\alpha T) \tag{2.39}$$

where

$$\alpha = \alpha_0 + \alpha_1 \ln \dot{\varepsilon}_{ep} \tag{2.40}$$

The stress-strain behavior of HCP metals typically displays characteristics intermediate to those observed in BCC and FCC metals. Consequently, the governing constitutive

relationship for HCP metals is derived by combining the principal mechanisms from both BCC and FCC structures[105]. In thıs context, in the event of the HCP structure, the ZA constitutive model is a superposition of the FCC and BCC constitutive equations as

$$\sigma_e = \sigma_a + Bexp\left[-\left(\beta_0 - \beta_1 \ln\left(\dot{\varepsilon}_{ep}\right)\right)T\right] + A\varepsilon_{ep}^{n} exp\left[-\left(\alpha_0 - \alpha_1 \ln\left(\dot{\varepsilon}_{ep}\right)\right)T\right] \quad (2.41)$$

However, comparative studies in the literature have examined the JC and ZA models. Harding[106] executed the calibration of the JC material parameters through torsion and tension experiments conducted on three distinct metals: OFHC copper, Armco iron, and 4340 steel. These calibrated models facilitated the simulation of these metals in cylinder form being projected against hard surfaces in what are known as Taylor impact tests. The outcomes of these simulations were then assessed in comparison with analogous findings presented by Zerilli and Armstrong[20]. The comparative analysis revealed a harmony between the experimental data and both models, with the ZA model exhibiting a superior predictive accuracy specifically for OFHC copper. Johnson and Holmquist[107] undertook a parallel investigation focusing on the impact behavior of cylinders made from OFHC copper and Armco iron, utilizing the material parameters previously established by JC and ZA for their respective theoretical models. Their investigation confirmed again the findings of Harding[106] and Zerilli and Armstrong, highlighting that both the JC and ZA models closely match experimental observations. However, it was noted that the predictions from the ZA model more accurately reflected the ultimate form of the tested specimens.

2.8. The Cowper – Symonds Constitutive Model

Cowper and Symonds[108] (1957) developed a model for application in analyzing the behavior of a cantilever beam. Specifically, the flow stress for an isothermal condition within the Cowper and Symonds model is formulated as follows

$$\sigma_e = \left(A + B\varepsilon_{ep}^{n}\right)\left[1 + \left(\frac{\dot{\varepsilon}_{ep}}{C_p}\right)^{\frac{1}{p}}\right][1 - (T^*)^m] \quad (2.42)$$

where, C_p and p are material parameters selected to describe material sensitivity to strain rate. The constants C_p and p are determined through calibration with experimental data, often involving a series of dynamic tests where the material is subjected to different rates of loading. The model is particularly adept at describing the high strain rate behavior where conventional static models fail to capture the observed material response. Since its inception, the Cowper-Symonds model has been applied across a variety of materials and has become a staple in the study of dynamic material behavior. Its simplicity, combined with its capacity to capture the essential features of rate-sensitive material response, makes it a valuable asset in the analysis and simulation of materials under dynamic loading[109].

2.9. The Log – quadratic Huh – Kang Constitutive Model

The Log-Quadratic Huh-Kang Constitutive Model[110] presents an advanced framework for capturing the stress-strain response of materials, particularly under conditions of high strain rates. This model was proposed in 2002 to address the limitations of the JC model in describing the behavior of materials undergoing large plastic deformations. The Log-Quadratic Huh-Kang model is mathematically represented by the following equation:

$$\sigma_e = \left(A + B\varepsilon_{ep}^{n}\right)\left[1 + C_1\, ln\left(\dot{\varepsilon}_{ep}^{*}\right) + C_2\left(\ln\left(\dot{\varepsilon}_{ep}^{*}\right)\right)^2\right][1 - (T^*)^m] \qquad (2.43)$$

Here, C_1, C_2 are material constants that are determined through experimental data fitting. The model incorporates logarithmic terms to account for the strain rate's influence on the material's stress-strain behavior, making it particularly suited for materials that exhibit strain rate sensitivity. The log-quadratic nature of the model allows it to describe the nonlinear hardening behavior observed in many materials. The fitting of the model parameters, C_1 and C_2 is a critical process that involves optimizing these constants to match the experimental stress-strain curves obtained from mechanical tests. Such optimization ensures that the model can predict the complex behavior of materials under a variety of loading conditions. The practical applications of the Log-Quadratic Huh-Kang model are diverse, ranging from the analysis of crash simulations in the automotive

industry to the design of metal forming processes. Its ability to accurately model the stress-strain relationship at different strain rates makes it an invaluable tool for engineers and researchers working with dynamic systems where materials experience rapid or varying loads.

2.10. The Allen – Rule Constitutive Model

Allen et al.[111] proposed a strain-rate form that is an exponential of the effective plastic strain rate. The Allen-Rule Constitutive Model is a prominent framework used to predict the stress-strain behavior of materials undergoing plastic deformation. Originating from the work of Allen, Rule & Jones in 1997, this model is integral to the field of materials science and engineering, particularly in the study of metals and alloys. The model is predicated on the principle that material behavior under load can be characterized by a series of exponential forms, each capturing different aspects of the material's response to deformation. The Allen-Rule model is expressed through an exponential form as follows:

$$\sigma_e = \left(A + B\varepsilon_{ep}^{n}\right)\left[\left(\dot{\varepsilon}_{ep}^{*}\right)^{C_3}\right][1 - (T^{*})^{m}] \tag{2.44}$$

where C_3 is an empirical constant that is specific to the material being studied. The power to which the normalized strain rate is raised, namely the constant C_3, is critical in defining how the material's stress response scales with changes in strain rate. This form of constitutive model is particularly adept at capturing the initial elastic response of the material, followed by the nonlinear hardening behavior as the material undergoes plastic deformation.

The determination of the constant C_3 is achieved through experimental testing. Tensile tests, compressive tests, and other forms of mechanical testing can be employed to obtain the stress-strain data needed. Subsequent data analysis and curve-fitting techniques are used to calibrate the model, ensuring that the constant C_3 accurately reflects the material's behavior. This calibration process is crucial for the model's predictive capabilities, especially when applied to simulate real-world scenarios such as metal forming, impact testing, and fatigue analysis.

The versatility of the Allen-Rule model lies in its simplicity and the minimal number of parameters required for its definition. However, this simplicity does not detract from its effectiveness. It has been widely used to describe the behavior of a vast array of materials, from soft polymers to hard ceramics, and its applications extend from basic research to industrial processes. Its ability to describe material behavior over a wide range of strain rates makes it an invaluable tool in the design and analysis of materials subject to dynamic loading conditions.

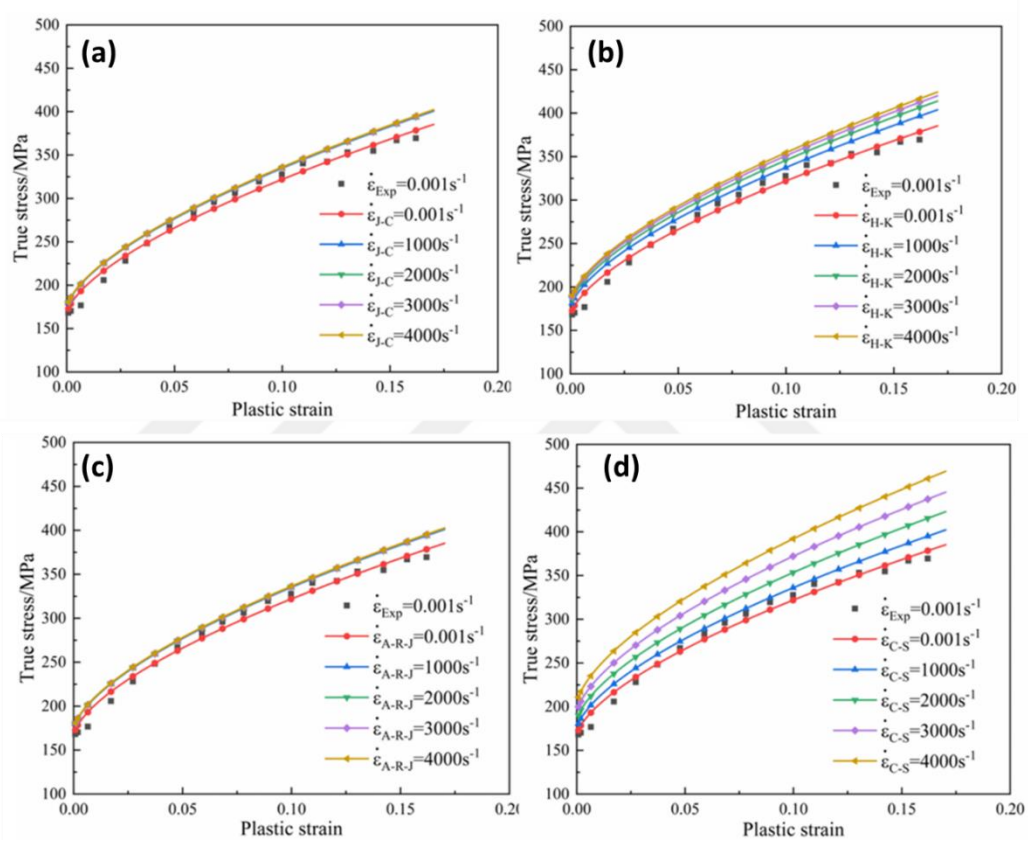

Figure 2.17. Flow stress curves: (a) JC model, (b) HK model, (c) ARJ model and (d) CS model (Source: Liu et al., 2022[112]).

The flow stress curves for AA5182-O aluminum alloy sheets were predicted using the JC, HK, ARJ, and CS models at different strain rates (0.001, 1000, 2000, 3000, and 4000 s^{-1}), as illustrated in Figure 2.17. Using 0.001 s^{-1} as the reference strain rate, the strain rate hardening term for each model was set to 1. At strain rates of 1000, 2000, 3000, and 4000 s^{-1}, the strain rate hardening term for the JC model increased by 4.0, 4.2, 4.3, and 4.4%, respectively. Similarly, the ARJ model exhibited increases of 4.1, 4.3, 4.4, and 4.5%, while the HK model demonstrated increases of 4.6, 7.4, 9.0, and 10.1%. Notably,

the CS model displayed gradual increases in the strain rate hardening term, namely 4.4, 9.8, 15.6, and 21.8%, at these elevated strain rates. The flow stress curves generated by the JC and ARJ models showed relatively low strain rate sensitivity within the range of 1000 to 4000 s^{-1}. Conversely, the HK and CS models exhibited significant strain rate hardening effects at higher strain rates, with the CS model displaying the most pronounced strain rate hardening effect[112].

2.11. Motivation for the Thesis Study

The accuracy of numerical models predicting the response of structures against external loadings has a strong dependence on the accuracy of material model parameters of flow stress and damage, both of which are commonly determined form the experimental stress-strain curves and fracture strains data through curve fittings. The variations in the material model parameters of different studies found in the literature are believed partly involved the errors in the data processing stage including the determination of the Bridgman correction factor, average stresses and strains curves, fracture strains, strain rate sensitivity parameters and etc. The automation of the data processing during the parameters determination will definitely reduce the extents errors arising from the human factor.

In the determinations of the Bridgman correction factor (*B*) based on Equation. 2.21 and σ_{eq} based on Equation. 2.22 requires

1) An accurate measurement of the R value, radius of curvature of necking, which is rather difficult by using video records
2) An accurate measurement of the value of a, radius of curvature of necking.

The determinations of the JC flow stress and damage parameters are usually performed by curve fittings using a graph program while the data read from the curves are entered by the user. Several steps are needed to obtain the material equations steps. All these fittings are also prone to the variations in the determined parameters between the different users.

The accurate material model parameter selection is also important. A comparison between the available data in the literature will allow users to detect the variations between the parameters reported in different studies. Once this comparison is seen then

appropriate model parameters can be screened by the users. Furthermore, the users should check the fidelity of the material model parameters obtained from the experimental tests with the published ones before entering then into a FE program. This allows them a comparison between their model parameters and the ones in the literature. The conversion of a specific material model equation into another model equation is also need in some occasion.

The main motivations for this thesis is the lack of any code available for determining

1) The Bridgman's corrections factor using video records
2) The average stress-strain curves
3) The JC flow stress equation parameters
4) Conversion of the JC flow stress equation into other equations
5) The JC damage parameter equations

There is also no data base on the JC flow stress and damage model equation parameters of common engineering materials for a comparison purpose. The main aims of these thesis are to developed a computer code in Python to determine Bridgman's correction factor, equivalent stress-strain curves, JC flow stress model equations and conversion of them to other equations, JC damage model parameters. A library of the JC parameters of common engineering materials was also included in the code.

CHAPTER 3

MATERIAL AND EXPERIMENTAL DETAILS

3.1. Quasi-Static and High Strain Rate Tests

316L and AISI 4340 alloys were selected in order to determine their constitutive equation parameters using the developed code. The tests on these alloys were performed in a project entitled TUBITAK-1505 5220017 CERAMIC ARMORS WITH ENHANCED BALLISTIC PERFORMANCES. The results of tests in this project were used as input to the code. The tension tests on above alloys were conducted in a 300 kN Shimadzu AG-X universal tension test machine at 10^{-3}, 10^{-2} and 10^{-1} s^{-1} at room temperature, complying with the ASTM E8/E8M-16 standard. The tension specimen sizes and their pictures are shown in Figure 3.1. Test setup and devices employed in the system are illustrated in Figure 3.2. The pictures of the tension test specimens with different σ^* values are also shown in Figure 3.3. A non-contact video extensometer was used to record the displacements and an external digital camera was used to record the deformation during the tests. At least three tests were performed at each strain rate.

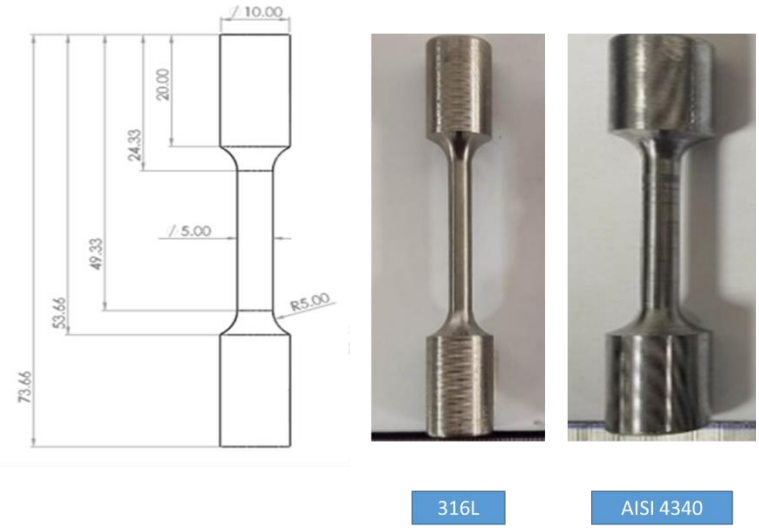

Figure 3.1. The sizes and the picture s of 316L and AISI 4340 tensile test specimens

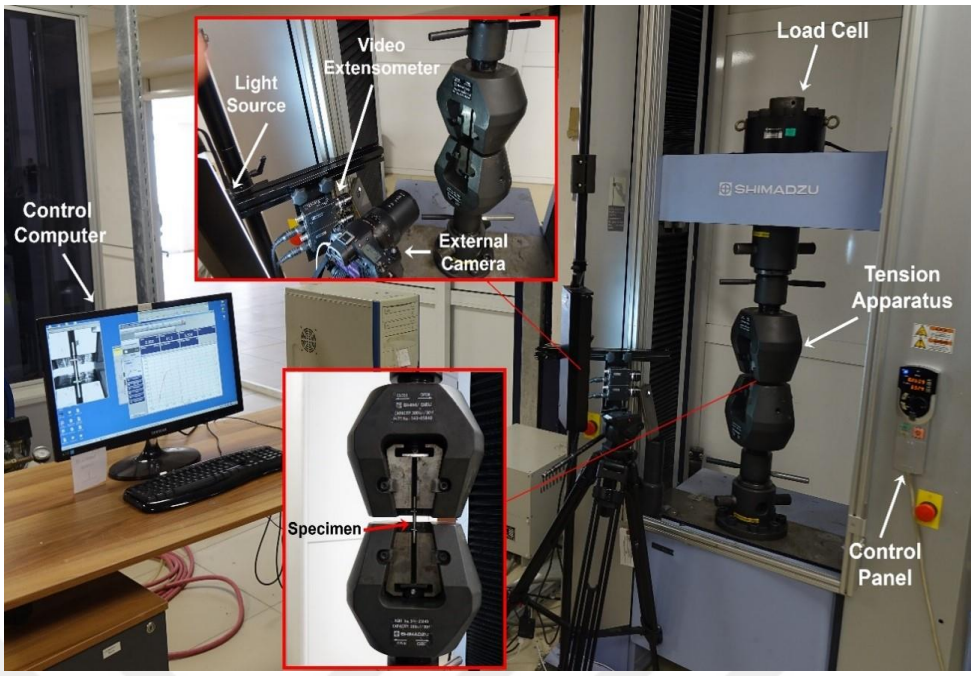

Figure 3.2. Quasi-static tension test setup.

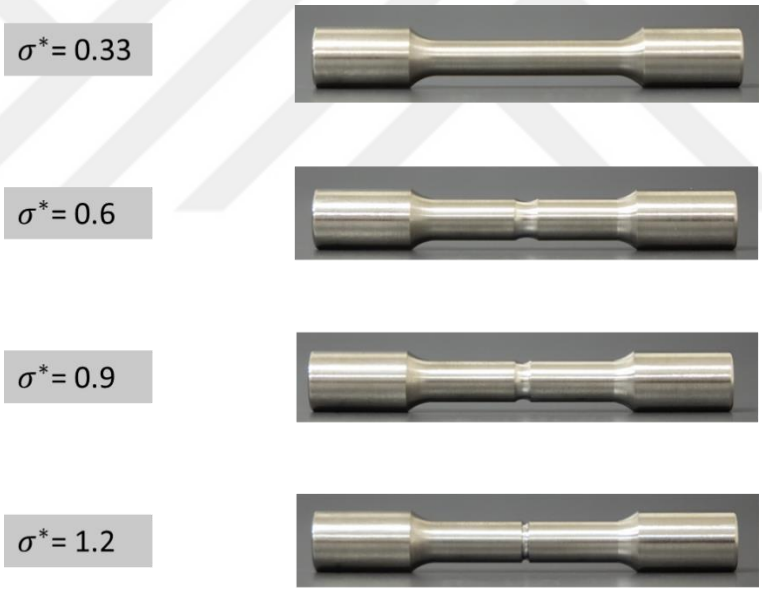

Figure 3.3. Tensile test samples with different triaxialities

High strain rate tests were performed in a SHTB set-up. The schematic and the picture of the used SHTB set-up are shown in Figure 3.4(a) and (b), respectively. The SHTB set-up consisted of a 316L alloy striker tube having a length of 500 mm and 316L alloy incident and transmitted bars having a length of 2410 mm and a diameter of 20 mm. The details of the used SHTB set-up are given elsewhere [113]. The elastic modulus, density and yield strength of the bar material are 193 GPa, 8000 kg m^{-3} and 300 MPa,

respectively. The strain (ε_s), stress (σ_s) and strain rate ($\dot{\varepsilon}_s$) of the specimen were calculated using the following relations

$$\varepsilon_s(t) = -\frac{2C_b}{L_s}\int_0^t \varepsilon_R(t)\,dt \tag{3.1}$$

$$\sigma_s(t) = \frac{A_b}{A_s}E_b\varepsilon_T(t) \tag{3.2}$$

$$\dot{\varepsilon}_s(t) = -\frac{2C_b}{L_s}\varepsilon_R(t) \tag{3.3}$$

where L_s, A_b, A_s, E_b, C_b and t are the specimen length, the bar cross-sectional area, the specimen cross-sectional area, the bar elastic modulus, the bar elastic wave velocity and the time, respectively. ε_R and ε_T are sequentially the reflected and transmitted strains. The size and picture of a SHTB specimen are shown in Figure 3.5. This image illustrates a typical setup for a Split-Hopkinson Tension Bar (SHTB) experiment, commonly used to determine the dynamic stress-strain response of materials at high strain rates. This setup allows researchers to understand the behavior of materials under high strain rates by analyzing the stress-strain response generated from the incident and transmitted stress waves.

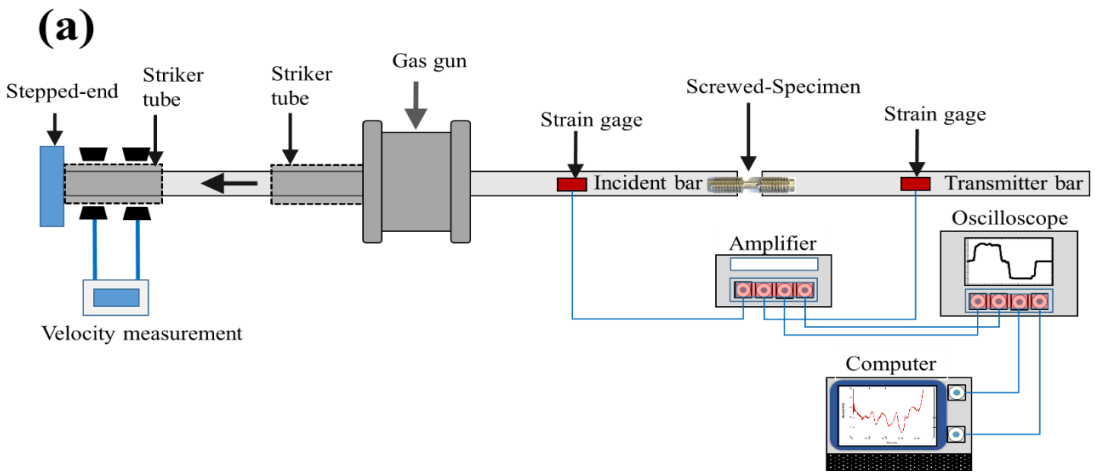

(cont. on the next page)

Figure 3.4. SHTB bar: (a) schematic and (b) the picture

(Source: Sarıkaya M. K. et al., 2023 [113])

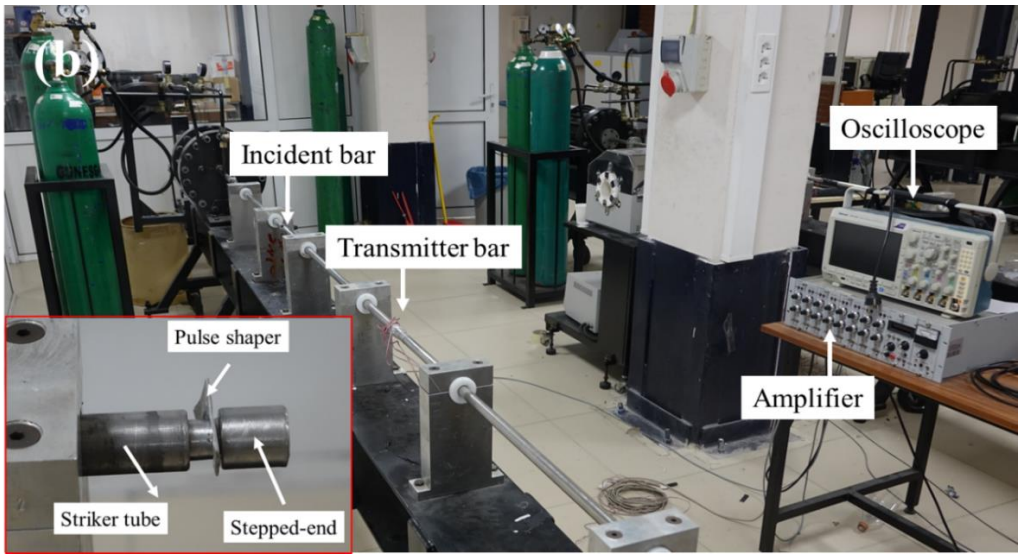

Figure 3.4 (cont.)

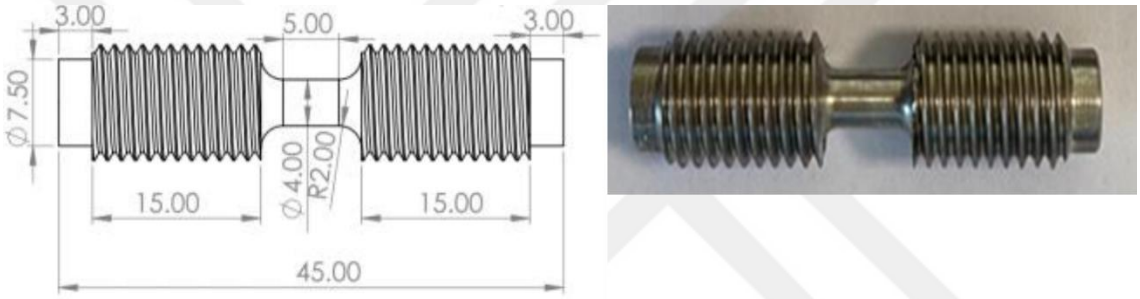

Figure 3.5. The size and picture of a SHTB test specimen

3.2. Calculation Methods

The steps to determine JC and ZA flow curves are depicted in Figure 3.6. The input to the program is the basic tensile test data, force and displacement as noted in Figure 3.6. The force and displacement data are then converted into engineering stress-strain curves using the initial length and cross-sectional area of the test specimen. Next, the trues tress-strain curves are calculated using the engineering stress-strain curves based on Equation 2.10 and Equation 2.11, respectively. The average true stress-strain curves are then determined using Equation 2.15 and Equation 2.27, respectively. The diameter of the necked region used in both equations is determined from the video records and therefore the video records of deforming specimens are input to the program. The equivalent stress values are the calculated using Equation 2.22 by determining the Bridgeman's correction factor and using Equation 2.28 by determining the MLR

correction factor. The JC parameters and ZA parameters are then determined by curve fitting. The *C* parameter is determined by curve fitting from the stress-strain curves at different strain rates.

The steps to determine JC damage parameters are shown in Figure 3.7. The quasi-static fracture strains at different stress triaxialities are used to determine D_1, D_2 *and* D_3 while high strain rate fracture strains along with the quasi-static fracture strain are used to calculate the damage parameter D_4.

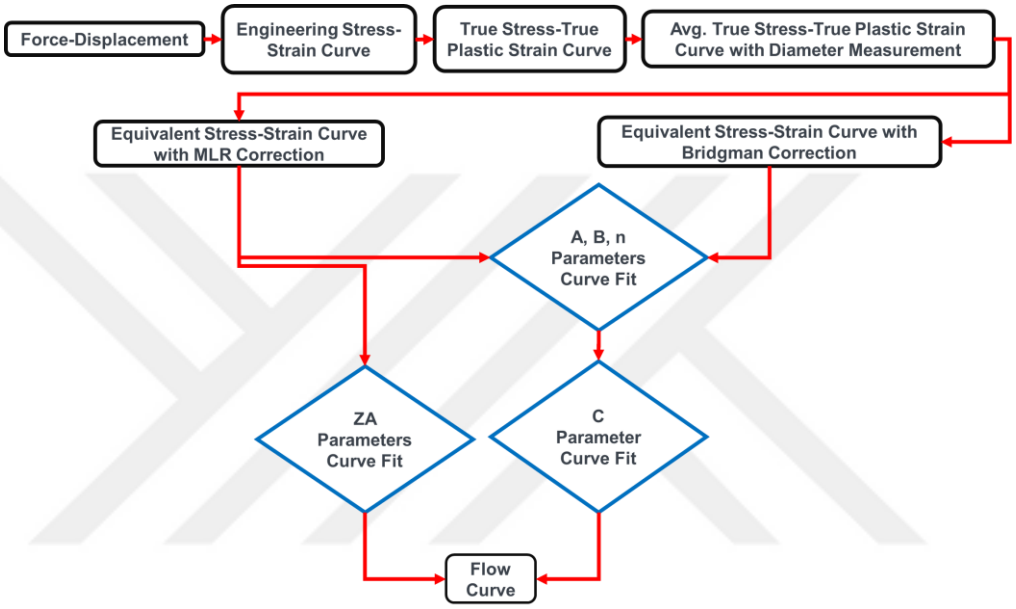

Figure 3.6. The processing steps to determine the JC and ZA flow curve

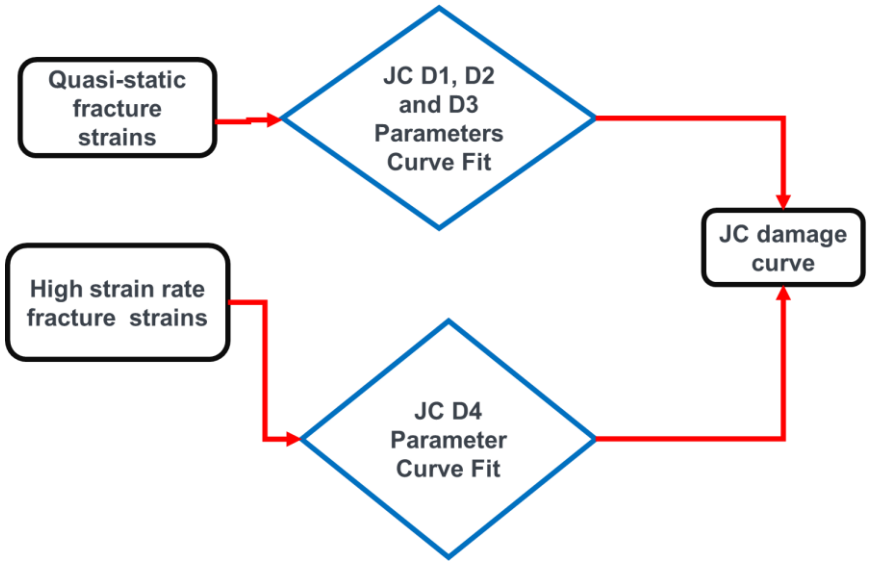

Figure 3.7. The processing steps to determine JC damage parameters

CHAPTER 4

INTERFACE DESIGN

4.1. The Interface for Determination of Equivalent Stress-Strain Curves

This chapter covers the complex process of developing a user-friendly interface for visualizing the average true stress-strain and equivalent stress-strain curves, and fracture strain-stress triaxiality relationships in the tested metals using the powerful combination of Python and the OpenCV library. The interface provides a comprehensive overview of the graphical user interface (GUI) of a software application that facilitates interaction with diameter and radius measurement data in the material necking region and their graphical representation on the image taken at certain time intervals over the sample tensile test video, as seen in Figure 4.1. This interface was designed using the OpenCV library prepared in the Python programming language and serves as an application for graphical visualization of the average true stress-strain and equivalent stress-strain curves and the fracture strain-stress triaxiality relationships. The GUI function produces various outputs required for analysis, documentation and further processing through advanced image processing and measurement logic. These outputs typically include annotated images that visually represent the measurements taken and data files that record the measured values. By processing image data, identifying contours, and calculating distances between specific points, this function provides a detailed analysis of material dimensions in real-time. Its integration with the OpenCV for image processing and Numpy for numerical calculations underscores the function's capability to handle complex image data and perform precise measurements.

This process begins with loading the material testing video file into the Python environment using the OpenCV. At equal intervals of time after the loading step, it is executed through the cv2.imread() function, which reads the image from the specified path and stores it as a multidimensional Numpy array. This array represents the image in the BGR (Blue, Green, Red) color space, which is a standard format for color images in OpenCV.

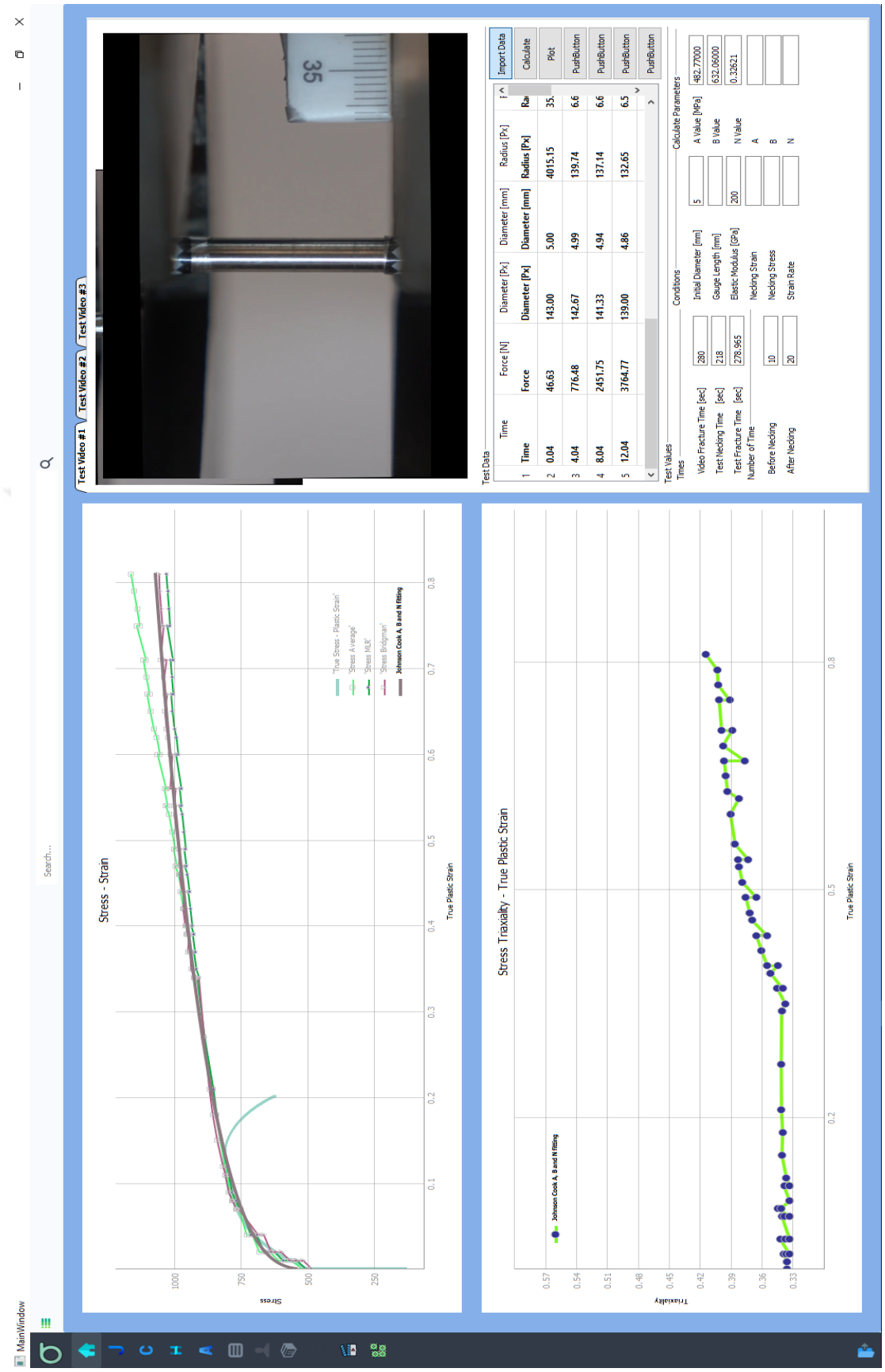

Figure 4.1. The picture of the code interface to determine average stress-strain and equivalent stress-strain curves and stress triaxiality

The next step is to apply grayscale conversion to the image. While color images are valuable for many applications, they can complicate the tasks focused on geometric analysis, such as diameter measurement. For this, converting the image to grayscale simplifies the data by reducing it to a single intensity channel and emphasizes the structural features of the object. This conversion is accomplished through the cv2.cvtColor() function, which converts the BGR image to a grayscale image. After grayscale, thresholding is made. Thresholding simplifies the image further by converting it to binary format, where pixels are set to black or white based on a specific threshold. This process increases the contrast between the object and the background, making it easier to detect edges and contours. Binary thresholding is performed using the cv2.threshold() function, where pixels with intensity values above the threshold are set to the maximum value (white) and all others are set to black.

After the image has been converted to a binary format through thresholding, the next step involves detecting the edges or contours of the object within the image. Contour detection is critical for understanding the shape and boundaries of the object, which are essential for accurately measuring its dimensions. In the given function, contour detection is achieved using the Laplacian operator, applied through OpenCV's cv2.Laplacian() function. The Laplacian operator is a second-order derivative method used in image processing to highlight regions of rapid intensity change, which are typically indicative of edges in an image. By applying this operator to the binary image, the function enhances the visibility of the object's contours against a uniform background. The output of the Laplacian operator is a new image that emphasizes the contours of the object. This contour-enhanced image serves as the foundation for the subsequent processes.

The second phase of the function focuses on defining the "Contour Analysis and Region of Interest" (ROI) identification in the processed image. The concept of ROI plays a fundamental role in digital image processing and allows focused analysis on the sections of interest in larger images. In applications requiring diameter measurement, accurate definition of the ROI is crucial to ensure measurement precision and efficiency. This process involves drawing the boundaries of the object of interest, thus reducing the computational load and increasing the accuracy of subsequent processing steps such as edge detection and contour analysis. The process begins with determining the vertical boundaries of the ROI in the image. This task is accomplished by scanning a predefined column in the processed image for significant changes in pixel intensity that are indicative

of the object's edges. In this function, the ROI is determined by scanning a predefined vertical line across the contour-enhanced image to detect the top and bottom edges of the object. Vertical scanning involves iteratively examining each pixel in a designated column, starting from the top of the image. The aim is to detect the first occurrence of a non-zero-pixel value indicating the presence of an edge, which is attributed to the Laplace operator applied in the image processing stage. Non-zero values in the contour map signify the presence of an edge. The search continues until the second significant change is detected, indicating the lower boundary of the object. These two points define the vertical range of the ROI. The goal here is to define the vertical boundaries of the ROI by scanning a predefined vertical line for edge points. The process starts from the top of the image and works downwards. When an edge point is detected, the Y coordinate is added to a list. Once the ROI is defined as vertical, the next step focuses on finding the left edge of the object within this region. This is accomplished by scanning horizontally across the image from a starting point within the ROI. The process looks for points where the Laplace output is nonzero, indicating an edge. Both the X and Y coordinates of these points are stored to represent the left edge of the object.

A similar approach is used to find the right edge of the object. However, the process adapts according to the number of iterations. For the first iteration, the scan starts from the Y coordinate corresponding to the middle of the left edge and moves horizontally from right to left. For subsequent iterations, scanning covers the full vertical coverage of the ROI. The function records the X coordinates of the leftmost and rightmost edges of the object at various vertical positions within the ROI. This method ensures that the narrowest part of the object is taken into account when measuring the diameter.

The third stage of the "Diameter Measurement Logic" phase important steps such as detecting edge coordinates and calculating the diameter and radius value of a sample in the necking region of the object in both pixels and millimeters. This phase is where the actual measurements are derived from the image data, following the preparation and ROI definition steps discussed previously. Diameter measurement in the context of image processing involves accurately locating the boundaries of the object and calculating the distance between those boundaries to determine the size of the object. For each pair of left and right edges detected along these rows, the horizontal distance between them is calculated and the narrowest distance in that particular row is represents the diameter. The calculated pixel distance between the left and right contours is converted to

millimeters based on the test sample reference diameter. The reference diameter (in millimeters) serves as a known reference value for a particular object or feature within the image. This reference is necessary to calibrate the pixels to millimeter conversion and effectively account for the scale of the image. To measure our radius value in the necking area, additional measurements are taken slightly above and below the point where our diameter value is measured along the Y axis. The function calculates the radius value passing through the left edge points at these points. The "Diameter Measurement Logic" phase combines edge detection with meticulous calculation to accurately determine the object's diameter within an image. By focusing on the widest part of the object and averaging measurements from multiple points, this logic ensures the reliability and precision of the diameter measurement. This phase showcases the application of computational geometry and image analysis techniques to solve practical problems, such as measuring physical dimensions from digital images.

The function draws a line for the diameter value in the necking region and a circle for the radius at the necking region on the image to visually represent the measured diameter and radius. These representations extend across the width of the object at the calculated average positions of the left and right edges and provide a clear indication of the measured area. In addition to lines, it adds text labels that display measured values in millimeters. A copy of the resulting annotated image is saved to disk, providing a permanent record of the measurement. OpenCV Drawing Functions is implemented using drawing functions provided by OpenCV such as cv2.line(), cv2.circle(), cv2.putText(). The display screen displays the annotated image in a widget, allowing the user to visually inspect the measurement results. The function saves the diameter and radius values calculated in time, pixels and millimeters, with details of each measurement in a text file. These recorded measurement values are later used for graphic analysis.

After these measurements listed, the script begins by reading a tab-delimited values file containing force and time data from an actual mechanical tensile test using pandas, the data analysis library. This step forms the basis for correlating video-derived metrics with testing data. The first phase of the function focuses on the process of reading and extracting critical information from a data file, specifically a file of tab-delimited values. This step of synchronizing video and test data is critical to accurately correlating the visual data captured in the video with the quantitative data recorded during the test, such as force and displacement. This process results in the structure of the data file as a

Pandas DataFrame, a two-dimensional labeled data structure with potentially different types of columns. When the data is loaded into a DataFrame, the script extracts the time values listed in the text file as a result of previous operations and the force values corresponding to those time values in the physical data file from the column related to the physical analysis and lists them in the relevant column in the relevant text. These columns contain time-stamped force measurements taken during material testing. The Time column represents the moments at which each measurement was taken, while the Force column records the magnitude of the force applied to the material at those moments. This extraction is simple in Pandas, individual columns can be accessed using header names such as file.Time and file.Force. With this extraction, it calculates these timestamps by aligning the video timeline with the test data timeline. This alignment involves adjusting for discrepancies between the actual test times (recorded in the data file) and the timestamps in the video file.

After the video processing stage, in which the diameter of the sample is measured at various times, these diameter measurements are required to be correlated with the force data obtained from the experimental test to calculate the average stress and strain, which depends on both the force and the geometric dimensions. Using Equations 2.12 and 2.13 for the relevant diameter and force data columns, the script calculates the average stress-strain values respectively, and the values are listed by creating a column in the text file for the calculated values. Synthesized data covering time, force, measured diameters, average stress and strain are compiled into a structured output file. This file serves as a comprehensive record of the analysis and facilitates subsequent studies or reviews.

After this process, the script first calculates the Bridgman constant B for the relevant diameter and radius data columns from the output file of the diameter and radius values measured at various times using the Bridgman correction constant Equation 2.21 to determine the equivalent stress after necking (σ_{eq}). A column for Bridgman's constant is created in the previously configured text file, and the calculated values are listed in the relevant column. To determine the equivalent stress behavior of the sample, Equation 2.22 was used. The equivalent stress values are calculated by substituting the relevant average stress column and the Bridgman coefficient constant column data calculated from the structured text file into Equation 2.22. The equivalent stress column is created in the structured text file for equivalent stress values, and the calculated equivalent stress values are listed in the relevant column. MLR method calculation, which is another method used

to find the equivalent stress, is Equation 2.28, and our strain data column, which is calculated and listed in the structured text, is calculated with the relevant MLR equation and our MLR constant values. By creating an MLR constant column in the structured text, our calculated MLR constant values are listed in the relevant column.

Apart from these calculation operations, the command line calculates engineering strain and engineering stress values respectively by using our force, extensometer strain values from the loaded physical test data file data, and creates columns in the physical test data text file, respectively, and engineering strain-stress values are listed in the relevant column. Then, our calculated engineering strain-stress data and true strain-true stress values are calculated and listed in the relevant columns created in the relevant text. To calculate our sample true plastic strain dataset, the function calculates the plastic strain by subtracting the elastic strain component from the total strain. Our calculated values of true plastic strain are listed in the relevant column created in the relevant text.

The command line has created two text files for the sample tested so far: the values calculated with the code and our physics data values. Our first text file contains our data columns obtained as a result of the calculations made on this tested sample video. This text file starts with a header line that names each column. These header lines are respectively; "Time", "Force", "Diameter [Px]", "Diameter [mm]", "Radius [mm]", "Average Stress [MPa]", "Average Strain [mm]", "Bridgman Constant", "Equivalent Stress -Bridgman- [MPa]", "MLR Constant", "Equivalent Stress -MLR- [Mpa]". Our second text file contains physical test data. The header lines of this text file are as follows; "Time", "Force", "Stroke", "Ext. Strain", "Eng. Strain", "Eng. Stress", "True Strain", "True stress", "True Plastic Strain".

After this process, the line of code visualizes the calculated values for the tested sample. From the text files created in our stress-strain graphic area in our interface, it first creates a graphical representation of the experimental data calculated as "True Plastic Strain" against "True stress" from our physical test data data text file, then "Average Strain" from our first text file and "Average Stress" against our data set, respectively. [MPa]", "Equivalent Stress -Bridgman- [MPa]", "Equivalent Stress -MLR- [MPa]" graphically represent the mechanical behavior of the tested sample material in the relevant graphic area. Thanks to this visualization capability, this function enables researchers and engineers to interpret experimental results and draw meaningful conclusions about the tested material.

The first phase of the interface, the "Preparation and Initial Processing" phase, includes several important steps focused on processing the input parameters and preparing the image data for subsequent processing and analysis. This phase ensures correct loading and pre-processing of the image, laying the foundation for accurate measurement. The "Preparation and Initial Processing" stage is foundational for the measurement function, ensuring that the image data is in an optimal state for accurate analysis. By carefully handling input parameters and applying targeted preprocessing techniques, this stage sets the groundwork for effective contour detection, dimension calculation, and ultimately, precise measurement of distances or dimensions within the image.

4.2. The Interface Design for Determination of Equivalent Stress-Strain Curve from Experimental Test Data for Johnson-Cook Strength Model

This interface section is designed to determine the equivalent stress-stain curves and *A, B, n* and *C* parameters of the JC flow stress equation using the experimental data. The interface is depicted in Figure 4.2. The equivalent stress-strain curves are determined using the MLR method. This interface is designed using the PyQt library prepared in the Python programming language. At the top of the interface there are three graphical visualization areas as shown in Figure 4.3. These are "Engineering Stress-Strain", "True Stress - True Plastic Strain" and "MLR - True Stress-True Plastic Strain". The third graphical visualization area shows the "Flow Stress-Strain" graph with the calculated *A, B* and *n* values, which are found as a result of the fitting process to the calculated "Equivalent Stress-Strain" graph of the sample using the MLR method on this graph. Under these graphic areas, as shown in Figure 4.4, there is table in which the first and second columns are the experimental Force and Displacement data, respectively. In the flowing columns sequentially the relevant calculated "Engineering Stress", "Engineering Strain", "True Stress" and "True Plastic Strain" data are included. "True Stress" and "True Plastic Strain" values are later used to calculate the JC parameters. This interface not only facilitates the calculation of crucial material parameters but also enhances the visualization and understanding of the stress-strain relationship in materials.

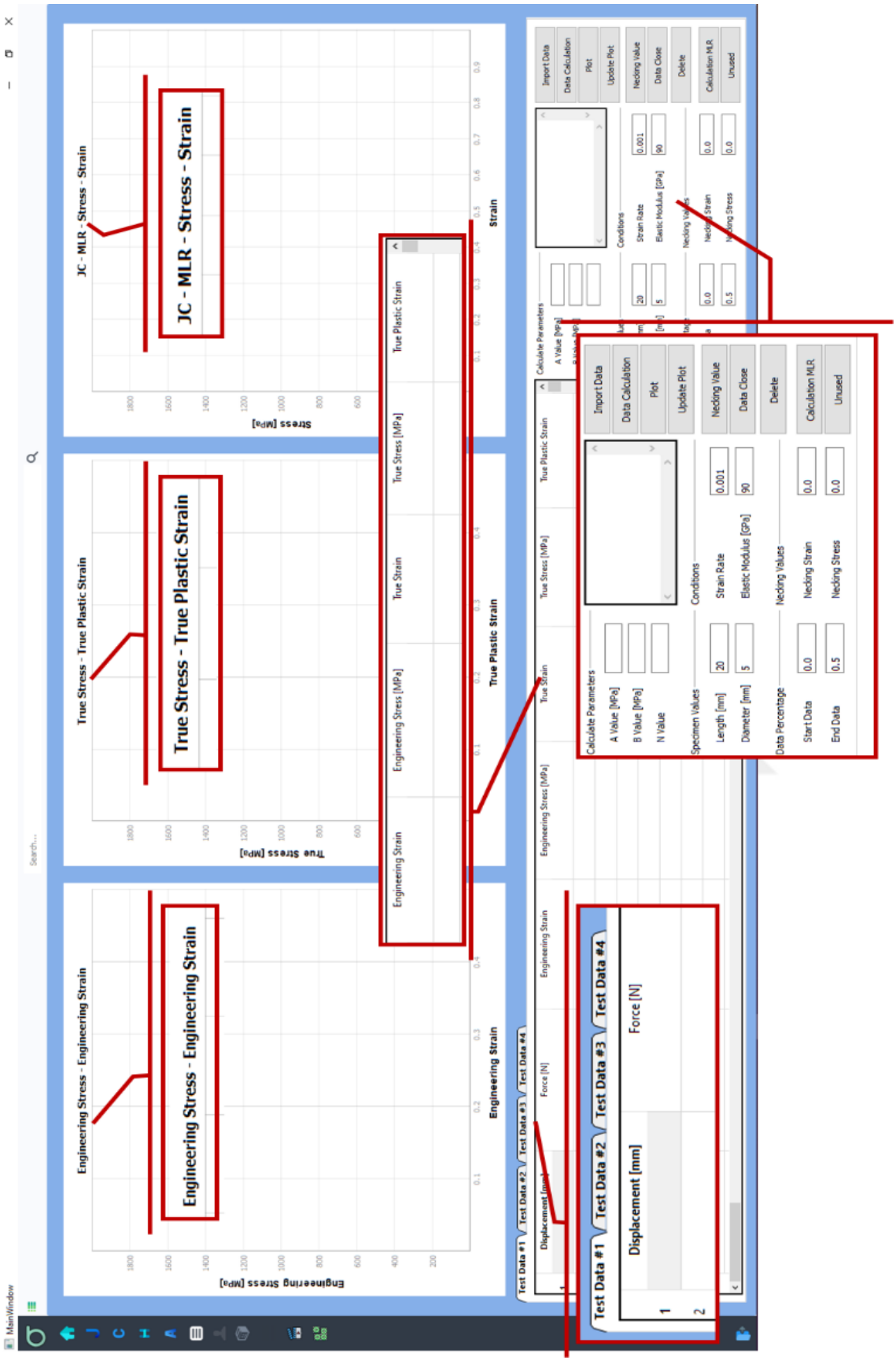

Figure 4.2. The interface design for determination of the equivalent stress-strain curve from experimental test data for the JC strength model

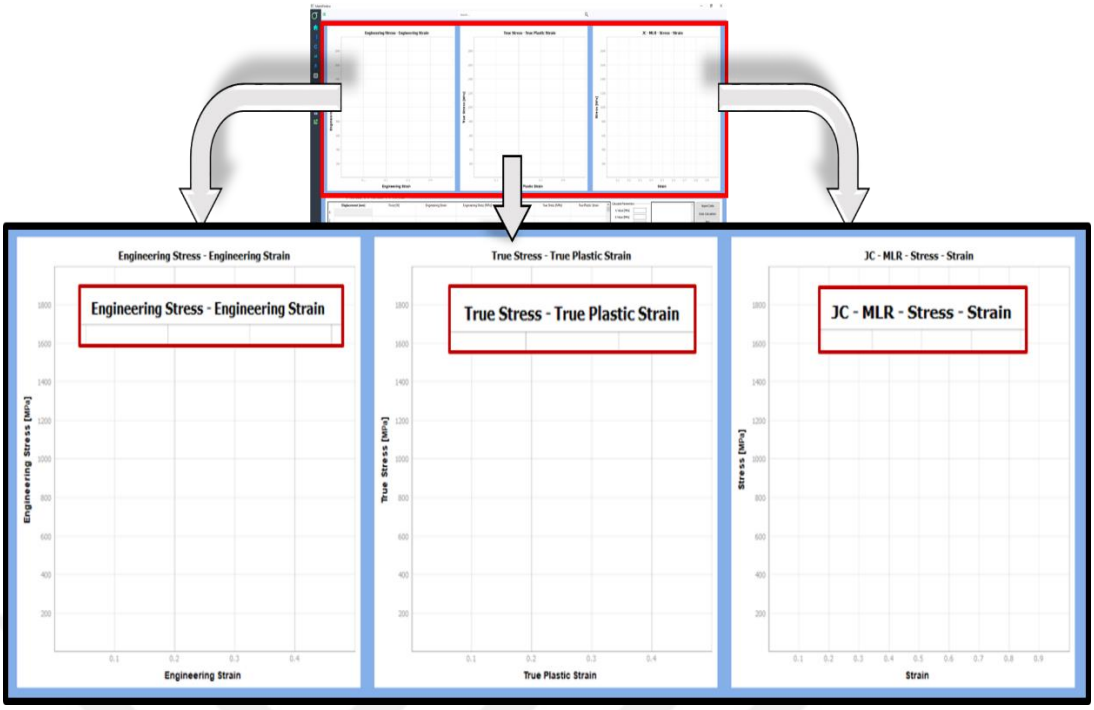

Figure 4.3. Visualization area of drawing experimental curve and JC strength equation at the interface

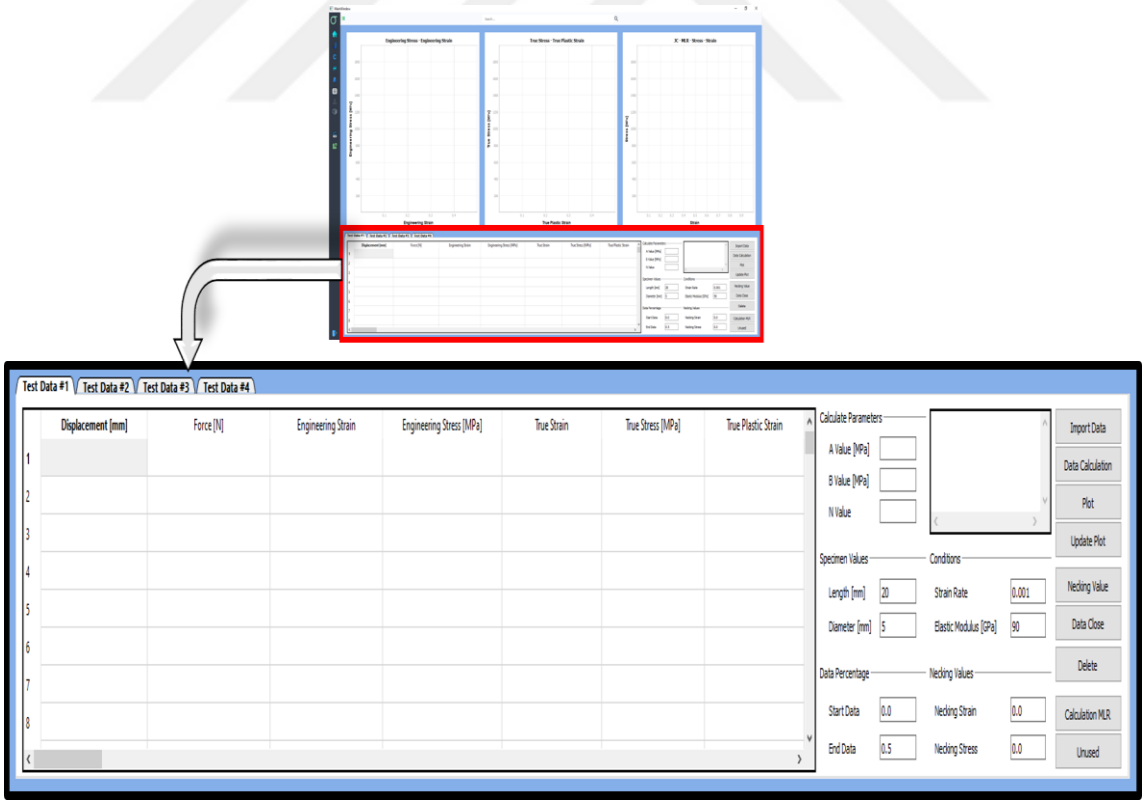

(cont. on next page)

Figure 4.4. Table of experimental data values and process parameters area

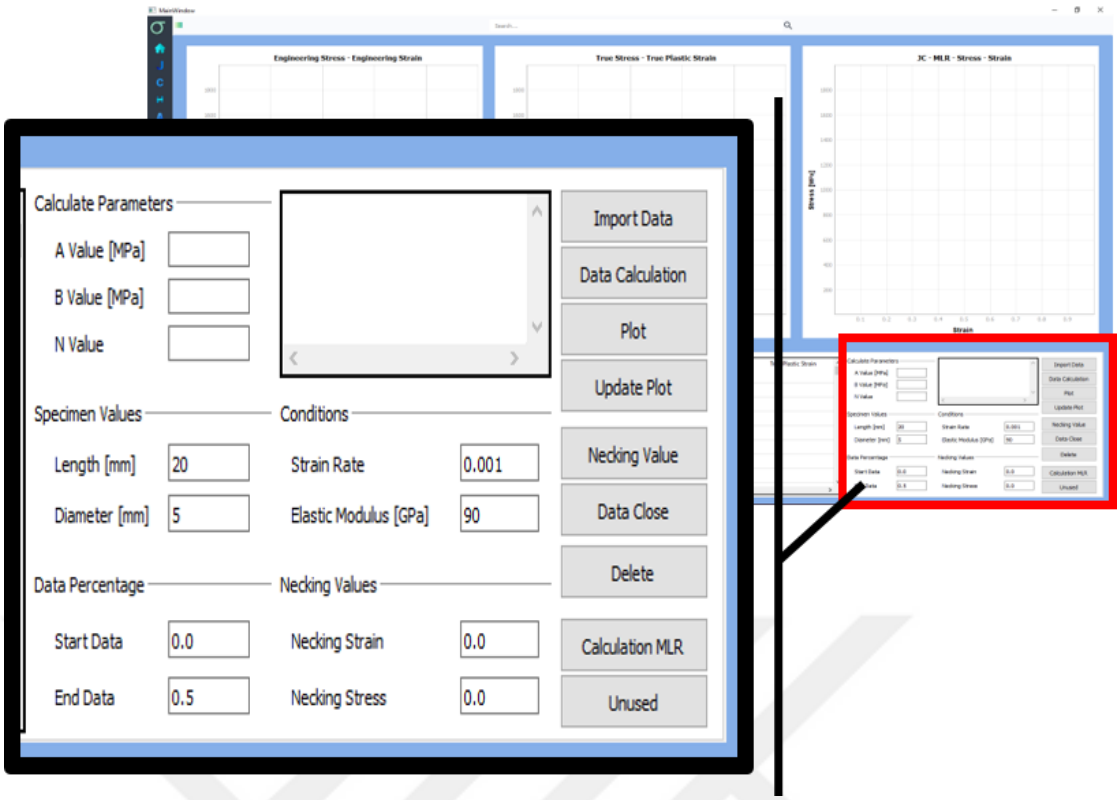

Figure 4.4 (cont.)

This PyQt-based interface facilitates the calculation of equivalent stress-strain curves and JC parameters (*A, B, n, and C*) using experimental data. It features graphical visualizations for various stress-strain relationships and a data table for experimental and calculated values. The MLR method is used for fitting and determining the parameters, streamlining the process for accurate material modeling.

This interface operation process is first uses "QFileDialog", a component of the PyQt framework, to open a local file selection dialog box with the help of a button to select the file containing the "Force-Displacement" data. This dialog box is configured to allow the user to select data files with specific extensions (.csv, .qda, .txt), ensuring that only compatible file types are selected for the processing. The file path selected by the user is retrieved and stored. This path is used to read and extract data from the file. The first column of the selected data files is set to be the "Force" data set, and the other column is set to be the "Displacement" data set. This step is very important as it forms the basis for all subsequent data manipulations and analysis. Depending on the file extension, the appropriate "Pandas" function is called to load the data into a "DataFrame". The data table "Table Widget (QTableWidget)" is configured to display data based on the number of

data columns and rows. "Force-Displacement" data from the "DataFrame" is filled into the table starting from the specified row.

After the data processing of the test sample is completed, the diameter and gauge length values are required to calculate the "Engineering Stress-Strain" values of the test sample entered into the relevant "QLineEdit" on the interface. After these entries, the "Engineering Stress-Strain" values are read by reading the "Force-Displacement" data required for calculation from the relevant column in the table by clicking the relevant button, and the calculated values are listed in the relevant "Engineering Stress-Strain" columns in the table. After the calculation, the "Engineering Stress-Strain" graphic representation of the tested sample is read from the table and the values in the relevant columns are drawn and a curve is drawn in the graphic area.

Following this process, the "True Stress" and "True Strain" values of the material are calculated from the "Engineering Stress-Strain" values, respectively, with the equations given in Chapter 2. The found values are listed in the relevant columns in the table. Another calculated value is "True Plastic Strain". The material elastic modulus value required for this calculation is obtained by entering the relevant linearity, dividing the material yield stress by the elastic modulus value and subtracting it from the "Total Strain" values. The obtained "True Plastic Strain" values are then listed in the relevant columns in the table. After the calculation process is completed, the values in the relevant column are plotted in the graphic fields.

After these operations, "True Plastic Strain" data column, corresponding to "True Stress" data column is drawn in the graphic visualization area. In order to perform this graph plotting process more smoothly, user-specified percentage values are entered into the relevant line edits to determine the proportion of data points to be excluded at the beginning and at the end of the data set. These percentages are converted into actual numbers of data points by calculating how much of the data at the beginning and end of the data set should be excluded from the analysis by multiplying the ceiling value of the total data points by the specified percentages. Based on the calculated exclusion numbers, the function is converted to our "True Stress" data column and "True Plastic Strain" determines the starting and ending points of the data to be used in the next analysis from our data column. For example, if the user enters 0.15 for the initial exclusion and the dataset contains 1000 data points, the function will draw the graph ignoring "math.ceil" (1000 * 0.15) = 150 points from the beginning of the dataset. This approach allows the

function to focus on analyzing the most important part of the data. In other words, plotting our data from the yield point of the material of our fitting process to the necking will enable us to perform the most accurate fitting process. Additionally, allowing users to specify exclusion percentages gives them control over their data analysis, allowing them to tailor the process to the specific needs and characteristics of their dataset. According to these adjustments, the "True Stress-True Plastic Strain" graphic representation is drawn in the relevant graphic area. In addition, the necking strain value of the test sample required for the MLR method equation, which we will use to obtain our equivalent stress-strain values in the later stages of the drawn "True Stress-True Plastic Strain" graph, is the strain value corresponding to our highest stress value of this graph, which will later be used in the MLR equation. It is printed in the relevant section with an interface. The printed necking strain value can be changed if the user wishes.

The next phase involves the preparation for the curve fitting, application of the model to the data, and improved graphical representation of the fitted model. The fitting process is carried out to obtain the *A, B and n* parameters. Initial estimates for model parameters are set based on data or predefined values, and the nonlinear least squares method (curve_fit from SciPy) is used to find optimal parameters that minimize residuals between observed data and the model. To visually evaluate the quality of fit, the fitted curve is plotted together with the raw data. Displaying these results directly in the interface allows users to instantly grasp the material properties and understand how well the model fits the experimental data. Then, the most appropriate parameters obtained are substituted into the equation and "Flow Stress-Strain" graph for 1000 points between zero and one of our strain value is displayed in the same graphic area, allowing users to quantitatively evaluate the behavior of the material under stress and verify theoretical models according to experimental data. The optimized parameters (*A, B, n*) as well as other important results from the analysis are displayed in the GUI, specifically within designated QLineEdit widgets and a text area. These widgets serve as display areas where users can easily view and interact with parameter values.

The "Flow Stress-Strain" graph is also drawn in our third graph area, and this graph is calculated using the MLR method equation to obtain the equivalent stress-strain graph to observe the behavior of the tested material after necking based on the used data. The equivalent stress-strain values, which are found in the MLR equation and the necking strain value we found previously, are read from our relevant line edit. The equivalent

stress-strain values are obtained by calculating each strain value of "Flow Stress-Strain" graph and multiplying strain value at each point with the corresponding flow stress values. The resulting equivalent stress-strain graph is drawn in the third graph display area. In this graph, the fitting process is performed to obtain the *A*, *B* and *n* parameters of the JC strength equation. As before, the fit process uses the curve fit method in SciPy's optimization library, which implements nonlinear least squares fitting. The estimated optimum parameter values are added to the printed text of the parameters found in the previous fit process in this interface. These are the operations performed on test data at a certain strain rate in this interface. The same procedures are performed for calculations of different strain rate test data. The *A, B,* and *n* values obtained from the equivalent stress-graph obtained at the end of each test data calculations are printed on the relevant interface and in the relevant line edits with the reference strain rate value to calculate the *C* parameter, which is the strain rate effect parameter of the JC strength equation.

By calculating the material test data performed at 4 different strain rates in this interface, the *C* parameter will be ready for calculation. The interface is designed to update the user interface in response to changes in the internal state or upon completion of analyses. For example, if a new data set is loaded or a new set of parameters is calculated, relevant parts of the user interface are automatically refreshed to reflect these changes. As a result of these four different test data calculations, this interface will complete its operation. As a continuation of the results obtained here, the operations continue in the *C* parameter calculation interface.

After performing the operations on 4 different strain rate data in this interface, we now move on to the *C* parameter calculation interface. This method is designed to analyze stress-strain relationships for materials under various conditions using a set of user-defined input parameters. It integrates data extraction, curve plotting, interpolation, and nonlinear curve fitting to provide information about the material's behavior under stress and improve the understanding of its mechanical properties. This computation is performed for multiple sets of parameters, resulting in multiple stress-strain curves that the function will later plot. This interface, as shown in Figure 4.5, calculates the JC strength model *C* parameters and plots the values of the *A, B* and *n* parameter sets found in 4 equivalent stress-strain graphs calculated in the previous interface. Drawing the relevant graphs in the interface, graphical visualization of the *C* parameter calculation method, batch fitting process like the previous fitting process to our 4 different graphs to

reduce our 4 different strain rate *A*, *B* and *n* data to a single parameter *A*, *B* and *n*, and the calculated *C* value. The *A*, *B* and *n* values, which are reduced to a single parameter set with, are graphically displayed with the JC strength equation for each strain rate value of 4 different strain rate test data. Additionally, there is a control panel where the *A*, *B* and *n* values calculated in the previous interface are printed and necessary for the *C* parameter.

In this interface, first of all, the *A*, *B* and *n* parameters, calculated separately from the "equivalent stress-strain" graph for each of the material data tested at 4 different strain rates in the previous interface, are printed in the relevant lineEdit boxes in this interface, together with each strain rate value. These printed data set values are calculated graphically for *1000* points between *0* and *1* of the strain value in the JC equation with the help of a button. For each strain rate data, the "Equivalent Stress-Strain" graphs are drawn in the relevant graphic display area. After this drawing process, we start calculating the JC strength model *C* parameter value.

The JC material model *C* value calculation is carried out as follows. First of all, the user enters the starting and ending values of the strain values user wants to calculate between the 4 different strain rate test data graphs drawn into the relevant box. The number of points at which the stress values between the entered values are desired to be included in the *C* value calculation is entered in the relevant box. The number of points entered will be the corresponding strain values in the selected strain range. The stress values at the relevant points in the strain rate chart for each of these strain values are drawn on the *C* parameter calculation chart. In other words, 4 different strain rate values are added to the *X-axis* and the corresponding stress values are added to the *Y-axis* in these value graphs. Each strain value of the existing strain values as many as the entered number of points will have 4 stress values coming from 4 different strain rate graphs. These four stress values will create a data set for *C* value calculation. A "*C"* value calculation data set will be created as many as the number of points entered. The *C* value calculation is performed separately for each data set. That is, whatever the number of points, the *C* value is calculated for each of them. The average *C* value is obtained by adding each *C* value found and dividing by the number of points. The fit graph assigned to each data set is shown on the data sets. This visual representation allows users to see how well the model fits the experimental data for each individual data set. This average *C* value is then printed both in the graphical visualization area and in a dedicated box within the interface.

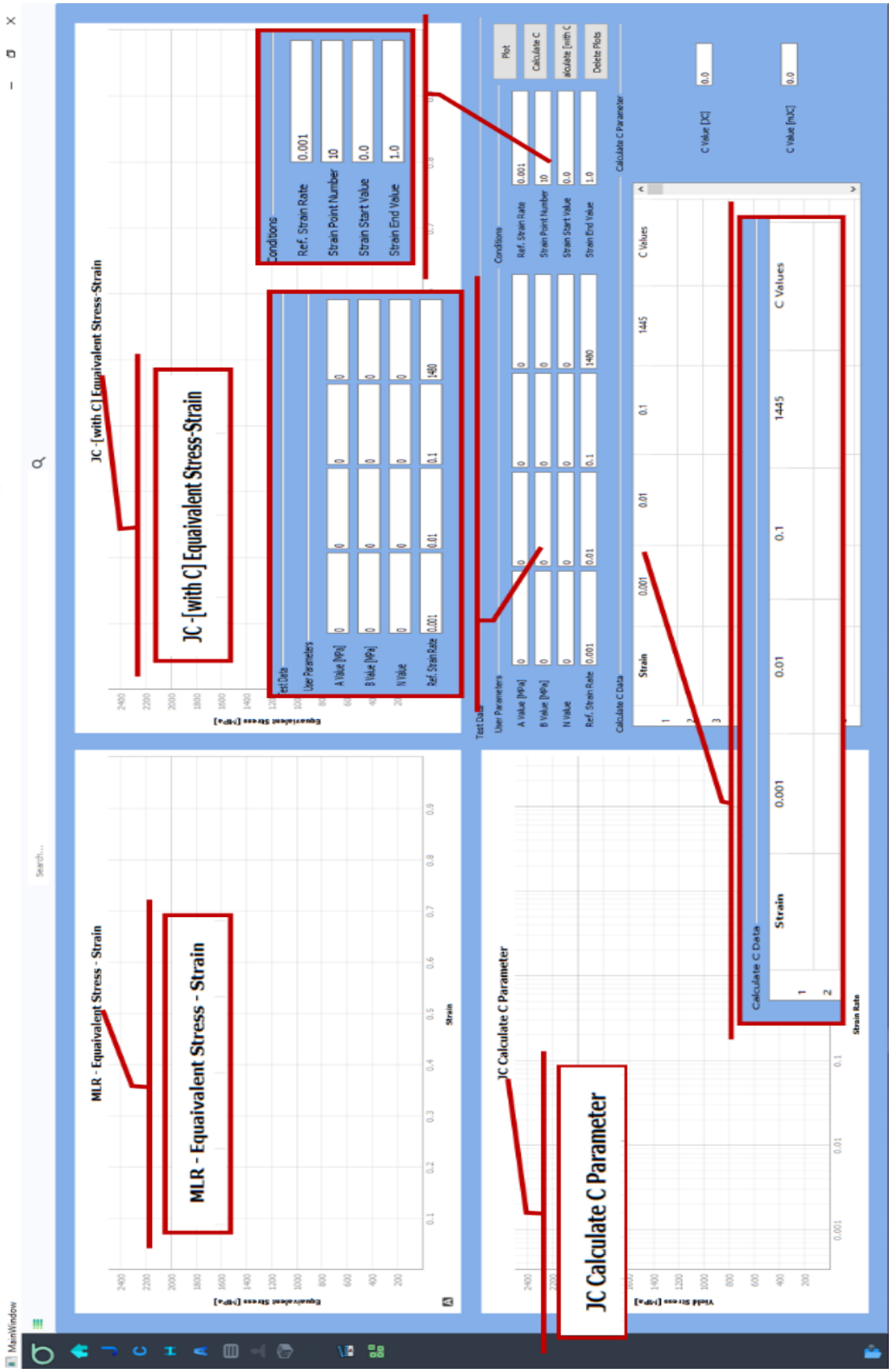

Figure 4.5. Interface design for calculating the JC strength model *C* parameter value and determining the equation results

To explain the process with an example, let's say a test material was tested at strain rate values of *"0.001", "0.01", "0.1"* and *"1000"*, respectively. The "Equivalent Stress-Strain" curves are calculated and drawn for the *A, B* and *n* values calculated for each strain rate value and the *1000* strain values between *0.0 – 1.0*. For the *C* parameter calculation, let's say the user wants to calculate the *C* value with the stress values corresponding to the *50* point between *"0.0"* and *"0.25"* from our strain values between *0.0 – 1.0*. In the *C* calculation graphic area, our strain values at 50 points in each strain rate graph, corresponding to our strain rate values on the *X-axis*, are drawn in the graphic area with corresponding stress values with dot symbols. Thus, *50* data sets are created for *C* value calculation. For each data set, the 50, *C* value is calculated by adding *50* fitting for the *C* value of the strain rate effect parameter of the JC material equation. The average *C* value is calculated by adding up the *50* values found and dividing by the total number of values.

After calculating the average *C* value, the lowest strain rate value is accepted as the reference strain rate in our "Equivalent Stress-Strain" graphs drawn with four different strain rate *A, B,* and *n* parameters. Batch fitting is performed to reduce four different *A, B* and *n* data sets to a single *A, B* and *n* data set. The fitting process accepts the *A, B* and n values found from the lowest strain rate graph as initial guess for the *A, B* and *n* values. The *C* value we found takes its place in the equation. The reference strain rate value in the strain rate effect section is taken as the lowest strain rate value. Another parameter in the equation is the strain rate parameter. Each strain rate value is assigned to our strain rate parameter from smallest to largest. Batch fit assignment is made to each strain rate graph with a single *A, B, n and C* value, just like the previous fit methods. To obtain the test graphs made at four different strain rates, by simply entering the strain rate value in the equation, the actual experimental test data graph and the material model parameters that converge to the same graphic data are obtained.

The *A, B and n* values obtained as a result of the batch fit process are printed in the relevant box on the interface. Then, the *A, B, n* and *C* values we found with the JC strength equation, the referenced strain rate value are added to the relevant equation, our strain range is calculated for *1000* of data between *0-1*. With the strain rate parameter in the equation, stress values are calculated separately for the strain rate values of the processed test data. Then, a graph of the material stress values found for each strain rate is drawn. With this graphical drawing, we can compare the graphs drawn with the *A, B and n* values calculated separately for each strain rate from the "Equivalent Stress-Strain"

graphs, and the results of the *A*, *B* and *n* values found by reducing them to a single value with the fitting process. offers the opportunity. These graphs show the user how well they match the real "Equivalent Stress-Strain" graphs and how accurate they are. In such tests, if test data processing at high strain rates is included, heating occurs in the material due to adiabatic heating that occurs during the test. Due to this heating, after the dynamic test data reaches a high stress value at the beginning, our stress curve will be downward due to heating, that is, the graph has a stress value above the yield point region of our static test result graphs, and due to the start of heating, we cut the stress graph of static tests at a certain strain value, the stress graph is static tests have stress values below the stress graph. In this case, since the stress values of the static tests have similar graphic curves in the batch fit process, as a result of the batch fit process to these similar curves, results that are more compatible with the material's actual stress value graph are obtained. However, since the inclusion of a test data performed at a high strain rate is different from the static stress values, in this case, the batch fitting process will cause a stress curve that converges to the result of the real stress test data performed at a high strain rate, losing the harmony and accuracy of the fit parameters obtained. The aim of this fitting process is to find the most converging combination of *A, B* and *n* values.

4.3. The Interface Design for Determining Johnson-Cook Failure Model Parameters from Experimental Test Data

This interface section provides the interpretation of the fracture strain value when our damage constant values of JC failure equation parameters 'D_1, ' 'D_2, ' 'D_3, ' ' D_4, ' have different stress triaxiality values with the data obtained from experimental data, as seen in Figure 4.6. It is designed to graphically visualize the "Fracture Strain-Stress Triaxiality" graph of the test sample calculated by finding equation parameter values. The graphic areas in the interface are graphic area where the results of calculating the D_1, D_2 and D_3 values of the JC failure model parameters are graphically displayed, respectively. The second graphic area provides a graphical representation of the calculation result of the D_4 damage constant value.

Below these graph areas are data tables that list the input values obtained from the test data for damage parameters. The first of these tables lists the values of the tests performed at different stress triaxiality values obtained from various test data to calculate

the D_1, D_2 and D_3 values and the fracture strain value of each of the tests. The second table contains a table that lists the fracture strain results of tests performed at different strain rate values at a single stress triaxiality value required to calculate the D_4 parameter. Test results required for the parameters are structured in a table that allows the user to select files with specific extensions (.csv, .txt) relevant to data analysis with the help of a button. If the user wishes, he can manually enter the values in the relevant columns in the table into the table instead of uploading the file containing the test results. The tables are standardized so that for D_1, D_2 and D_3 values, the first column is stress triaxiality values and the second column is fracture strain values. In the D_4 table, the first column is stress triaxiality value, the second column is fracture strain values and the third column is strain rate values. Finally, there are relevant boxes in the interface where calculated D_1, D_2, D_3 and D_4 values are printed.

In order to find the parameters in the damage equation, notched sample tests with more than one test sample at different stress triaxiality values are also required to calculate D_1-D_3 values. First of all, the file containing the stress triaxiality and fracture strain values of the tested samples at different stress triaxiality values is listed in the columns in the relevant table with the help of a button or manually. "Stress Triaxiality" values versus "Fracture Strain" values are plotted in the relevant graphic area of values in the table. After the plotting process, the D_1, D_2 and D_3 values of damage constants are calculated and the D_1, D_2 and D_3 values of the JC failure equation are obtained by the curve fitting method to the plotted data. By substituting found values into the equation, calculated data is plotted on top of curve-fitted data. This provides the opportunity to compare applied curve fitting chart with test data. The calculated D_1, D_2 and D_3 values are printed in the relevant boxes on the interface.

After this process, we start calculating our other damage parameter, D_4 value. In calculating the D_4 value, the file containing the fracture strain values of the tests performed at different strain rate values of samples with a single stress triaxiality value is listed in the relevant table. After listing, the data is plotted against "Strain Rate" values versus "Fracture Strain" values in the relevant graphic area. After the plotting process, the D_1- D_3 values we found are sent to the JC failure equation for curve fitting. Calculating the D_4 value on drawn "Strain Rate-Fracture Strain" graph. The found values are substituted into the equation together with the D_4 value, and the calculated data is plotted on the curve-fitted data.

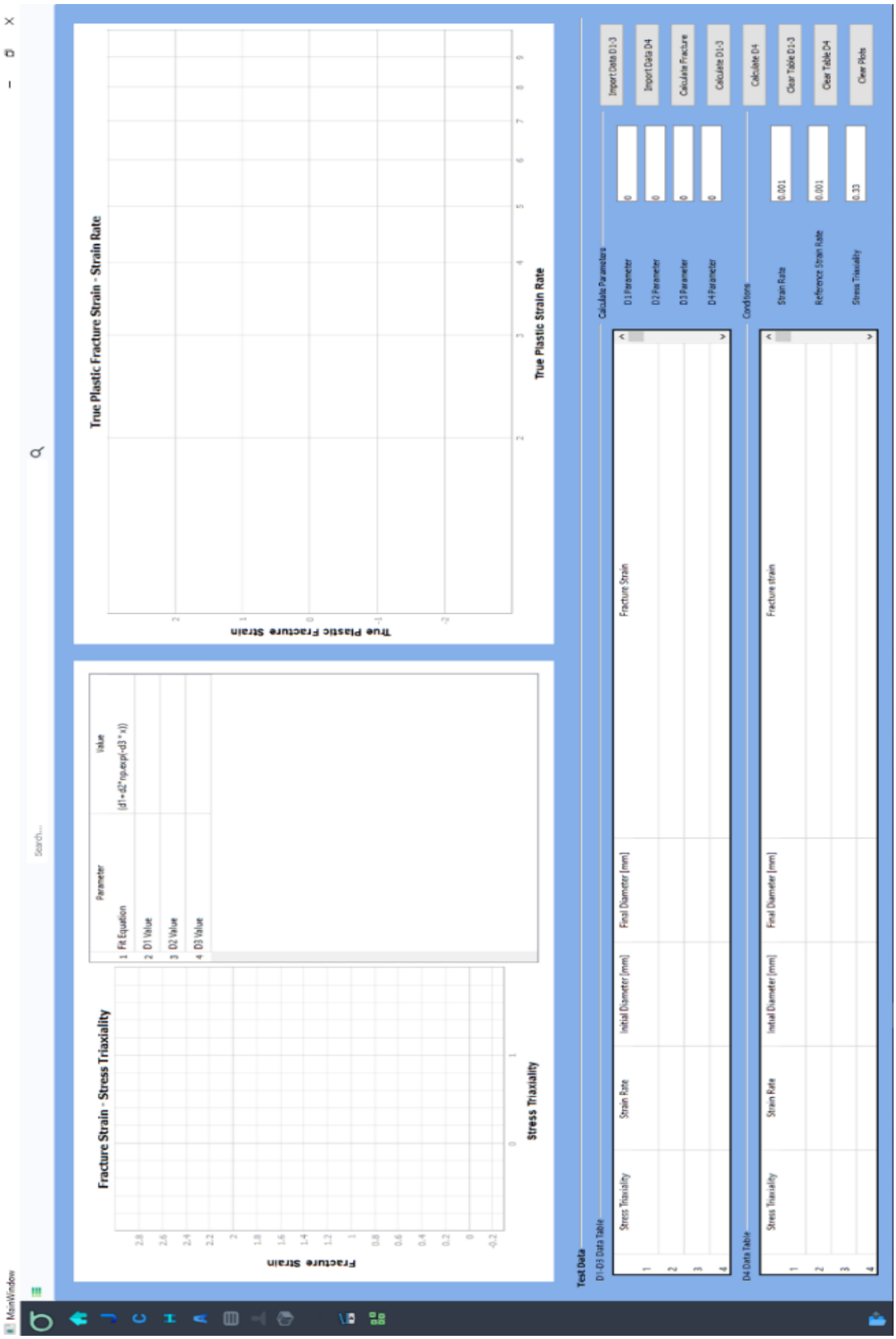

(cont. on next page)

Figure 4.6. Interface design for calculating JC failure model parameter values and determining equation results

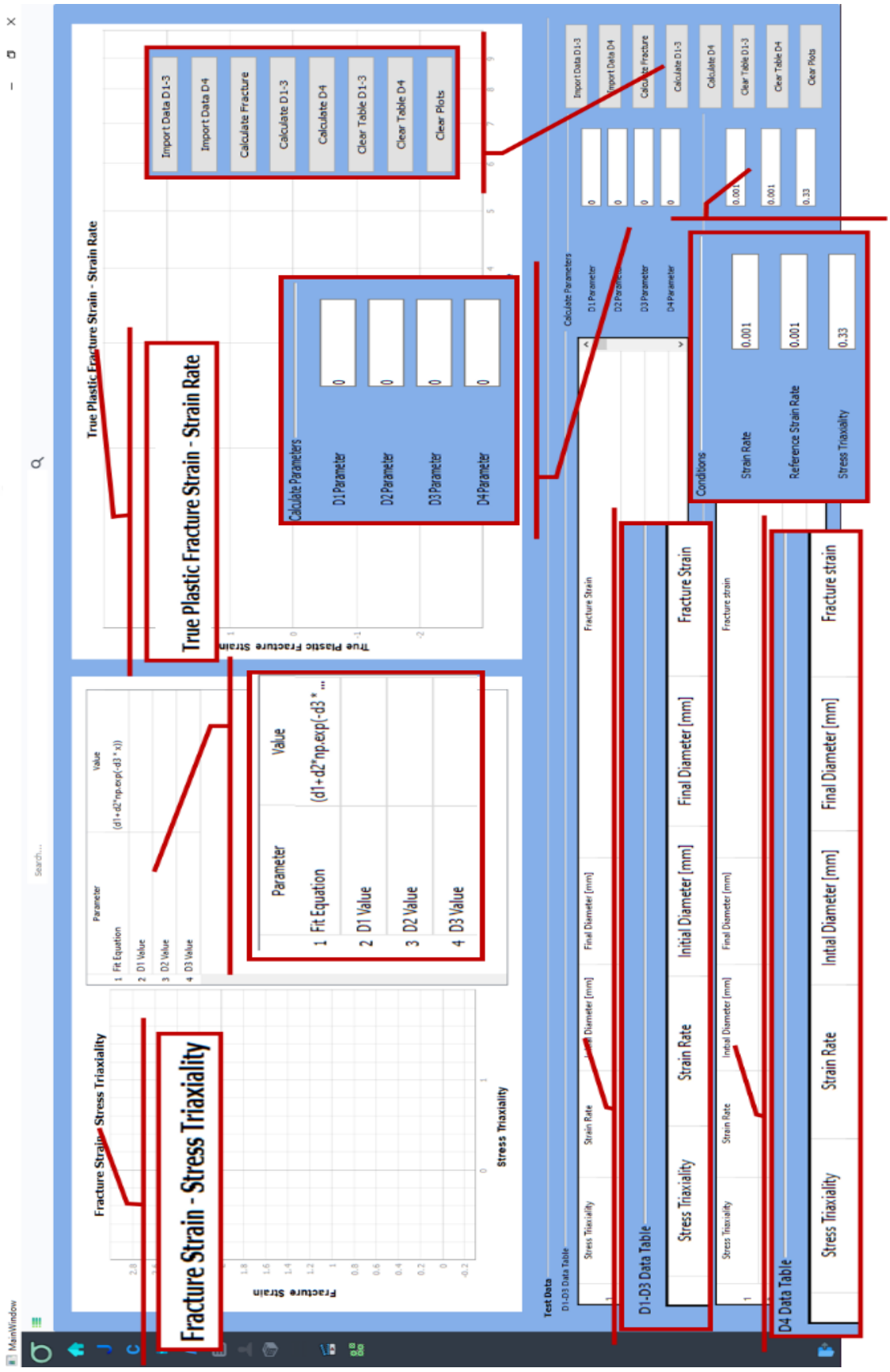

Figure 4.6 (cont.)

4.4. The Literature Data Interface for the Johnson-Cook Models

This parts covers the complex process of developing a user-friendly interface for visualizing stress-strain and fracture strain-triaxiality relationships using the powerful combination of Python, PyQt, and Pyqtgraph libraries. As seen in Figure 4.7, the JC equations for the strength and damage provide a comprehensive overview of a software GUI that facilitates the user's interaction with material data and their graphical representation. This interface was designed using the PyQt library, prepared in the Python programming language, and serves as an application for entering parameters into JC models and visualizing the resulting stress-strain relationships and failure strain-stress triaxiality of selected materials. The GUI is partitioned into several distinct areas, each serving specific functionalities such as literature data comparison, stress-strain analysis, and fracture strain-stress triaxiality correlation. Two primary sections dominate the GUI: the upper region that visualizes data through graphs and the lower section that presents the data in tabular form and offers additional controls for user input and data management (Figure 4.6).

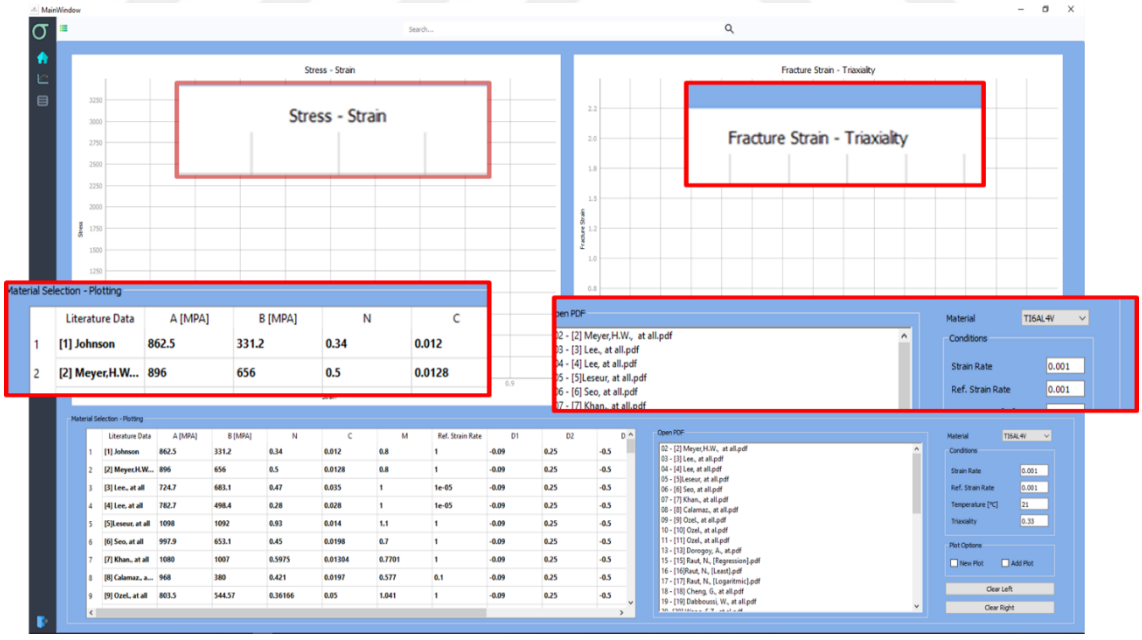

Figure 4.7. The literature data interface for the JC strength and damage models

There are two graphics side by side at the top of the interface, as shown in Figure 4.8. These graphs are intended to display graphical data regarding the behavior of the

material under stress and the conditions that lead to its fracture. The plots are central to the analysis process as they will display calculated stress-strain curves derived from the JC strength model and fracture strain data as a function of triaxiality obtained from the damage model, respectively. The first graph is labeled "Stress-Strain", which corresponds to the JC strength model. This model characterizes the flow stress of materials as a function of strain, strain rate, and temperature. The chart is intended to plot the stress in the y-axis (in MPa) against the strain in the x-axis. The Stress-Strain graph is typically used to show the relationship between the stress applied to a material and the resulting strain; this is a fundamental property in understanding material behavior. The second graph is titled 'Fracture Strain – Triaxiality' which will be associated with the JC damage model. This model predicts the onset of damage in a material based on the strain at fracture and stress triaxiality (a measure of deviation from pure shear stress). In the graph, the x-axis represents triaxiality, which is a factor that defines the type of stress state, and the y-axis represents the fracture stress, which is the stress at which the material will break. Stress triaxiality is a very important factor in the study of fracture mechanics as it affects the way materials fracture when subjected to multiaxial stress states.

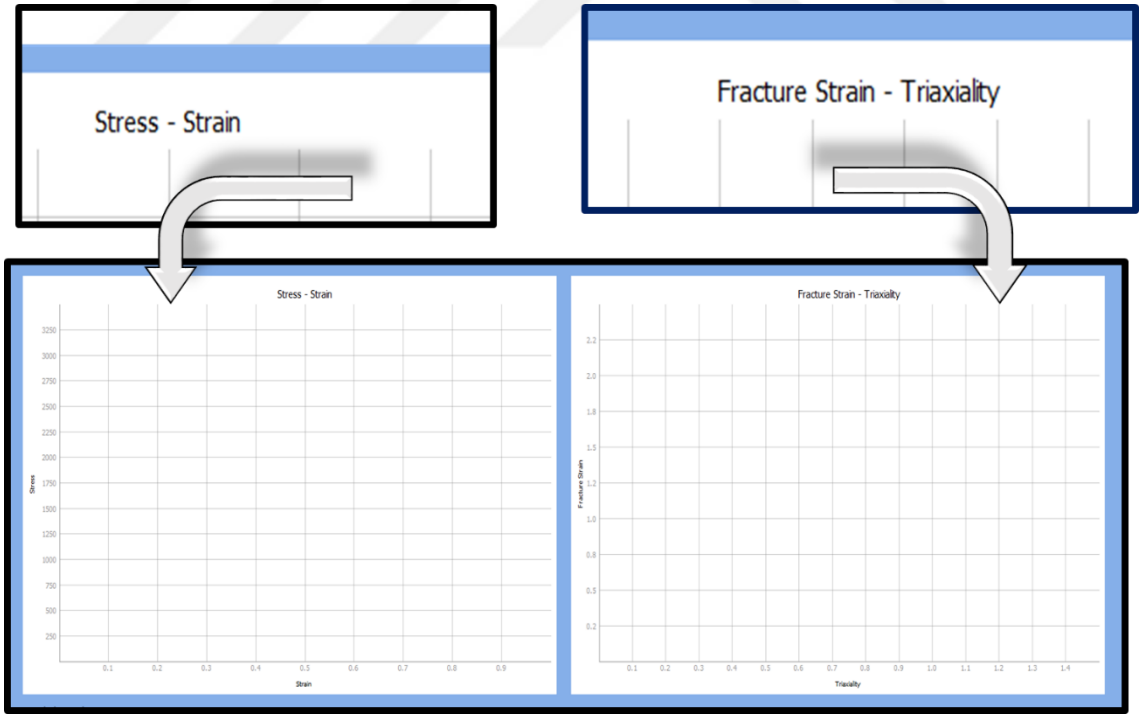

Figure 4.8. The JC strength and damage equation plot area at the interface.

Below these graphic areas is a tabular data table titled "Material Selection - Plotting" filled with parameters taken from the literature, as shown in Figure 4.9. This table contains numerical data from various studies (referenced by the author names and study identifiers) and is compiled for comparison and selection purposes into a database of material properties. The data correspond to coefficients and parameters used in predictive models of material behavior. This table lists various datasets from literature sources, as indicated by columns titled 'Literature Data, ' 'A [MPa], ' 'B [MPa], ' 'N, ' 'C, ' 'M, ' 'D$_1$, ' 'D$_2$, ' 'D$_3$, ' 'D$_4$, ' 'D$_5$, '. These headers correspond to the coefficients and parameters used in the JC models. Data input into the GUI is facilitated through an interactive table, where users can enter material properties and coefficients for the JC equations. The table is a data table that serves as a store for these literature data and can be used to compare with calculated results from JC models. The GUI processes this input to calculate the stress-strain and fracture responses of materials, with the results plotted in real-time, providing immediate visual feedback. The literature data table not only serves as a store of empirical data but also as a means to plot and compare these values on the graphs above. Each entry in the table corresponds to a dataset, with parameters such as stress and strain rates critical for plotting the respective curves. The table includes numerical values and identifiers, such as ' [1] Johnson et al., ' ' [2] Meyer,H.W., ', implying a compilation of research findings or experimental results that can be plotted on the graphs above.

In summary, in the interface, the user is provided with a database of literature data, as seen in the table, which includes values of these parameters obtained from various studies. The user can select different data sets corresponding to different materials or conditions, allowing them to quickly simulate different scenarios and visualize the predicted stress-strain and fracture strain-stress triaxiality relationships using graphs at the top of the interface. This table allows for the input and display of relevant literature data, facilitating easy access and comparison of various material properties sourced from academic papers. By integrating these functionalities, the interface not only simplifies the exploration of material properties but also supports informed decision-making in engineering applications that rely on accurate and comprehensive material characterization. This capability is crucial for optimizing designs and ensuring reliability across different operational contexts within the field of materials science and engineering.

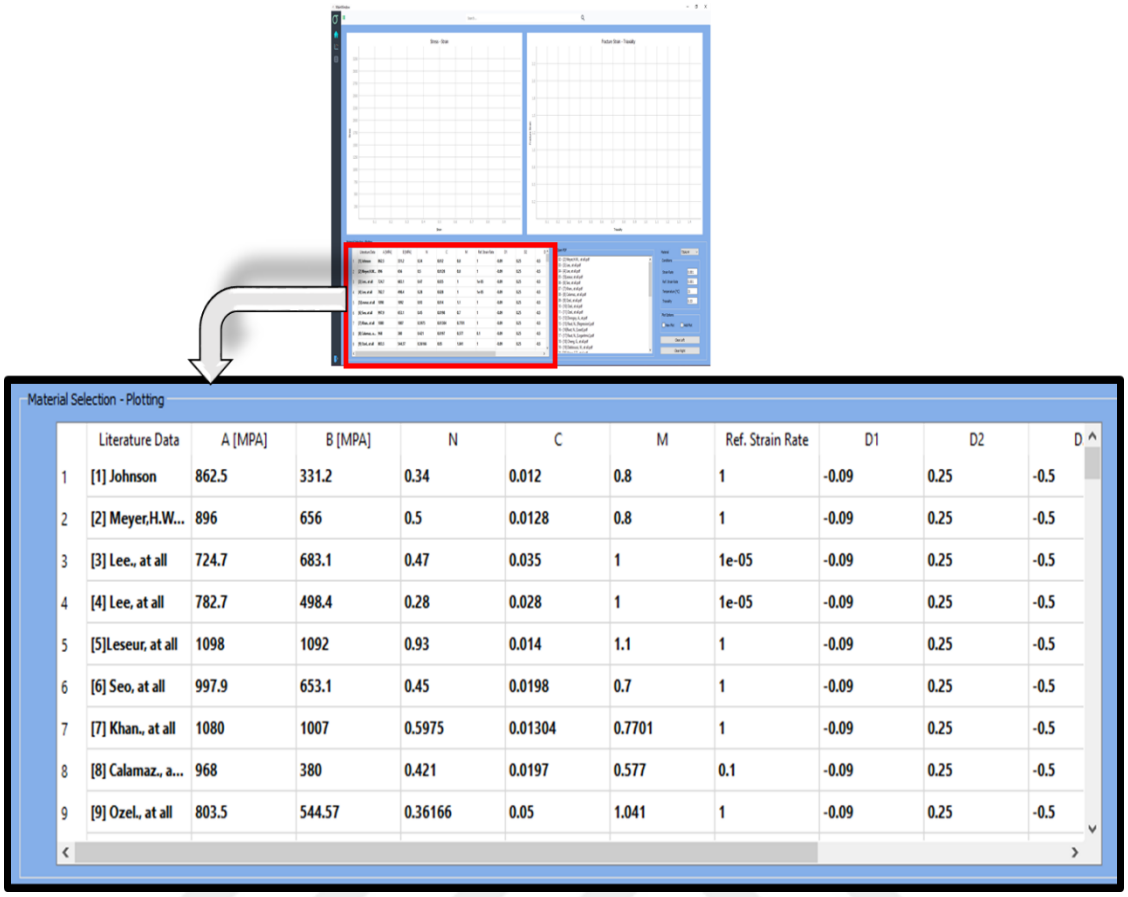

	Literature Data	A [MPA]	B [MPA]	N	C	M	Ref. Strain Rate	D1	D2	D
1	[1] Johnson	862.5	331.2	0.34	0.012	0.8	1	-0.09	0.25	-0.5
2	[2] Meyer,H.W...	896	656	0.5	0.0128	0.8	1	-0.09	0.25	-0.5
3	[3] Lee., at all	724.7	683.1	0.47	0.035	1	1e-05	-0.09	0.25	-0.5
4	[4] Lee, at all	782.7	498.4	0.28	0.028	1	1e-05	-0.09	0.25	-0.5
5	[5]Leseur, at all	1098	1092	0.93	0.014	1.1	1	-0.09	0.25	-0.5
6	[6] Seo, at all	997.9	653.1	0.45	0.0198	0.7	1	-0.09	0.25	-0.5
7	[7] Khan., at all	1080	1007	0.5975	0.01304	0.7701	1	-0.09	0.25	-0.5
8	[8] Calamaz., a...	968	380	0.421	0.0197	0.577	0.1	-0.09	0.25	-0.5
9	[9] Ozel., at all	803.5	544.57	0.36166	0.05	1.041	1	-0.09	0.25	-0.5

Figure 4.9. Literature data table of JC strength and damage parameters

On the right side of the table, as shown in Figure 4.10, is a vertical list of checkboxes labeled 'Open PDF'; This user's PDF files are listed, each of which is linked to the literature data sources referenced in the table. This feature offers an integrated library where users can access the full text of studies for detailed information. The PDF links provided in the interface suggest that users can access detailed documentation or research papers related to the data or models, supporting the academic and research-oriented utility of the tool. The inclusion of these PDF links is particularly beneficial for researchers and engineers who need to validate their data against existing studies or delve deeper into specific methodologies used in the referenced literature. By providing direct access to these documents, the interface ensures that users can quickly verify the accuracy and relevance of the data, compare methodologies, and understand the context of the findings within the broader scientific literature. This capability is especially useful when referencing multiple sources to ensure consistency and reliability in the data being used for analysis.

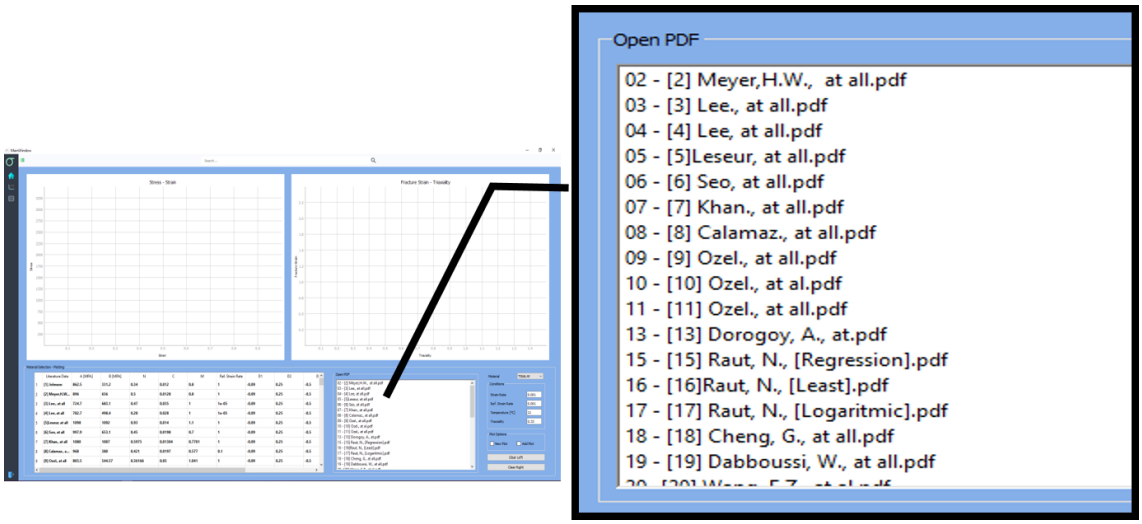

Figure 4.10. Listing of PDF files linked to literature data sources referenced in the table

In the bottom right area, as shown in Figure 4.11, there is a drop-down menu labeled 'Material' to select a material; The material "Ti6Al4V" was chosen as an example here. The "Conditions" tag below the material selection provides a comprehensive set of controls for determining material properties and conditions for the simulation. These include 'Strain Rate', 'Reference Strain Rate', 'Temperature [°C]' and 'Triaxiality', which are key parameters in JC models. These parameters provide a default and customizable analysis tool, allowing the user to determine under what conditions the data should be plotted. Below these fields, it provides clearing data graphs such as 'Clear Left' and 'Clear Right', which provide interactive elements to control the visualized data.

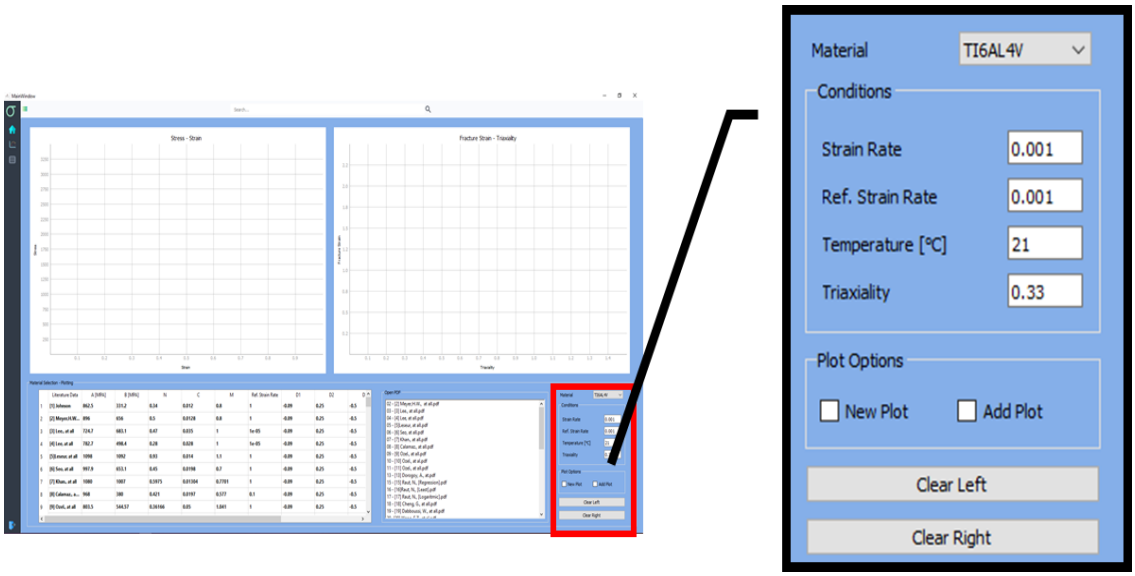

Figure 4.11. Control set of JC equation parameters

As a result, the Python-based application's interface provides an advanced platform for simulating material behavior using JC strength and damage models. The GUI allows detailed examination and visualization of material responses to complex loading conditions, which is essential for designing materials for specific applications and understanding failure mechanisms in existing materials. In general, the user interface is structured to facilitate the selection, analysis, and visualization of material properties data, to provide researchers with a tool to evaluate material behavior under various conditions, and to assist in the material selection process for specific applications. The design reflects an academic and practical approach that combines data management with graphical analysis in a single interface. The interface also includes software that allows direct comparisons between experimental data and literature studies.

The working logic of this interface, designed in Python programming language for JC material models, begins with the initialization of a graphical drawing area designed to display stress-strain relationships within the code, GUI. Following this, a 'GraphicsLayoutWidget' from the 'pyqtgraph' library is instantiated. This widget serves as a container for plot items, facilitating the creation and layout of graphs. A plot item is then created and added to the graphics layout widget. Similar steps are followed to initialize a second plot area dedicated to displaying the relationship between fracture strain and triaxiality. Then, it loads an Excel workbook using the 'openpyxl' library, which allows for reading and writing Excel files in Python. The code specifies a list of sheet names, representing different materials, to be added to a 'ComboBox'. This ComboBox serves as a user interface element that enables users to select a material, thereby dictating the data to be displayed within the application. By changing the selection in the ComboBox, the table is updated according to the selected material. This feature allows users to select different materials and view their corresponding data visualizations.

The user's selection of material from the ComboBox launches the Excel work mode of that sheet. Upon successful sheet selection, the function proceeds to extract and display data from the Excel sheet. It iterates over specified rows and columns within the sheet, translating the Excel cells' contents into items within a PyQt table widget. Upon validation, the method proceeds to populate a table widget with material parameters such as Literature Data, A [MPa], B [MPa], N Parameter, C Parameter, M Parameter, Reference Strain Rate Parameter, D_1 to D_5 Parameters, and additional material properties. Before the data population, the contents of the table widget are cleared, setting the stage

for an updated display. Defines the folder containing PDF files related to the selected material, and a model for a ListView is created and populated with the titles of the PDF files; This model allows the user to open and view the PDF file of the corresponding work directly from the application by double-clicking on the ListView.

When the user clicks on the study data that the user wants to draw from the literature studies listed in the table widget, the program calculates the stress values for certain strain values using the JC material parameters in this line. A similar process is performed for the JC damage equation case. Finally, the obtained data is plotted on the graph. Users change the 'Conditions' parameters in the bottom right area of the interface and the table widget, and the data obtained as a result of the changed parameters is processed in the graphics area when they click on the relevant working line in the first column of the table widget.

CHAPTER 5

RESULTS AND DISCUSSION

Chapter 5 shows all the results, experimental results and program results in the thesis.

5.1. Experimental Results of Quasi-static and Dynamic Tests

The force-displacement curves of the quasi-static tensile samples of 316L and AISI 4340 at $1x10^{-3}$, $1x10^{-2}$, and $1x10^{-1}$ s^{-1}, and the dynamic tensile (SHTB) test of 316L test at 1500 s^{-1} and AISI 4340 at 1622 s^{-1} are shown in Figure 5.1(a) and (b), respectively. Since three tests were performed at each strain rate showing the similar force-displacement curves at each strain rate, representative a single force-displacement curve is plotted in the same figure at each strain rate. The corresponding engineering stress-engineering strain curves are shown in Figure 5.2(a) for 316L and Figure 5.2(b) for AISI 4340. The true stress-true strain curves of the same 316L and AISI 4340 alloys at different strain rates are shown in Figure 5.3(a-b), respectively. The true stress-true plastic strain curves of 316L and AISI 4340 alloy at different strain rates are further shown in Figure 5.4(a) and (b), respectively.

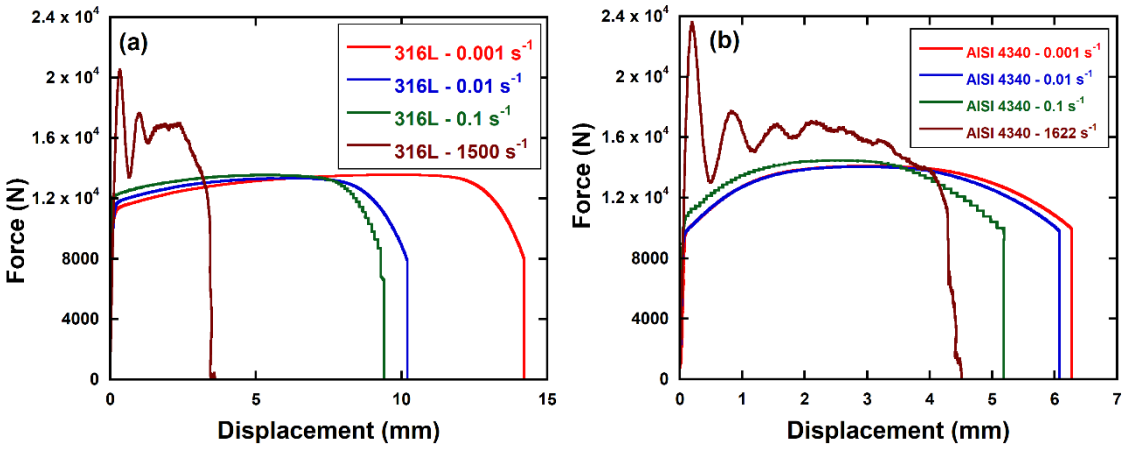

Figure 5.1. The force-displacement curves of (a) 316L and (b) AISI 4340 at different strain rates

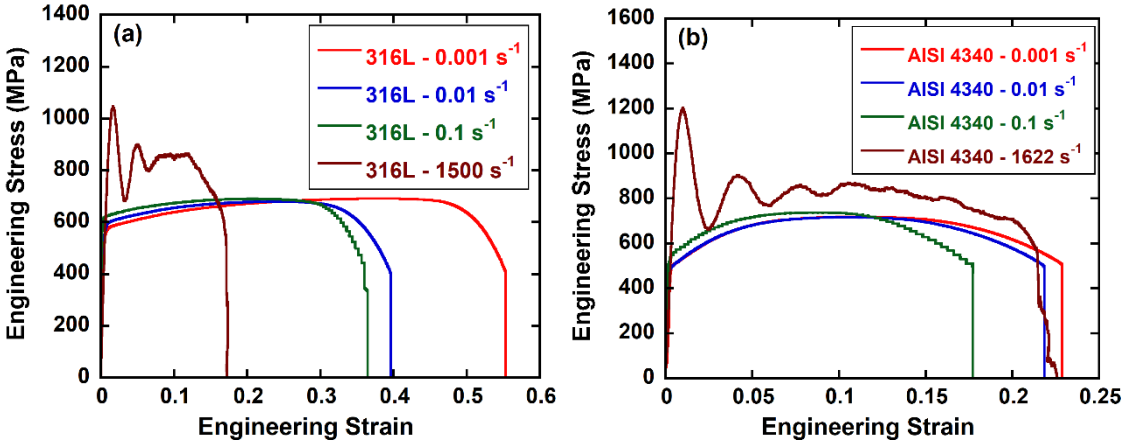

Figure 5.2. The engineering stress-strain curves of (a) 316L and (b) AISI 4340 alloy at different strain rates

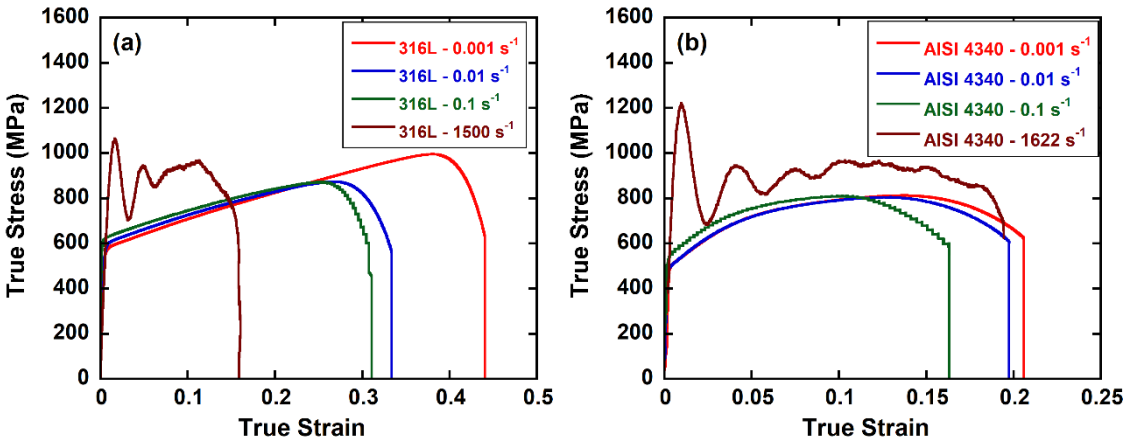

Figure 5.3. The true stress-true strain curves of (a) 316L and (b) AISI 4340 alloy at different strain rates

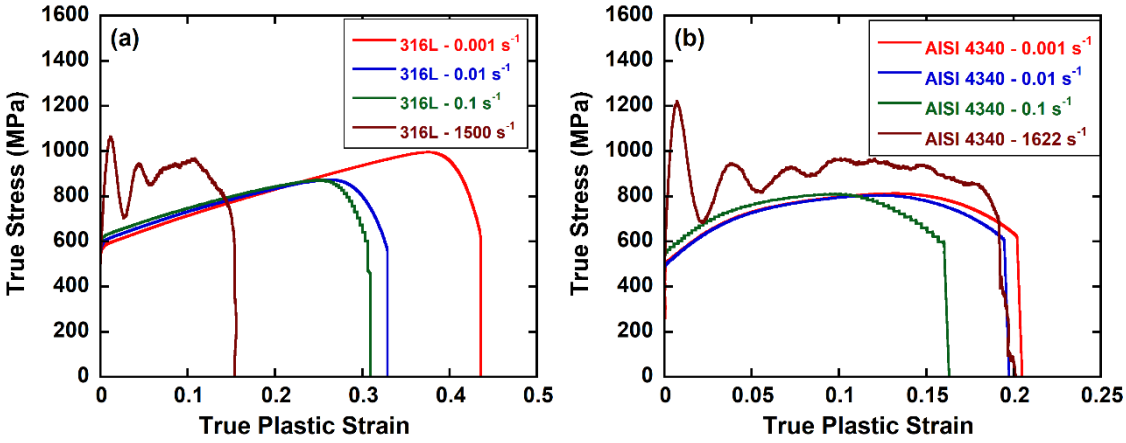

Figure 5.4. True stress-true plastic strain curves of (a) 316L and (b) AISI 4340 at different strain rates

The average yield strengths of 316L are 580, 580, 600 and 801.11 MPa, and the average ultimate tensile strengths are 995, 873, 870 and 1045 MPa sequentially at $1x10^{-3}$, $1x10^{-2}$, $1x10^{-1}$ and 1500 s^{-1}. The average engineering fracture strains of 316L are 0.38, 0.271, 0.255 and 0.155 at $1x10^{-3}$, $1x10^{-2}$, $1x10^{-1}$ and 1500 s^{-1}, respectively. The average yield strengths of AISI 4340 are 460, 459.86, 549.21 and 774.84 MPa, and the ultimate tensile strengths are 813, 804, 810 and 1221 MPa sequentially at $1x10^{-3}$, $1x10^{-2}$, $1x10^{-1}$ and 1622 s^{-1}. The engineering failure strains are 0.205, 0.195, 0.163 and 0.197 at $1x10^{-3}$, $1x10^{-2}$, $1x10^{-1}$ and 1622 s^{-1}, respectively.

Figure 5.5(a) shows the true stress-true plastic strain curves of three test samples of 316L at the reference strain rate of $1x10^{-3}$ s^{-1}. The first bracket parameters (*A, B and n*) of the JC flow stress equation are determined by direct curve fitting the equation to the stress-strain data. The parameter *A* in the equation represents the yield stress and this value is 580 MPa at $1x10^{-3}$ s^{-1}. The curve fitting method was applied to the region data starting from the beginning of the elastoplastic region until the final strength point. As a result of this curve fitting, *B* and *n* values at $1x10^{-3}$ s^{-1} are determined 1025.77 MPa and 0.86727, respectively. The fitting results of the values of *A*, *B* and *n* at $1x10^{-2}$ s^{-1} are shown in Figure 5.5(b). The *A*, *B* and *n* values at $1x10^{-2}$ s^{-1} are 580 MPa, 844.79 and 0.7703, respectively. The values of *A*, *B* and *n* at $1x10^{-1}$ s^{-1}, as shown in Figure 5.5(c), are 600 MPa, 680.88 and 0.6279, respectively. The same values are sequentially 801.11 MPa, 388.32 and 0.39369 at 1500 s^{-1} as shown in Figure 5.5(d).

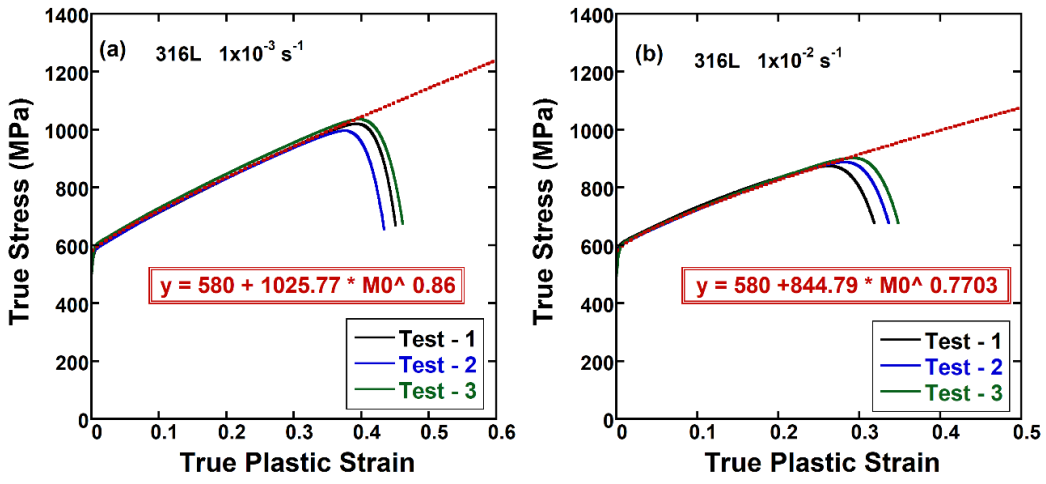

(cont. on next page)

Figure 5.5. The JC *A*, *B* and *n* parameters of 316L at (a) $1x10^{-3}$, (b) $1x10^{-2}$, (c) $1x10^{-1}$ s^{-1}, and (d) 1500 s^{-1}

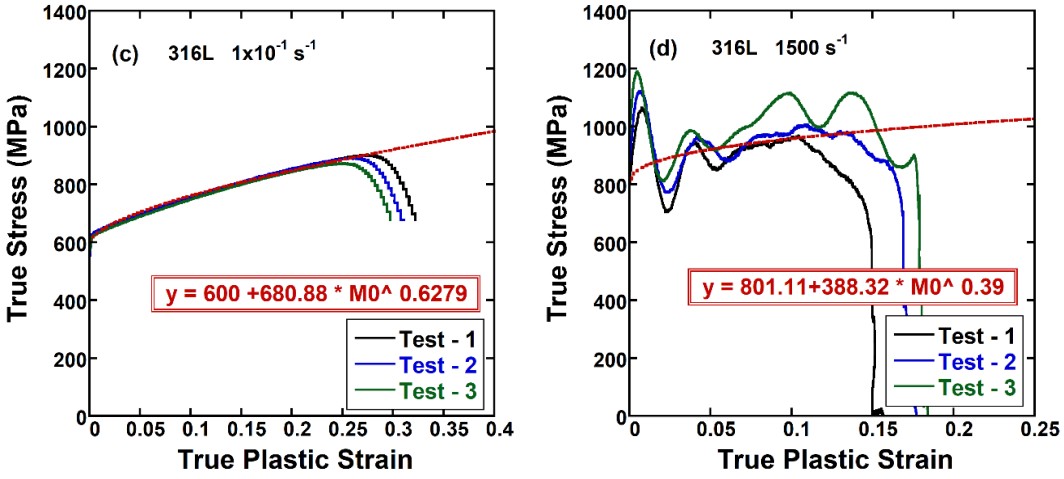

Figure 5.5 (cont.)

Figure 5.6 shows the true stress-true plastic strain curves of three test samples of AISI 4340 material the first bracket parameters of the JC strength model to these curves, the determination of *A*, *B and n* values. Figure 5.6(a) shows the true stress-true plastic strain curves of three tests of AISI 4340 alloy at $1x10^{-3}$ s^{-1}. The values of *A*, *B* and *n* at $1x10^{-3}$ $s^{-1}$are 460 MPa, 815 and 0.38, respectively. The determined values *A*, *B* and *n* at $1x10^{-2}$ s^{-1} (Figure 5.6(b)) are 475.84 MPa, 960.28 and 0.45121, respectively. At $1x10^{-1}$ s^{-1}, the values *A*, *B* and *n* are 549.21 MPa, 993 and 0.53114, respectively, as shown in Figure 5.5 (c). The values of *A*, *B* and *n* determined by curve fitting at 1622 s^{-1} are 774.74 MPa, 368.11 and 0.38045, respectively (Figure 5.6(d)).

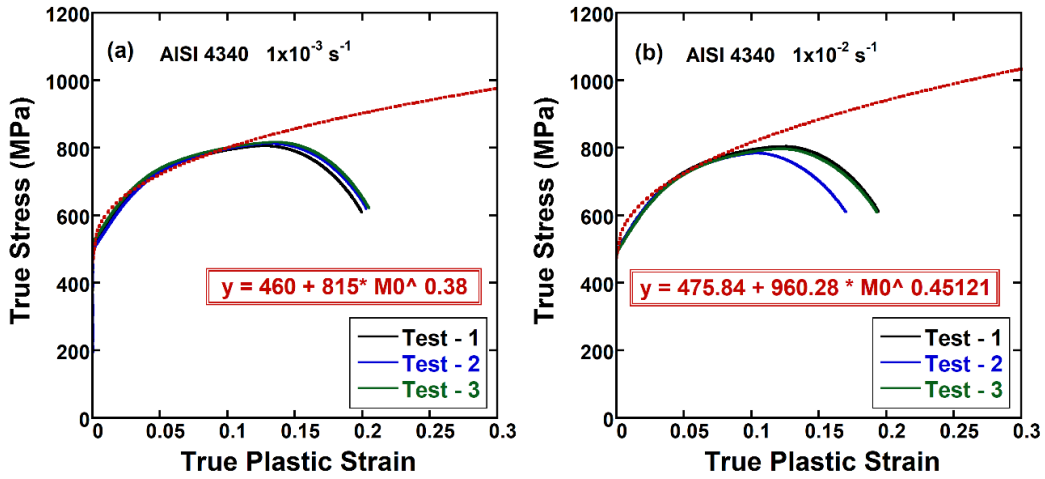

(cont. on next page)

Figure 5.6. The JC *A*, *B* and *n* parameters of AISI 4340 material at (a) $1x10^{-3}$, (b) $1x10^{-2}$, (c) $1x10^{-1}$ s^{-1}, and (d) 1622 s^{-1}.

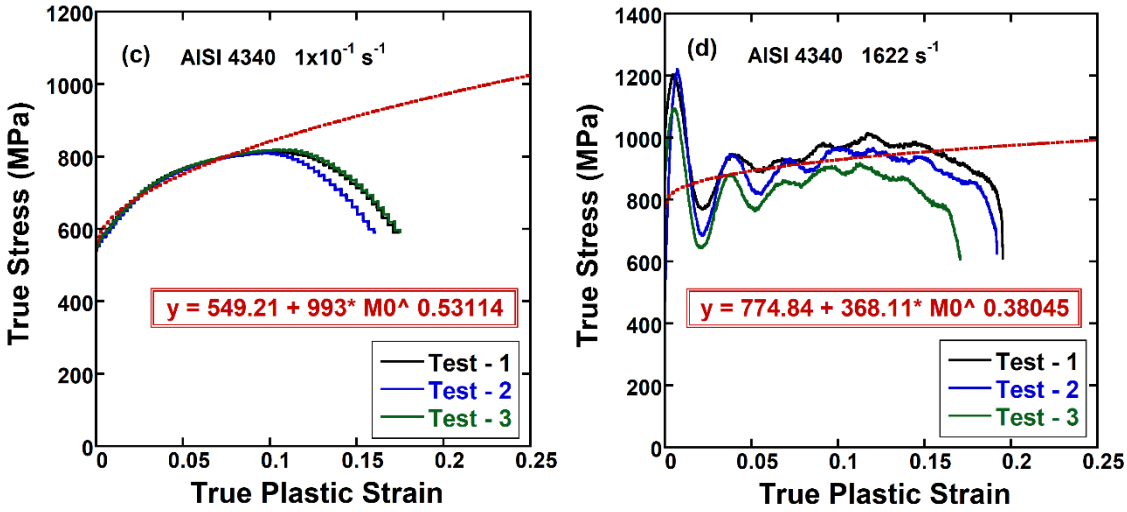

Figure 5.6 (cont.)

The JC *C* parameter is determined by curve fitting the true stress of 316L and AISI 4340, sequentially at 0.1 and 0.05 strain, with $\sigma_0(1 + C ln\left(\frac{\dot{\varepsilon}}{\dot{\varepsilon_0}}\right))$, where $\dot{\varepsilon_0}$ is the reference strain rate, $1x10^{-3}$ s^{-1}. As a result of the curve fitting, the *C* value of 316L is calculated 0.019491 (Figure 5.7(a)), and the *c* value of AISI 4340 is 0.01315 (Figure 5.7(b)). Figure 5.8(a) and (b) show the true stress-true plastic strain curves of 316L and AISI 4340 with the determined *A*, *B* and *n* values at different strain rates, respectively. As noted in the same figures, the adiabatic heating of the specimens at increasing strain rates reduces the flow stresses; hence, at larger strains, high strain rate flow stresses become lower than those of lower strain rate tests. The true stress-true plastic strain curves of 316L and AISI 4340 were then calculated using the determined JC parameters using the JC flow stress equation (including the *C* parameter) and by taking $1x10^{-3}$ s^{-1} as the reference strain rate. Figure 5.9(a) and (b) show the calculated JC curves of 316L and AISI 4340 at four different strain rates, respectively. As the *C* values are determined at a low strain (0.1 and 0.05), the adiabatic heating effect is eliminated. In these curves, the parameter A is taken 580 MPa for 316L and 460 MPa for AISI 4340 at the reference strain rate of $1x10^{-3}$ s^{-1}. The values of *B* and *n* are sequentially 1025.77 MPa and 0.86727 for 316L and 815 MPa and 0.38 for AISI 4340 at the reference strain rate. The values of *C* are taken 0.019491 for 316L and 0.01315 for AISI 4340. The true stress-true plastic strain curves determined by using the JC flow stress equation and the experimental true stress-true plastic strain curves are shown in Figure 5.10 (a) and (b), sequentially for 316L and AISI 4340 for comparison.

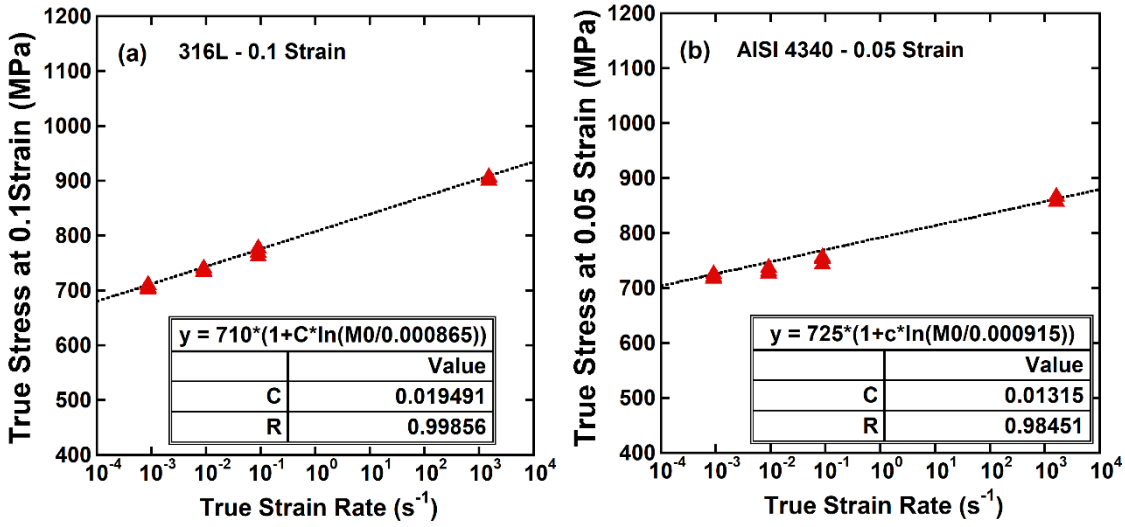

Figure 5.7. The JC *C* parameter of (a) 316L, and (b) AISI 4340

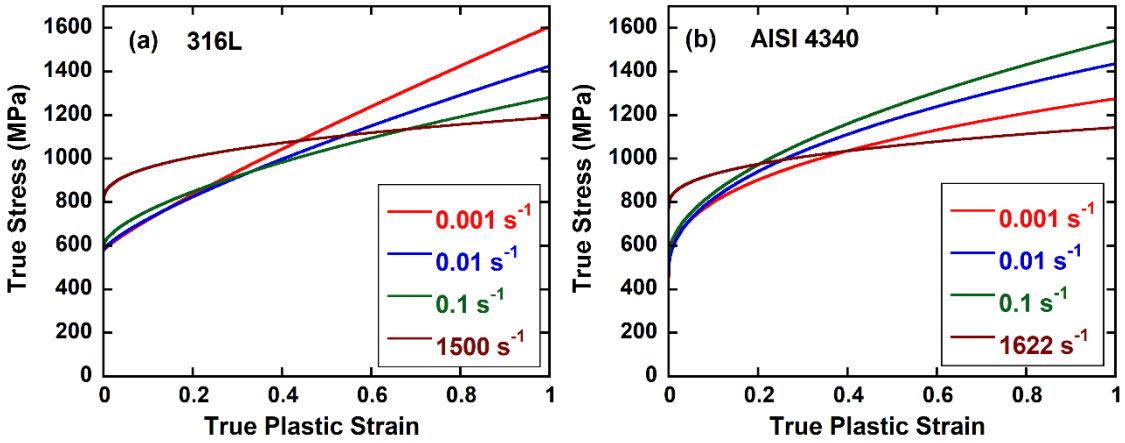

Figure 5.8. The true stress-true plastic strain curves of (a) 316L and (b) AISI 4340 with the determined *A*, *B* and *n* values at four different strain rates

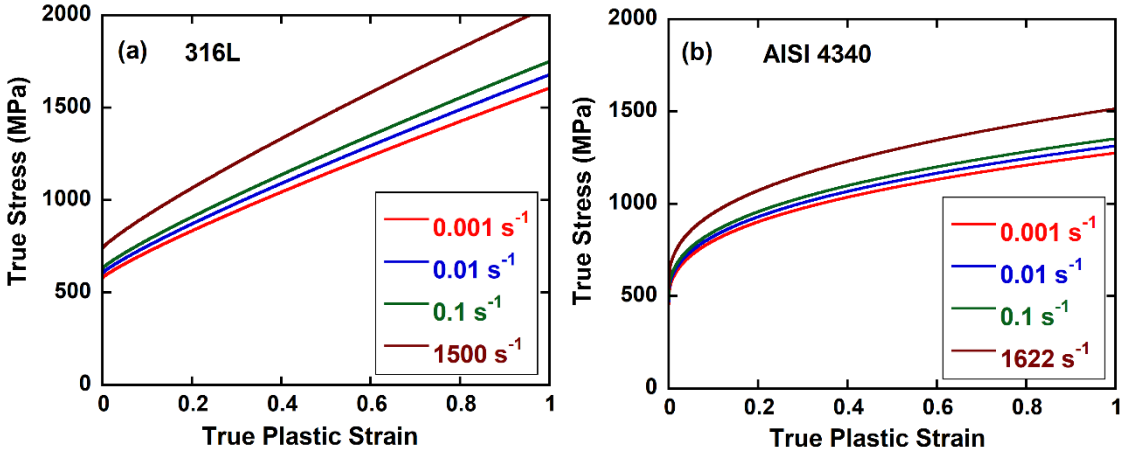

Figure 5.9. The JC true stress-true plastic strain curves of (a) 316L and (b) AISI 4340

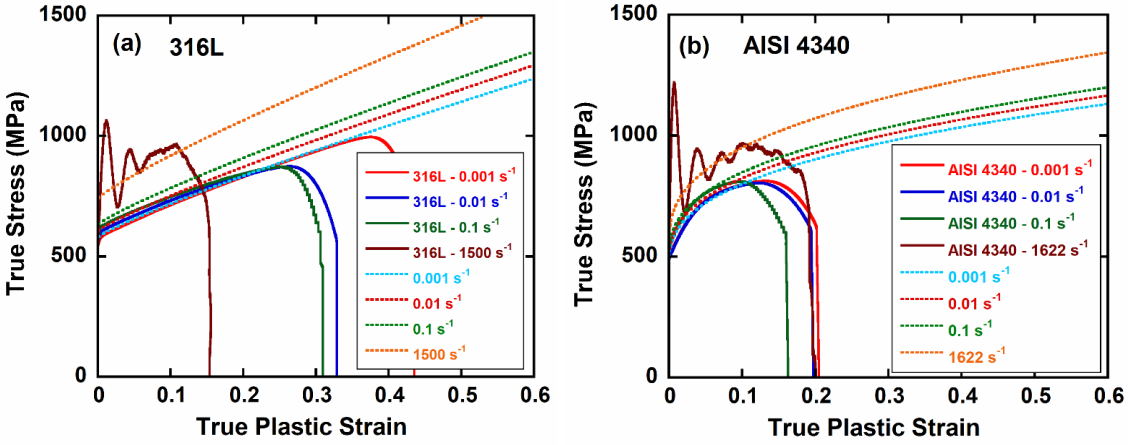

Figure 5.10. The true stress-true plastic strain curves determined by using the JC flow stress equation and the experimental true stress-true plastic strain curves (a) 316L, and (b) AISI 4340

Figure 5.11(a) and (b) show sequentially the equivalent stress-strain curves of 316L and AISI 4340 determined by the MLR method. The necking strains of 316L, used in the MLR equation, are 0.38, 0.271, 0.255 and 0.155 at $1x10^{-3}$, $1x10^{-2}$, $1x10^{-1}$ s^{-1} and 1500 s^{-1}, respectively. The necking strains of AISI 4340 are 0.138, 0.123, 0.113 and 0.119 at $1x10^{-3}$, $1x10^{-2}$, $1x10^{-1}$ s^{-1} and 1622 s^{-1}, respectively. The values of *A, B and n* parameters of the JC strength model at $1x10^{-3}$ s^{-1} are determined by fitting the equivalent stress-strain curves determined by the MLR method to the JC flow stress equation.

Figure 5.12(a) and (b) show the fitting results for 316L and AISI 4340, respectively. The determination of the *c* parameter is made by curve fitting. The equivalent stress-equivalent strain curves at four different strain rates are drawn according to the relevant actual strain rate of stress values at 0.1 strain (for 316L), and 0.05 strain (for AISI 4340). The curve fitting equation $\sigma_0(1 + Cln\left(\frac{\dot{\varepsilon}}{\dot{\varepsilon}_0}\right))$ is assigned to the stress JC equation at a reference strain rate of $1x10^{-3}$ s^{-1}. As a result of the curve fitting, the *C* value is found 0.020986 for 316L and 0.015983 for AISI 4340, as shown sequentially in Figure 5.13(a) and (b). The JC equivalent stress-plastic strain curves of 316L and AISI 4340 at four different strains using the MLR method are shown in Figure 5.14(a) and (b), respectively. The values of *A*, *B* and *n* in Figure 14(a) are 580 MPa, 876.1 MPa and 0.72687, respectively. The values of *A*, *B* and *n* in Figure 14(b) are 460 MPa, 645.2 MPa and 0.25343, respectively.

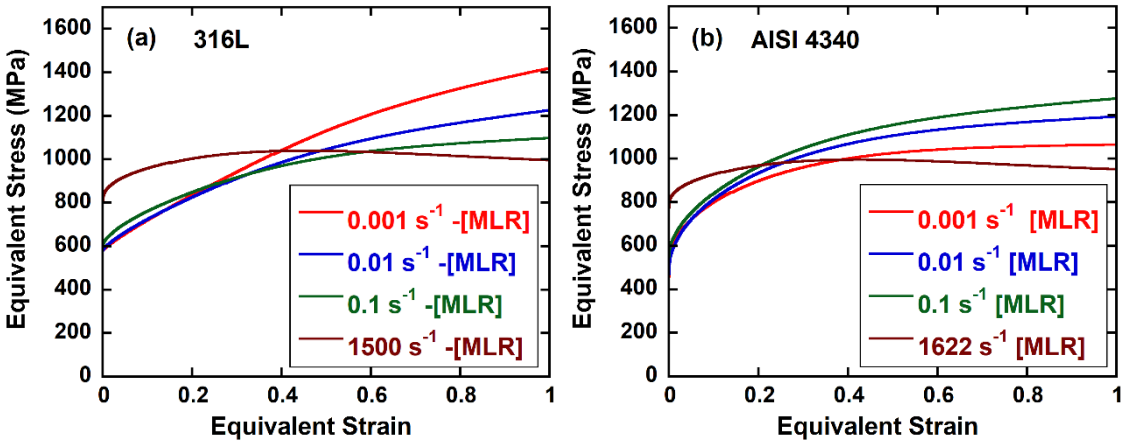

Figure 5.11. The equivalent stress-strain curves determined by the MLR method for (a) 316L and (b) AISI 4340 at different strain rates

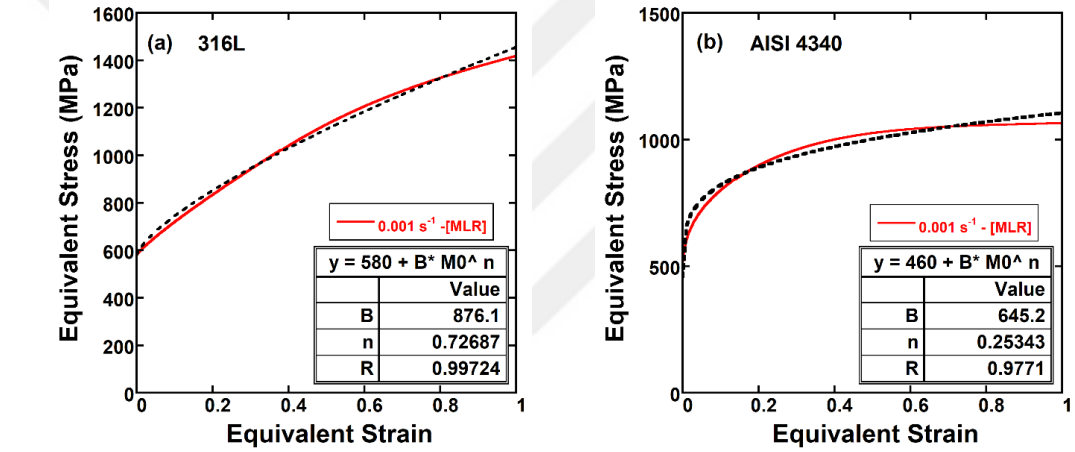

Figure 5.12. The values of *A, B and n* using the MLR method at $1x10^{-3}$ s^{-1} (a) 316L, and (b) AISI 4340

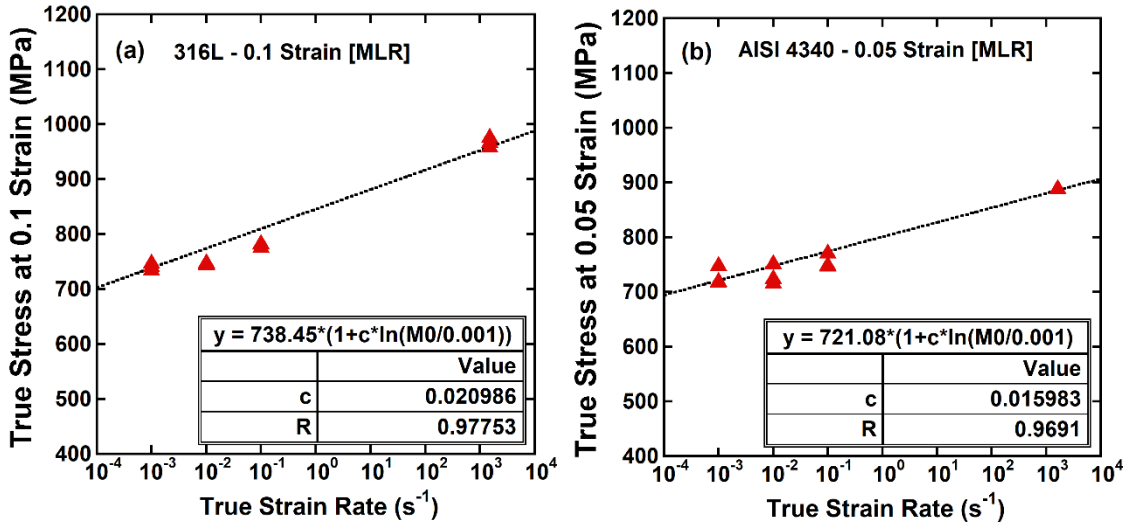

Figure 5.13. The values of *C* parameter in the MLR method (a)316L and (b) AISI 4340

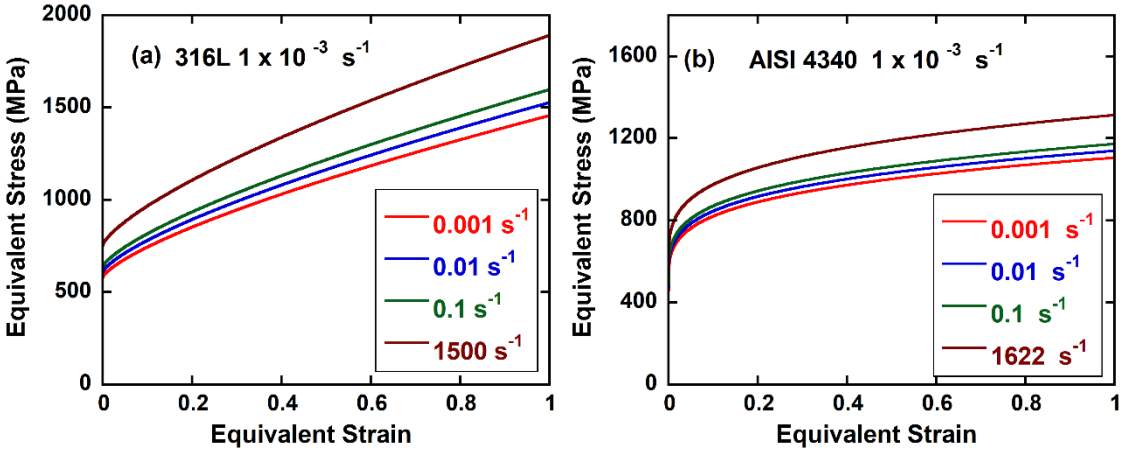

Figure 5.14. The equivalent stress-strain curves of (a) 316L and (b) AISI 4340 using the MLR method

The true stress-true plastic strain curves determined by using the JC flow stress equation and MLR method the experimental true stress-true plastic strain curves are shown in Figure 5.15 (a) and (b), sequentially for 316L and AISI 4340 for comparison. The experimental stress curves are predicted well by the MLR method for both alloys at $1x10^{-3}$ s^{-1} and the SHTB strain rate. Some discrepancies between the predictions and experiments are seen on the other hand at higher quasi-static strain rates.

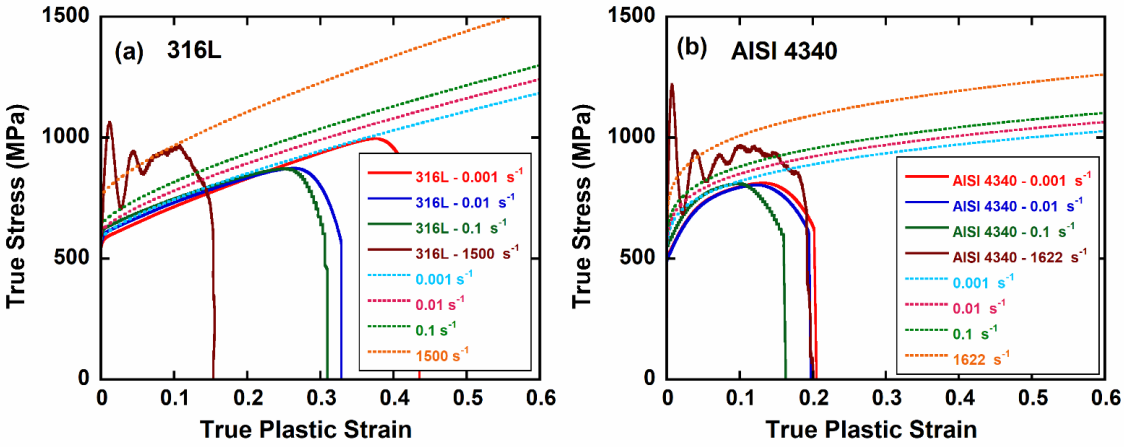

Figure 5.15. The true stress-true plastic strain curves determined by the MLR method and the experimental true stress-true plastic strain curves (a) 316L and (b) AISI 4340

The deformation of the quasi-static tensile tests samples was video-recorded and the snapshots were taken at equal intervals from these videos. The diameter and radius of

the sample and necking area of each of the images were performed in ImageJ program. Figure 5.16(a) shows the average stress-strain curve of 316L (determined from the video record) and fitted *A*, *B* and *n* values, and Figure 5.16(b) and (c) show the Bridgman and MLR corrected equivalent stresses and fitted *A*, *B* and *n* values. Figure 5.17(a) shows the average stress-strain curve of AISI 4340 (determined from the video record) and fitted *A*, *B* and *n* values, and Figure 5.17(b) and (c) show the Bridgman and MLR corrected equivalent stresses and fitted *A*, *B* and *n* values. In both metals, the corrected values of *B* and *n* are reduces as compared to the average stress-strain curves.

In Figure 5.18(a) and (b) three curves at $1x10^{-3}$ s^{-1}: average stress-strain and the Bridgman and MLR corrected stress-strain curves are shown together for 316L and AISI 4340, respectively. The average true stress, Bridgman equivalent stress and MLR equivalent strain values for *1000* points with strain values between *0* and *1* of *A, B and n* values determined by manual measurements made on the test video for both materials are presented together.

Figure 5.19(a-c) and Figure 20(a-c) show the average stress-strain and the Bridgman and MLR corrected stress-strain curves at different strain rates for 316L and AISI 4340, respectively. In Figure 5.21 (a-c) and Figure 22(b), the average stress-strain and the Bridgman and MLR corrected stress-strain curves are shown together with the experimental stress-strain curves, sequentially for 316L and AISI 4340.

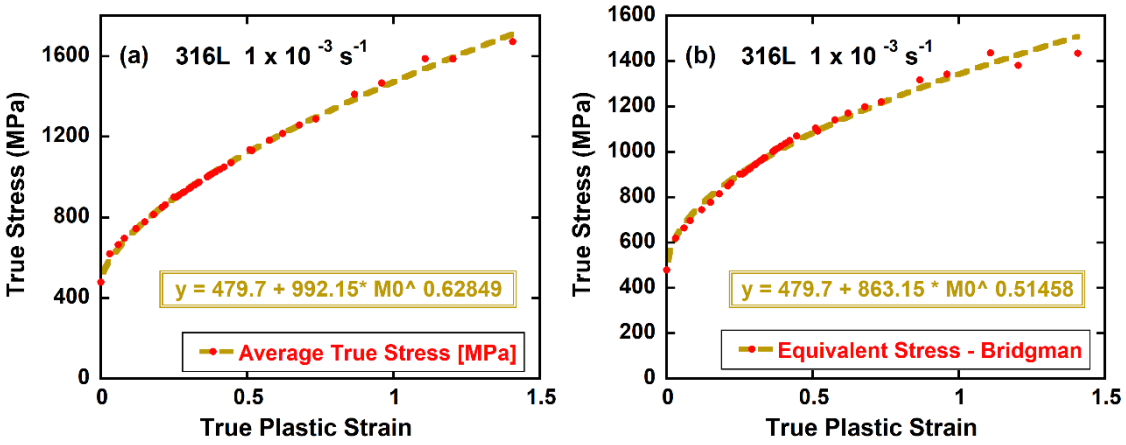

(cont. on next page)

Figure 5.16. (a) The average true stress-strain and (b) Bridgman and (c) MLR corrected equivalent stress-strain curves of 316L at $1x10^{-3}$ s^{-1}

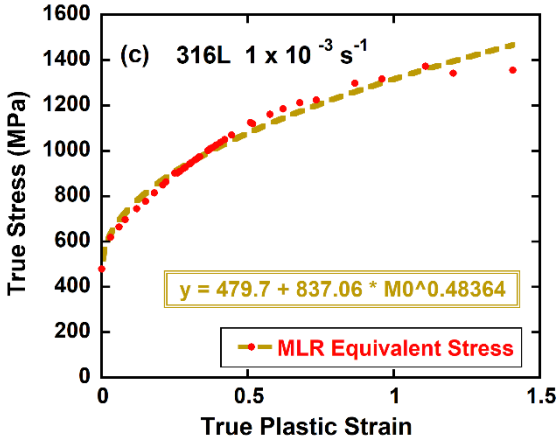

Figure 5.16 (cont.)

In Figure 5.17, the graphs respectively depict the determination of the average stress and equivalent stress curves of AISI 4340 material at a strain rate of $1x10^{-3}$ s^{-1} from the test video. The determination of *A, B, and n* values is demonstrated using a direct curve-fitting method on the measured stress data points. For each curve determined at a strain rate of $1x10^{-3}$ s^{-1}, the parameter *A* is *549.99* MPa. Firstly, for the average true stress-true plastic strain curve obtained from the measurement points, the curve-fitting method yielded *B* and *n* values of *650.68* and *0.47396*, respectively, at a strain rate of $1x10^{-3}$ s^{-1}. For the equivalent stress curve determined by the Bridgman method, the *B* and *n* parameters were found to be *437.46* and *0.31476*, respectively. The equivalent stress parameters determined by the MLR method were obtained as *537.23* and *0.37032*.

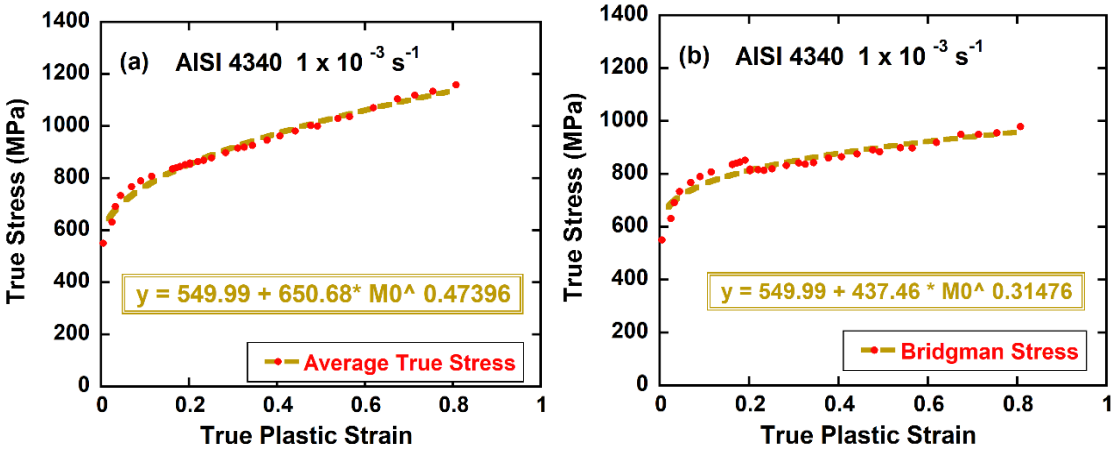

(cont. on next page)

Figure 5.17. (a) The average true stress-strain and (b) Bridgman and (c) MLR corrected equivalent stress-strain curves of AISI 4340 at $1x10^{-3}$ s^{-1}

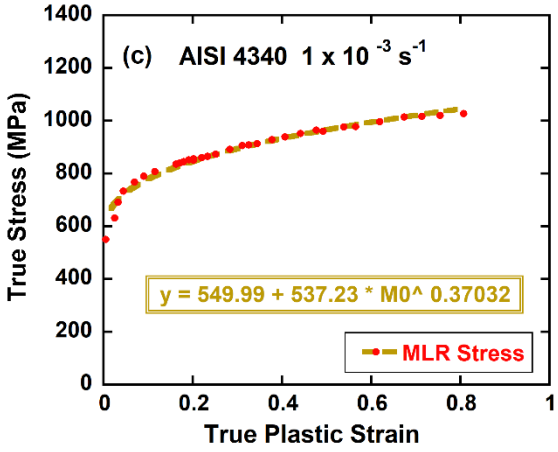

Figure 5.17 (cont.)

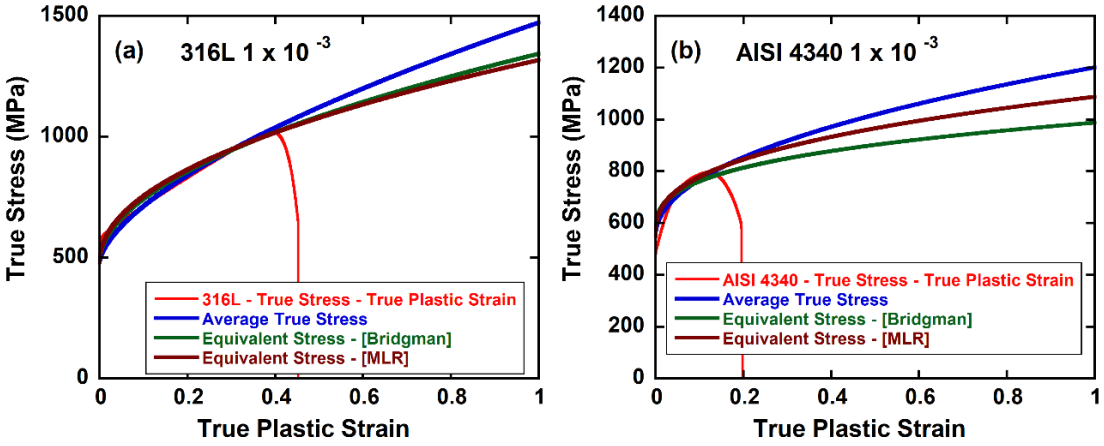

Figure 5.18. The average stress-strain and Bridgman and MLR corrected stress-strain curves of (a) 316L and (b) AISI 4340 at $1x10^{-3}$ s^{-1}

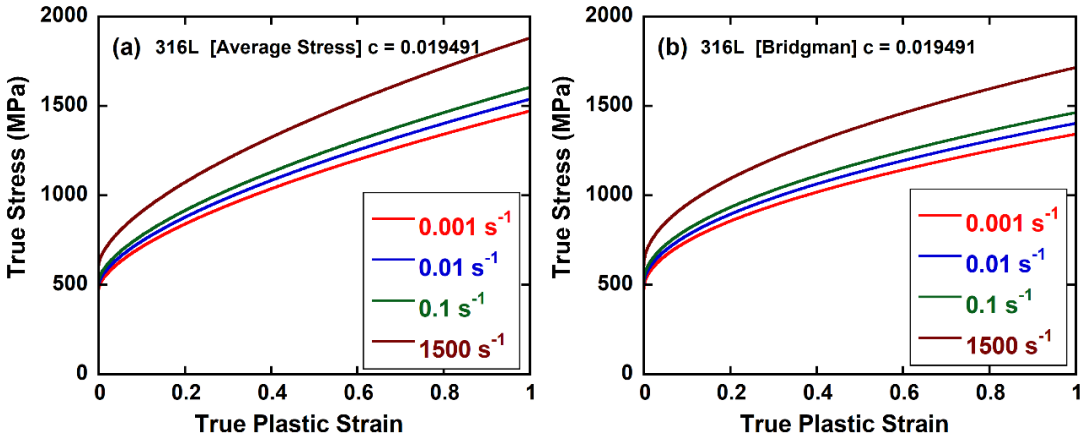

(cont. on next page)

Figure 5.19. The stress-strain curves of 316L at different strain rates: (a) the average and (b) Bridgman and (c) MLR corrected stress-strain curves

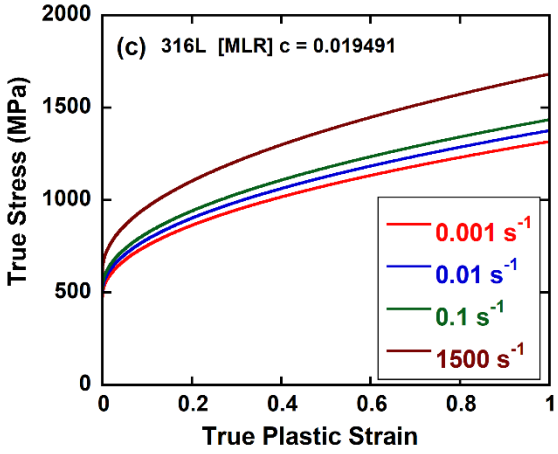

Figure 5.19 (cont.)

In Figures 5.19 and 5.20, the Johnson-Cook (JC) strength model is shown using to analyze the behavior of 316L and AISI 4340 materials, respectively, at different strain rates. For 316L (Figure 5.19), the *A, B, and n* parameters were determined at a reference strain rate of $1x10^{-3}$ s^{-1}, and the *C* parameter of the strain rate effect equation was found to be *0.019491*. This parameterization allows the JC model to predict the material's response accurately across varying strain rates. Similarly, for AISI 4340 (Figure 5.20), *A, B, and n* were established at the same reference strain rate, with a *C* parameter of *0.01315* derived from experimental data.

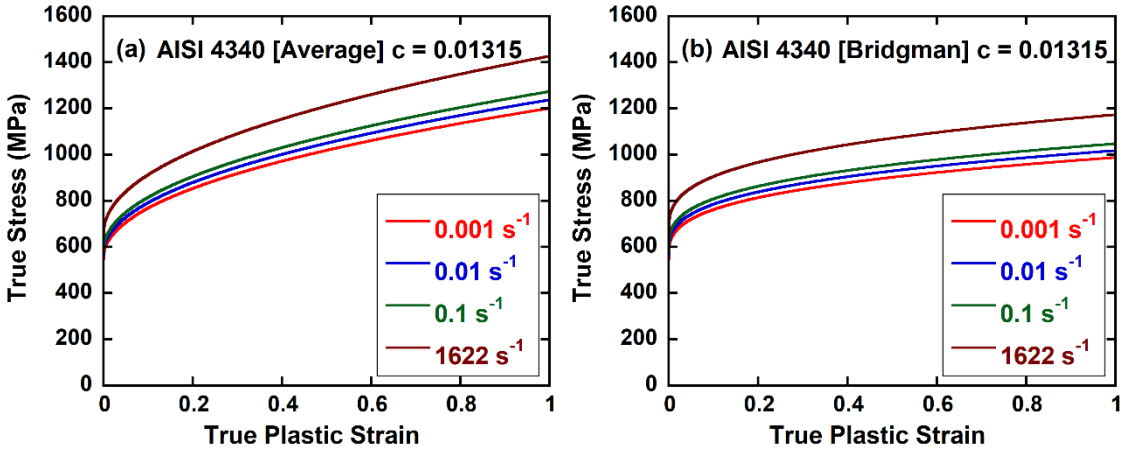

(cont. on next page)

Figure 5.20. The stress-strain curves of AISI 4340 at different strain rates: (a) the average and (b) Bridgman and (c) MLR corrected stress-strain curves

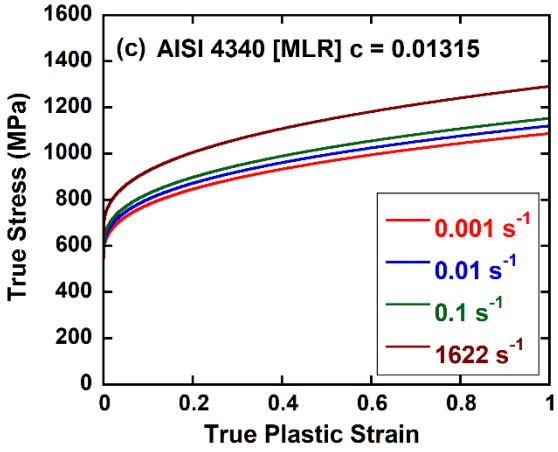

Figure 5.20 (cont.)

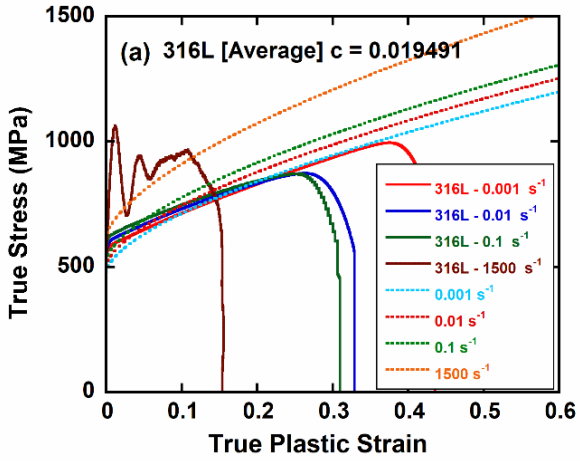

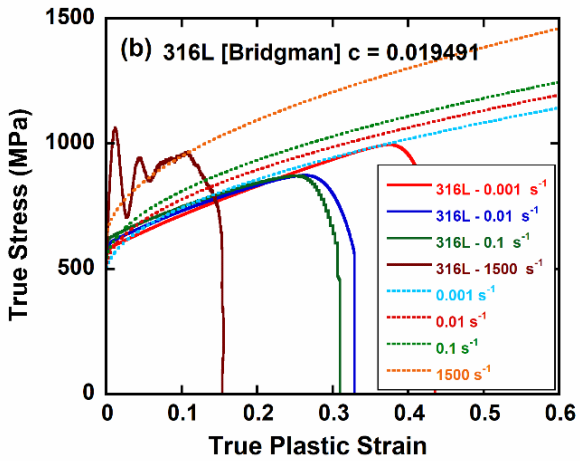

(cont. on next page)

Figure 5.21. The predicted and experimental stress-strain curves of 316L at different strain rates: (a) the average and (b) Bridgman and (c) MLR corrected stress-strain curves

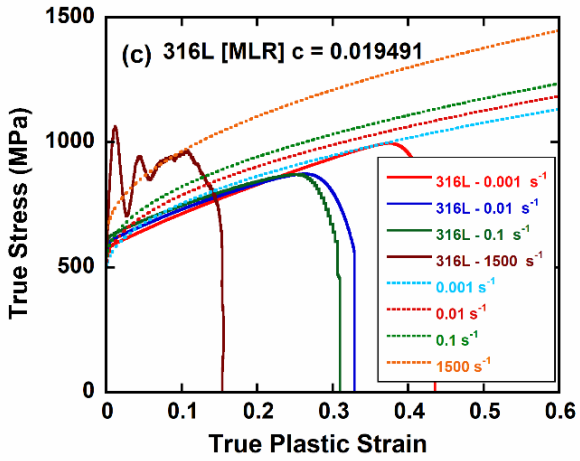

Figure 5.21 (cont.)

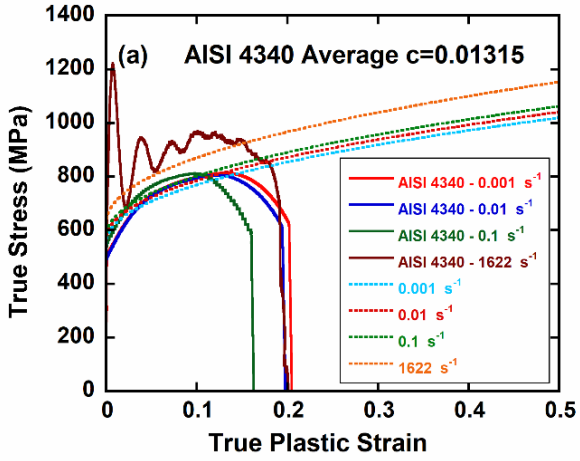

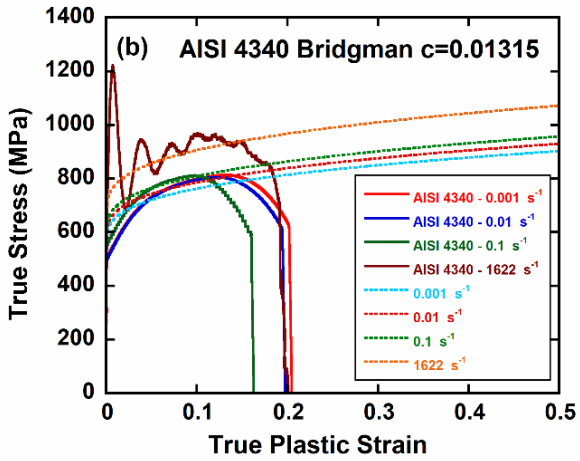

(cont. on next page)

Figure 5.22. The predicted and experimental stress-strain curves of AISI 4340 at different strain rates: (a) the average and (b) Bridgman and (c) MLR corrected stress-strain curves

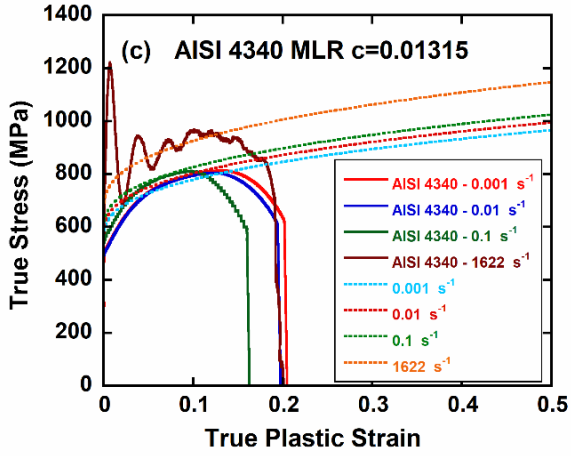

Figure 5.22 (cont.)

Figures 5.23(a-h) show the experimental calculation results of the equivalent fracture plastic strains of 316L and AISI 4340 materials using the JC failure model equation. Parameters D_1, D_2, D_3, D_4 are determined from the JC failure equation constants. Three tests were performed at *4* different stress triaxialities values: *0.33, 0.6, 0.9 and 1.2.* All tests were performed at a strain rate of $1x10^{-3}$ s^{-1}. Since all tests were carried out at room temperature, the temperature factor parameter D_5 was not calculated in the damage equation. Samples with different notch radius are used to determine the fracture strain. After tests were carried out under quasi-static and isothermal conditions and D_1, D_2 and D_3 values are determined by the fit method, the test data are used for the purpose of strain against fracture as a function of stress triaxiality. The damage equation parameters found for the 316L material are shown in Figure 5.23 (a-b). In Figure 5.1 (a), the value of -1.5 was assigned to the D_3 parameter and it was determined according to the fit equation of the D_1 and D_2 parameters. The values of D_1 and D_2 parameters determined according to the D_3 value of *-1.5 are 0.76 and 1.17*, respectively. The graph shown in Figure 5.23 (b) shows the results of parameter determination without assigning a value to D_3. According to the created fit equation, the values of D_1, D_2 and D_3 parameters are *0.99203, 2.1021 and -4.1939*, respectively. Quasi-static and dynamic tests of samples with a stress triaxiality value of *0.33* were used to determine the D_4 parameter included in the damage equation. The parameter D_4 was found by performing linear curve fitting on the fracture strain-strain rate curve drawn on a logarithmic basis. The D_4 damage parameter found by determining the D_3 value of the 316L material as *-1.5* is shown in Figure 5.23(c). D_4 parameter was obtained as -0.0394. In the graph of Figure 5.23(d), the value of the

determined D_4 parameter shows the determination of D_4 when no value is assigned to the D_3 value. Accordingly, the D_4 value was obtained as -0.041376. As a result of obtaining the D_4 parameter, the JC parameters of the 316L material were completed. Figure 5.23 (e-h) shows the graphs of determining the equivalent fracture plastic strains of the AISI 4340 material and the parameters D_1, D_2, D_3, D_4 from the JC failure equation constants. Figure 5.23(e) shows the determination of D_1 and D_2 parameters according to the fit equation by assigning a value of -1.5 to the D_3 parameter of the AISI 4340 material. When the D_3 value is *-1.5*, the values of the D_1 and D_2 parameters are *0.32* and *0.905*, respectively. The graph shown in Figure 5.23(f) shows the results of parameter determination without assigning a value to D_3. According to the created fit equation, the values of D_1, D_2 and D_3 parameters are *0.47, 1.21 and -3.176*, respectively. Quasi-static and dynamic tests of samples with a stress triaxiality value of *0.33* were used to determine the D_4 parameter included in the damage equation. The parameter D_4 was found by performing linear curve fitting on the fracture strain-strain rate curve drawn on a logarithmic basis. The D_4 damage parameter found by determining the D_3 value of the AISI 4340 material as *-1.5* is shown in Figure 5.23(g). D_4 parameter was obtained as -0.00036. In the graph of Figure 5.23(h), the value of the determined D_4 parameter shows the determination of D_4 when no value is assigned to the D_3 value. Accordingly, the D_4 value was obtained as -0.002533. As a result of obtaining the D_4 parameter, the JC parameters of the AISI 4340 material were completed.

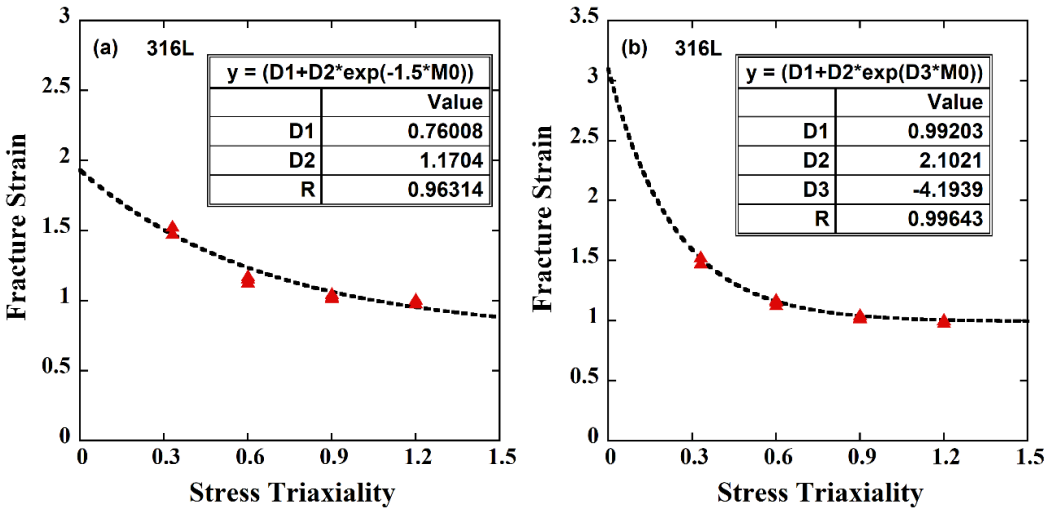

(cont. on next page)

Figure 5.23**.** The JC failure model parameters (a-d) D_1, D_2, D_3, D_4 for 316L and (e-h) for AISI 4340

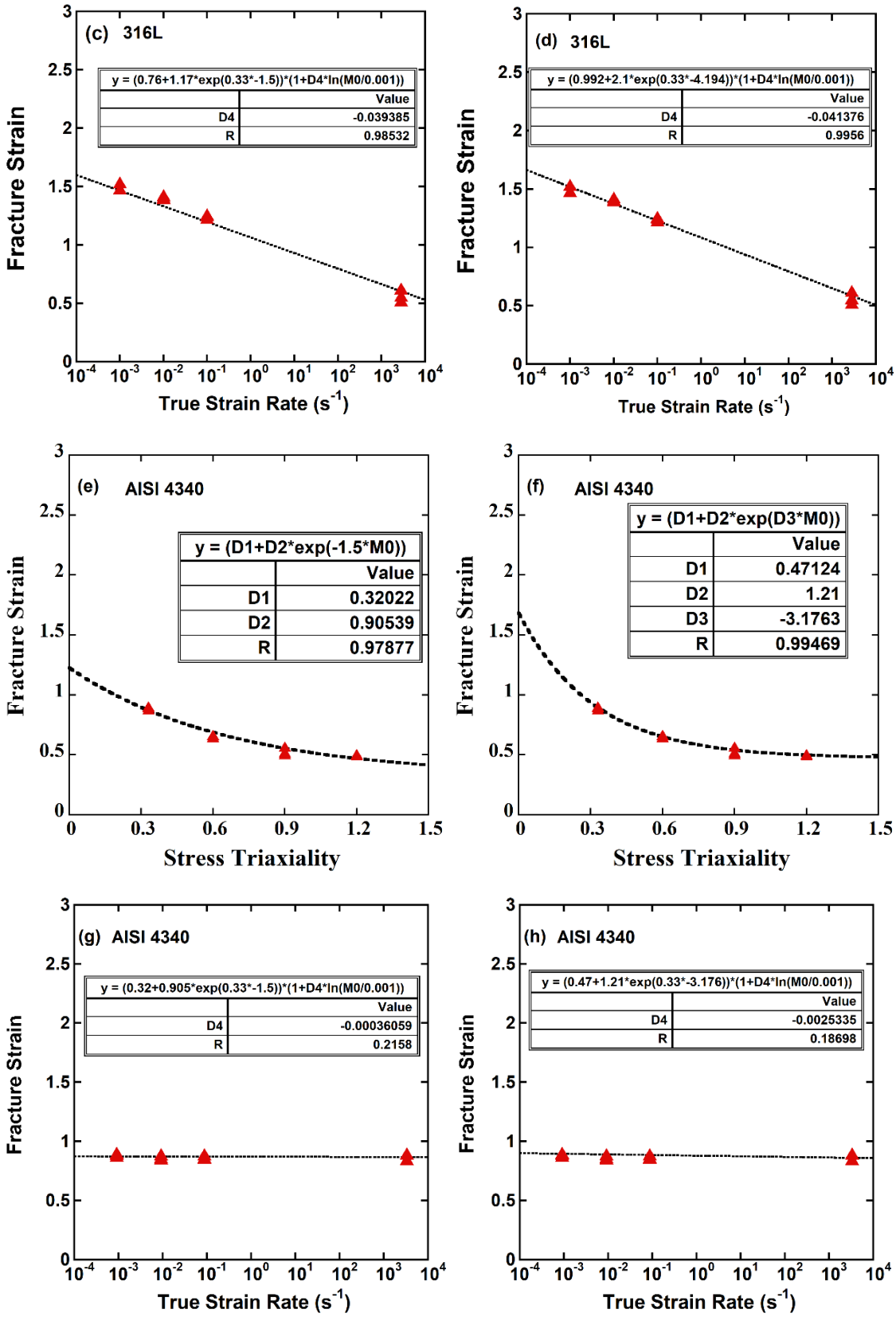

Figure 5.23 (cont.)

5.2. Program Results of Quasi-static and Dynamic Tests

By entering the force-displacement data from the test data into the program, the engineering stress-engineering strain curves of the test at each strain rate are calculated and shown in Figure 5.24(a) and (b), sequentially for 316L and AISI 4340. Calculations were made by entering one test data from three test data performed at each strain rate in the program. True stress-true plastic strain curves of the tests at each strain rate from the engineering stress-strain data found as a result of the program calculation in Figure 5.24 are shown in Figure 5.25(a) and (b) for 316L and AISI 4340, respectively.

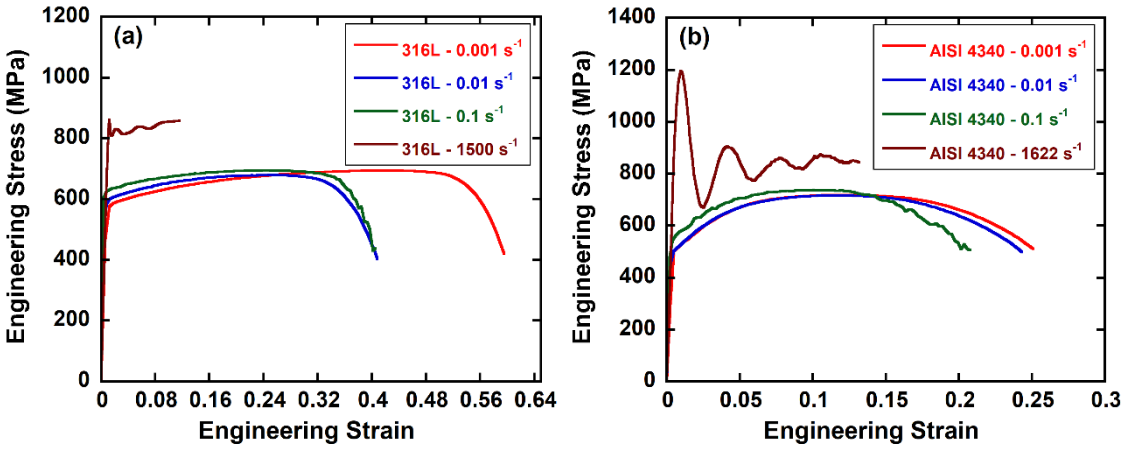

Figure 5.24. The code engineering stress-strain curves of (a) 316L, and (b) AISI 4340

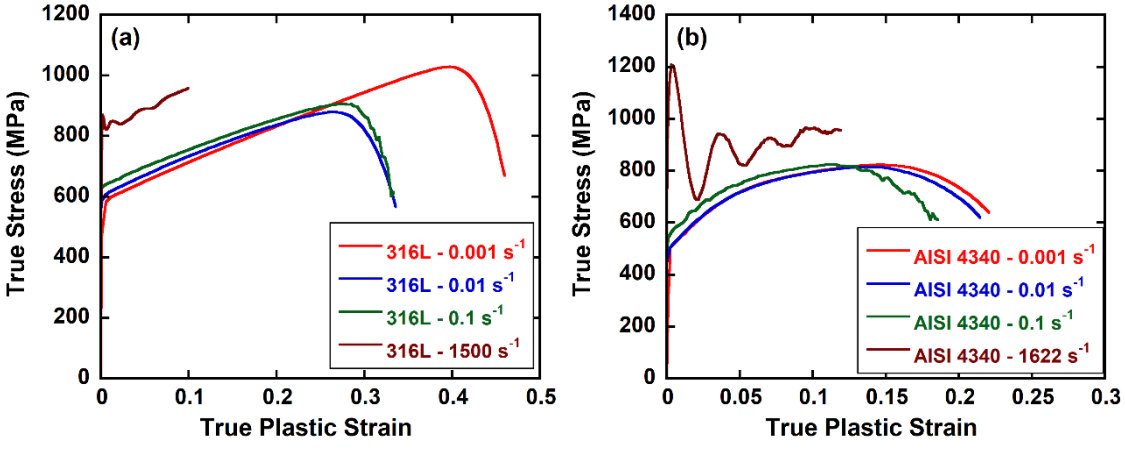

Figure 5.25. The code true stress-true plastic strain curves of (a) 316L, and (b) AISI 4340

Figure 5.26. (a-d) shows the fit that was fitted to the true stress-true plastic strain curve calculated at each tested strain rate by using the fit fitting method to determine the

A, B and n values of the Johnson-Cook strength equation parameters for 316L material. Figures 5.26(a-d) show sequentially the code determined values of *A, B and n* of 316L at $1x10^{-3}$ s^{-1}, $1x10^{-1}$ s^{-2}, $1x10^{-1}$ s^{-1} and 1500 s^{-1}. Figure 5.26 (e-h) shows the fit to the true stress-true plastic strain curve for AISI 4340 material at each tested strain rate. This fit was used to determine the values of the Johnson-Cook strength equation parameters *A, B, and n*. Figures 5.26(e-h) show sequentially the code determined values of *A, B and n* of AISI 4340 at $1x10^{-3}$ s^{-1}, $1x10^{-1}$ s^{-2}, $1x10^{-1}$ s^{-1} and 1622 s^{-1}. The yield stress of *A* value of 316L at $1x10^{-3}$ s^{-1} is determined *582.9764 MPa* and the values of *B* and *n* are *1022.41833 MPa*, and *0.87826*, respectively. These are sequentially *630.9394 MPa, 729.39271MPa and 0.7562* for 4340 alloy at the same reference strain rate.

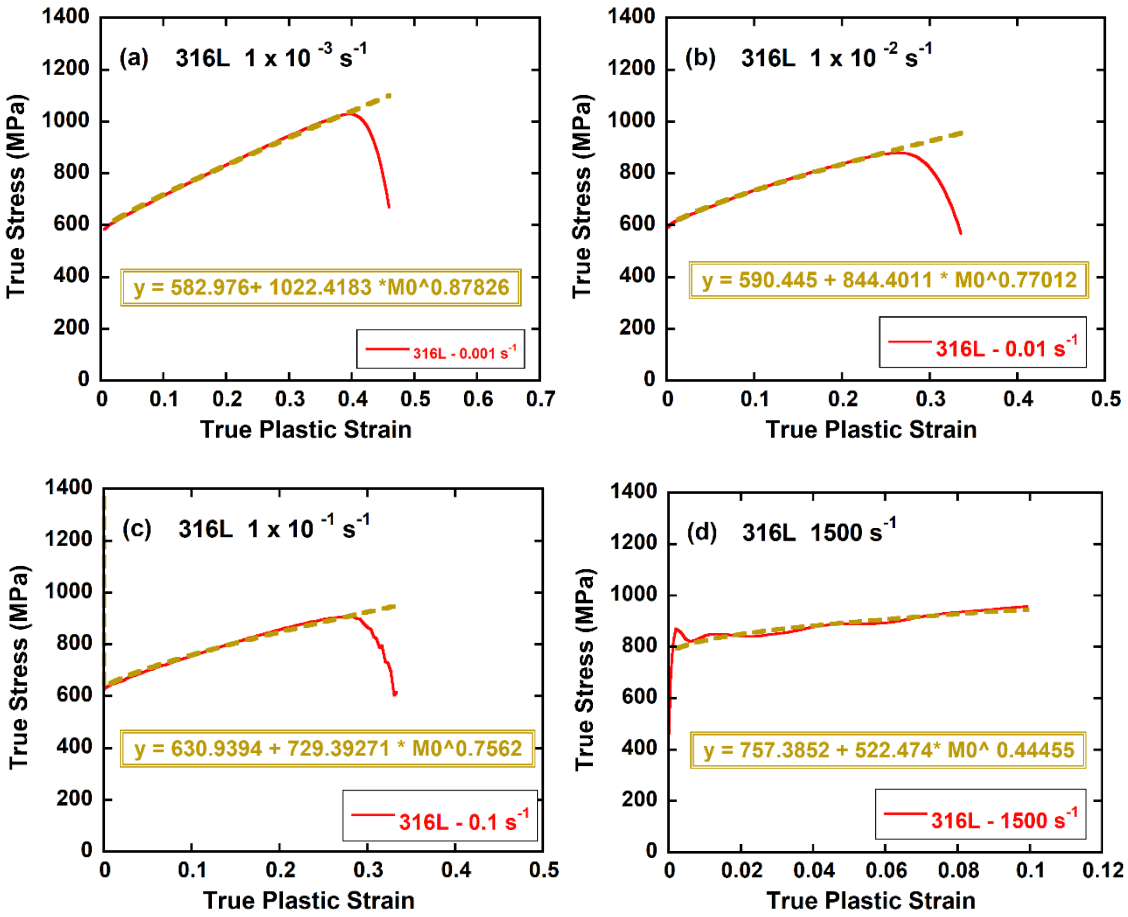

(cont. on next page)

Figure 5.26. Determination of the JC A, B and n parameters through true stress-true plastic strain curves of (a-d) 316L, and (e-h) AISI 4340 material according to program results at (a, e) $1x10^{-3}$, (b, f) $1x10^{-2}$, (c, g) $1x10^{-1}$ s^{-1}, (d) 1500 s^{-1} (for 316L), and (h) 1622 s^{-1} (for AISI 4340).

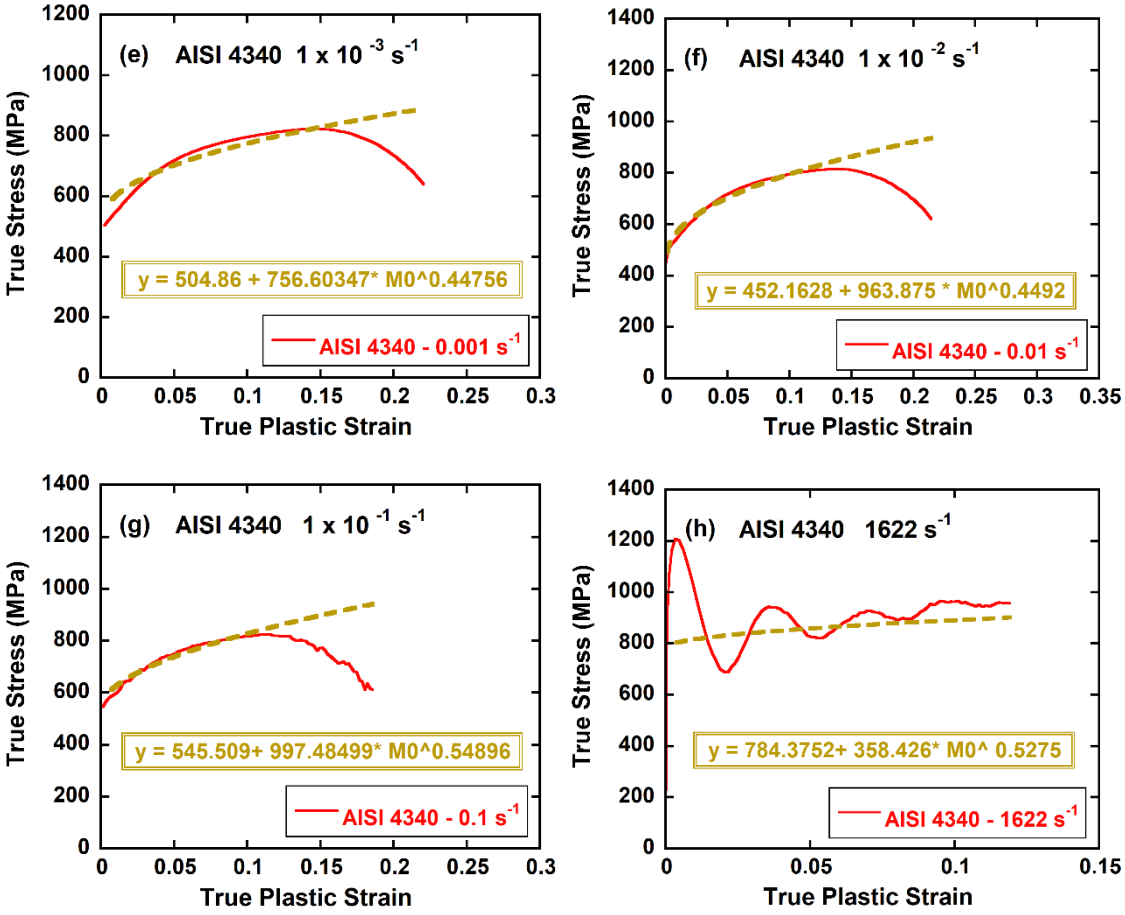

Figure 5.26 (cont.)

The determination of the second bracket strain rate effect parameter *C* value of the JC strength equation obtained for the 1x10^{-3} s^{-1} reference strain rate ($\dot{\varepsilon_0}$) for the 316L material through the program is shown in Figure 5.27(a-c). The *C* parameter in the program is determined by the fit method based on the stress values at *0.1* strain from the equivalent stress-strain curves obtained by the MLR method. The *C* parameter from experimental data calculated from the true stress-true plastic strain curves and MLR curves of tests at four different strain rates. Experimental results were calculated by entering 3 test data at each strain rate. A maximum of 6 different test data can be entered in the program. In the program calculation, it was calculated by entering test data at each strain rate, and the *C* parameter was calculated by entering another test data at 1x10^{-3} s^{-1} and 1x10^{-2} s^{-1} strain rates. The curve fitting equation $\sigma_0(1 + Cln\left(\frac{\dot{\varepsilon}}{\dot{\varepsilon_0}}\right))$ is assigned to the average stress JC equation at the reference strain rate ($\dot{\varepsilon_0}$) 1x10^{-3} s^{-1}. For the reference strain rate ($\dot{\varepsilon_0}$) 1x10^{-3} s^{-1}, the stress (σ_0) value of 316L material at *0.1* strain is *742.52 MPa*. As a result of the curve fitting equation, the *C* value determined by entering one

test data at each strain rate of the 316L material is *0.019559*, as shown in Figure 5.27(a), and the *C* value determined by entering another test data at $1x10^{-2}$ s^{-1} and $1x10^{-1}$ s^{-1} strain rates is *0.018828*, as shown in Figure 5.27(b). By entering the test data at $1x10^{-3}$ s^{-1} and 1500 s^{-1} strain rates in Figure 5.27(c), the value found in the calculation of the *C* parameter was obtained as *0.019439* from stress values at 0.1 strain for the 316L material. In the experimental results, the *C* value was calculated with *3* data values at each strain value for a total of *12* data, while in the program it was first calculated with a total of *4* data, *6* data and *8* data. It has been observed that determining the *C* value in the program converges to the *C* value found in the experimental results as the number of data increases. The determination of the strain rate effect parameter *C* for the JC strength equation of AISI 4340 material at a reference strain rate of $1x10^{-3}$ s^{-1} is shown in Figure 5.28. The *C* parameter was determined using the fit method on stress values at 0.05 strain from MLR-derived equivalent stress-strain curves. Experimental *C* values were calculated from true stress-true plastic strain and MLR curves at four different strain rates, using three data points per rate. Initially, *C* values were calculated with *4, and 8* data points. The program's *C* value converged to the experimental value as more data were added. For example, the stress (σ_0) value at *0.05* strain for $1x10^{-3}$ s^{-1} is *742.52* MPa. With one test data point per strain rate, *C* was *0.01351*; with additional data at $1x10^{-2}$, $1x10^{-1}$, $1x10^{-3}$ and 1500 s^{-1} was *0.013755*. The code calculated true-stress strain curves based on the *A, B and n* values obtained at each strain rate are shown in Figure 5.29(a) and (b) for 316L and AISI 4340, respectively.

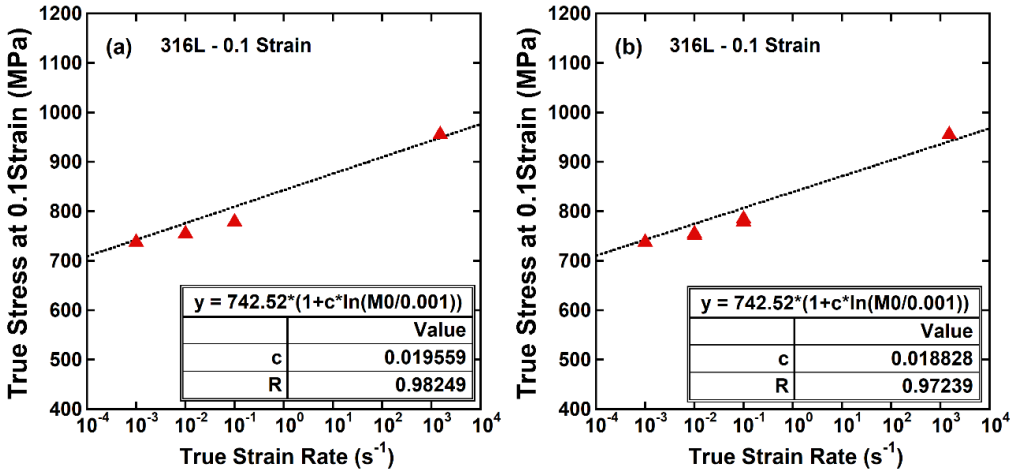

(cont. on next page)

Figure 5.27. The code calculated JC *C* parameter using the MLR method for 316L (a) single, (b) two and (c) three flow stress data

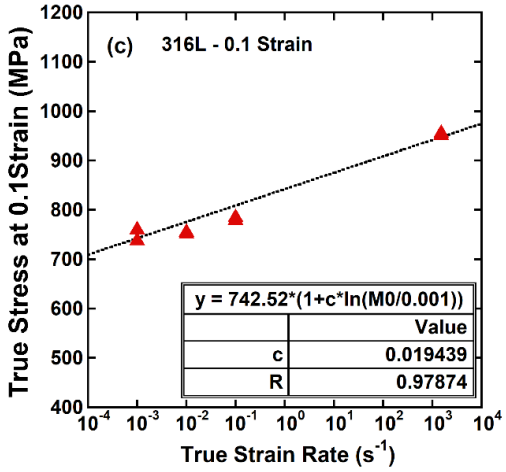

Figure 5.27 (cont.)

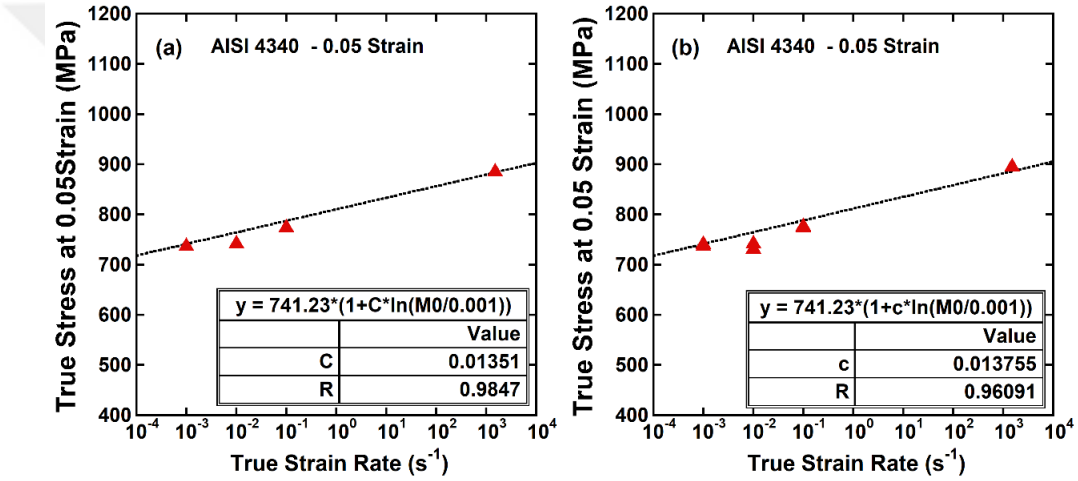

Figure 5.28. The code calculated JC *C* parameter using the MLR method for AISI 4340 (a) single, (b) three flow stress data

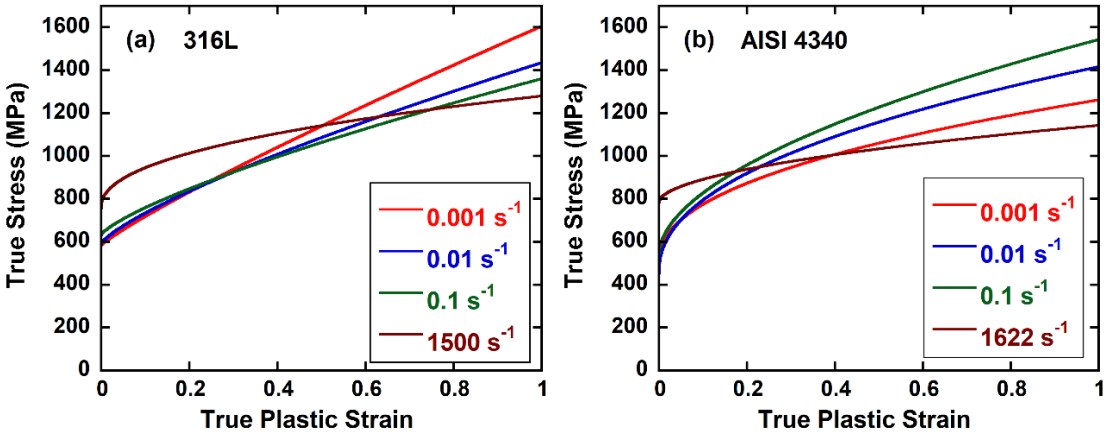

Figure 5.29. The code calculated true-stress strain curves based on the *A, B and n* values obtained at each strain rate, (a) 316L and (b) AISI 4340

The *A, B, and n* values at $1x10^{-3}$ s^{-1} reference strain rate determined from the equivalent stress-strain curves calculated in the program and the graphs of the equivalent stress-strain curves with the determined *C* value at different strain rates are shown in Figure 5.30. The *C* value determined for 316L material by the equivalent stress-strain curves at $1x10^{-3}$ s^{-1} in the program, and the *A, B and n* values at $1x10^{-3}$ s^{-1} reference strain rates determined from the true stress-true plastic strain curve and the results of other strain rate curves, as shown in Figure 5.30. The *A, B, n* values determined at $1x10^{-3}$ s^{-1} reference strain rate and the *C* values determined from the test data entered for each strain rate are *582.9764 MPa*, *1022.41833*, *0.87826* and 0.019559, as shown in Figure 5.30(a). True stress-true plastic strain curves are shown in Figure 5.30(b) according to the *C* value (*0.018828*) determined by entering another test data at $1x10^{-2}$ and $1x10^{-1}$ s^{-1} strain rates. True stress-true plastic strain curves are shown in Figure 5.30(c), according to the *C* value (*0.019439*) calculated from 8 data, including $1x10^{-3}$ and 1500 s^{-1} strain rates. The *A, B, n* values determined at $1x10^{-3}$ s^{-1} reference strain rate and the *C* values determined for AISI 4340 material from the test data entered for each strain rate are *504.86 MPa*, *756.6*, *0.44756* and 0.01351, as shown in Figure 5.30(d). These results highlight the critical role of the Johnson-Cook (JC) model parameters (*A, B,* and *n*) and the strain rate sensitivity parameter (*C*) in accurately characterizing the mechanical behavior of 316L and AISI 4340 alloys under varying strain rates.

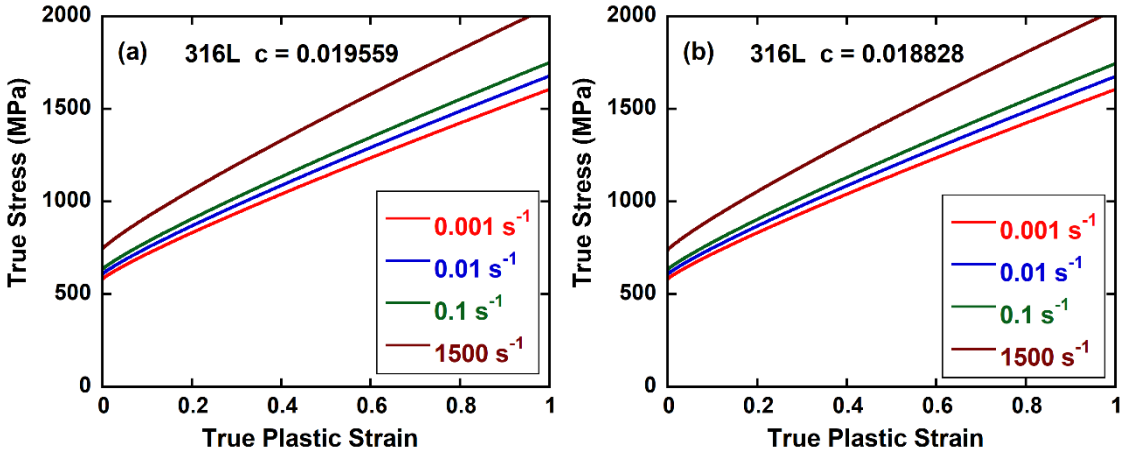

(cont. on next page)

Figure 5.30. The code true stress-true plastic strain curves at different strain rates (a-c) 316L and (d) AISI 4340

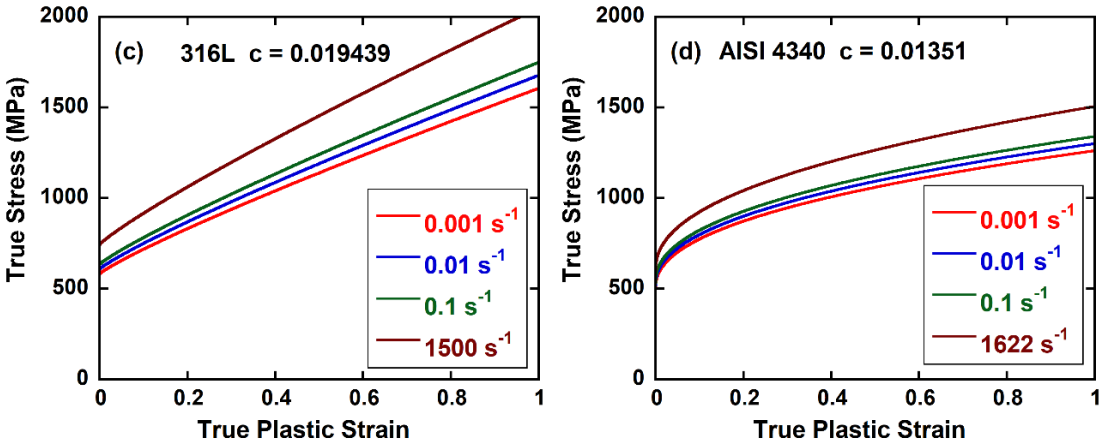

Figure 5.30 (cont.)

In Figure 5.31 (a-d), in order to verify the JC parameters calculated from the test data entered in the program with the test result curves. Comparison of separate test and model curves for *c* values determined by test data is shown. Since the test data contained too much data, the test data entered into the program was further reduced with the weighted mean process and calculations were made. Figure 5.32 (a-d) shows the comparison of experimental test and model. The code determined and JC stress-strain curves of 316L are shown Figure 5.31(a-c) for different *c* values. Figure 5.31(d) shows the code determined and JC stress-strain curves of AISI 4340 at different strain rates. The code determined and experimental stress-strain curves of 316L and AISI 4340 at different strain rates are shown in Figure 5.32(a-d).

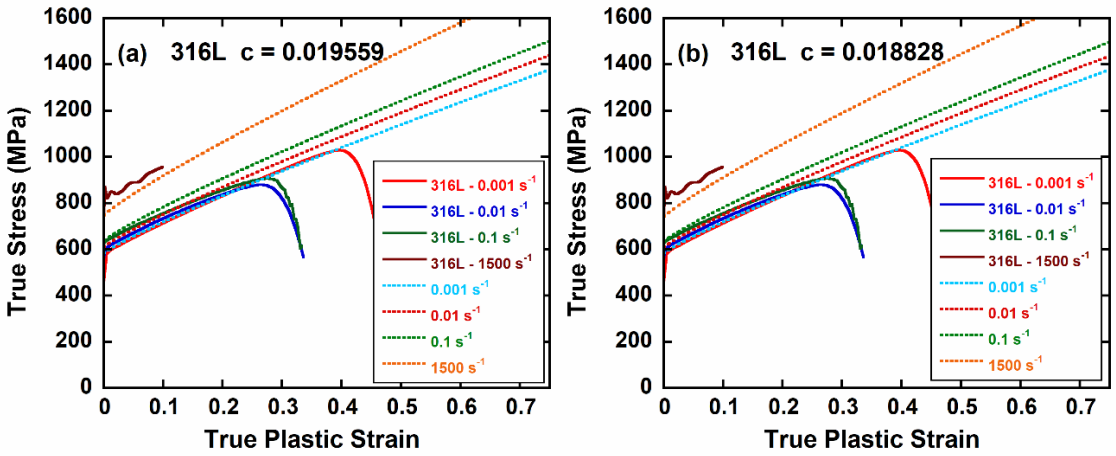

(cont. on next page)

Figure 5.31. The code determined and JC stress-strain curves of (a-c) 316L and (d) AISI 4340 at different strain rates

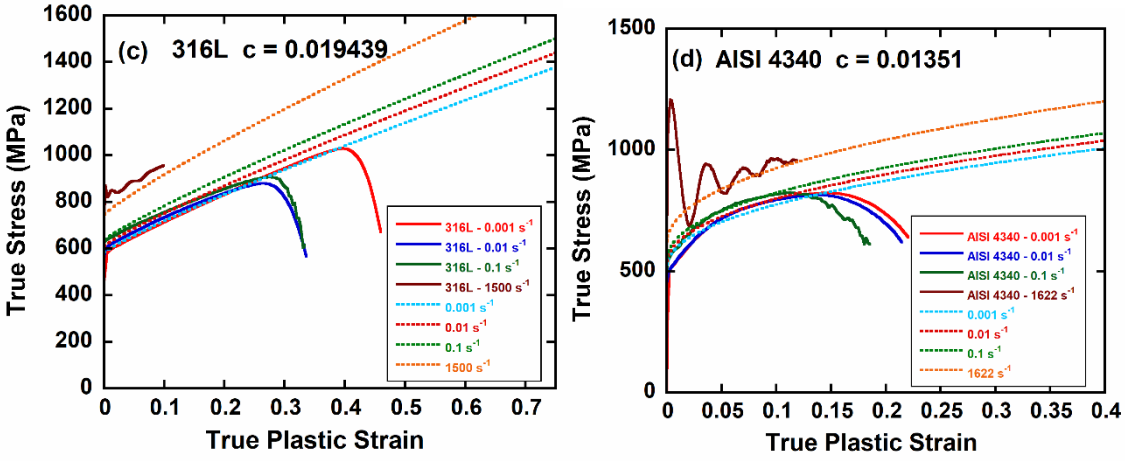

Figure 5.31 (cont.)

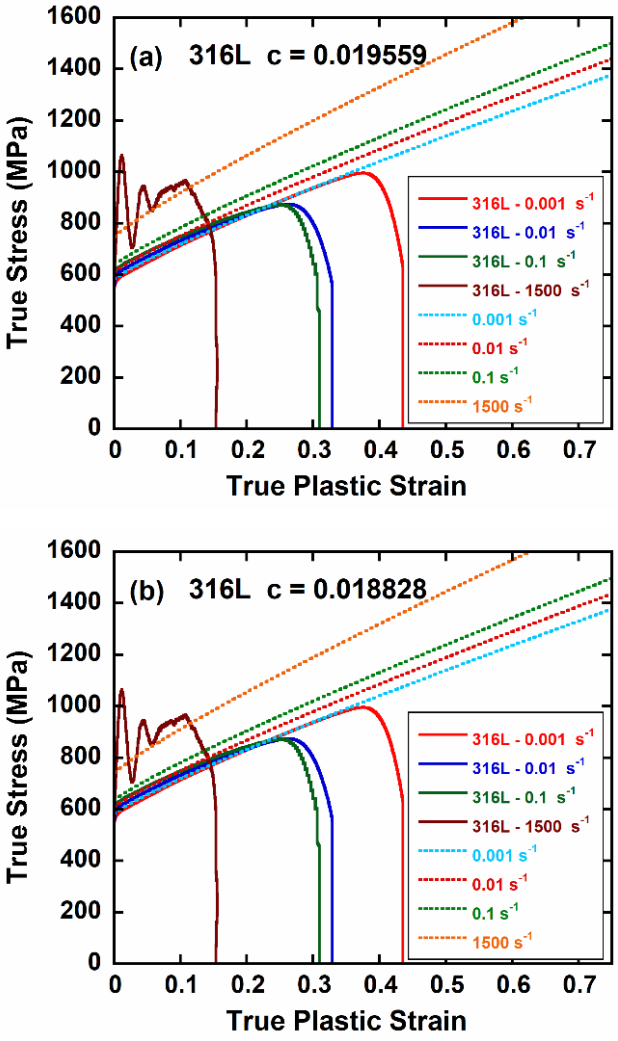

(cont. on next page)

Figure 5.32. The code determined and experimental stress-strain curves of (a-c) 316L and (d) AISI 4340 at different strain rates

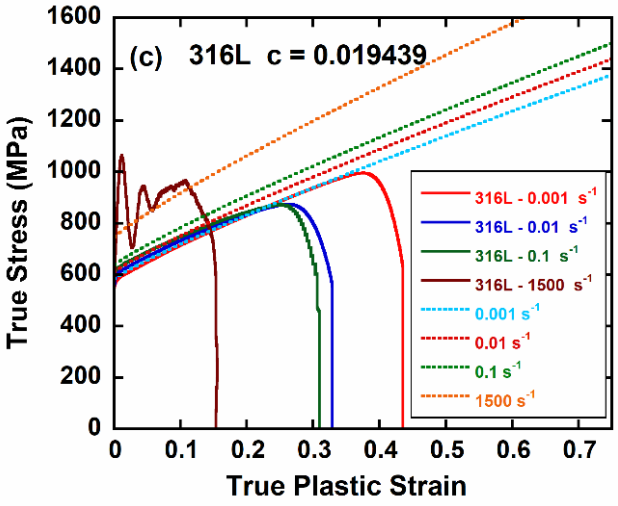

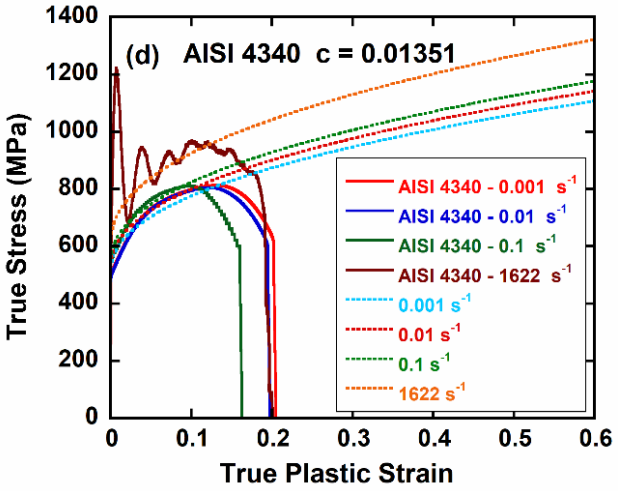

Figure 5.32 (cont.)

By taking test images at certain time intervals through the test videos designed in the program content, an example measurement of the diameter and radius measurements in the captured image is shown in Figure 5.33(a-f) at different times. Tensile test video data taken in the test at $1x10^{-3}$ s^{-1} is the program measurement output for 316L and AISI 4340 materials. In the program, the user enters the number of diameter and radius to be measured, divides the video duration by the entered number, and takes images in equal areas to perform diameter and radius measurements. The force values in the video image durations are entered into the experimental data file into the program and the force values in the image durations are read. Average true stress-true plastic strain calculations are performed for the measured diameter and radius values.

To determine the equivalent stress, Bridgman's constant and MLR constant are calculated for the measured diameters and radius. By multiplying the calculated constants

of both methods with the average true stress values, equivalent tensile strain values are calculated for two different methods. Curve representations of the calculated data in Figure 5.33(a-f) are seen as program output. Determination of JC *A, B and* n values from the drawn curves to the equivalent stress curve determined by the Bridgman method is determined by the fit fitting method. The curve is displayed with the determined value results.

Additionally, this process allows for a more accurate and detailed analysis of the material properties under varying strain rates, enhancing the reliability of the JC model parameters. The program's ability to automate and visualize these measurements significantly improves the efficiency and accuracy of the experimental data analysis, making it a valuable tool for researchers studying the mechanical behavior of materials. This integration of image analysis with stress-strain calculations provides a comprehensive approach to material testing, ensuring precise and reproducible results.

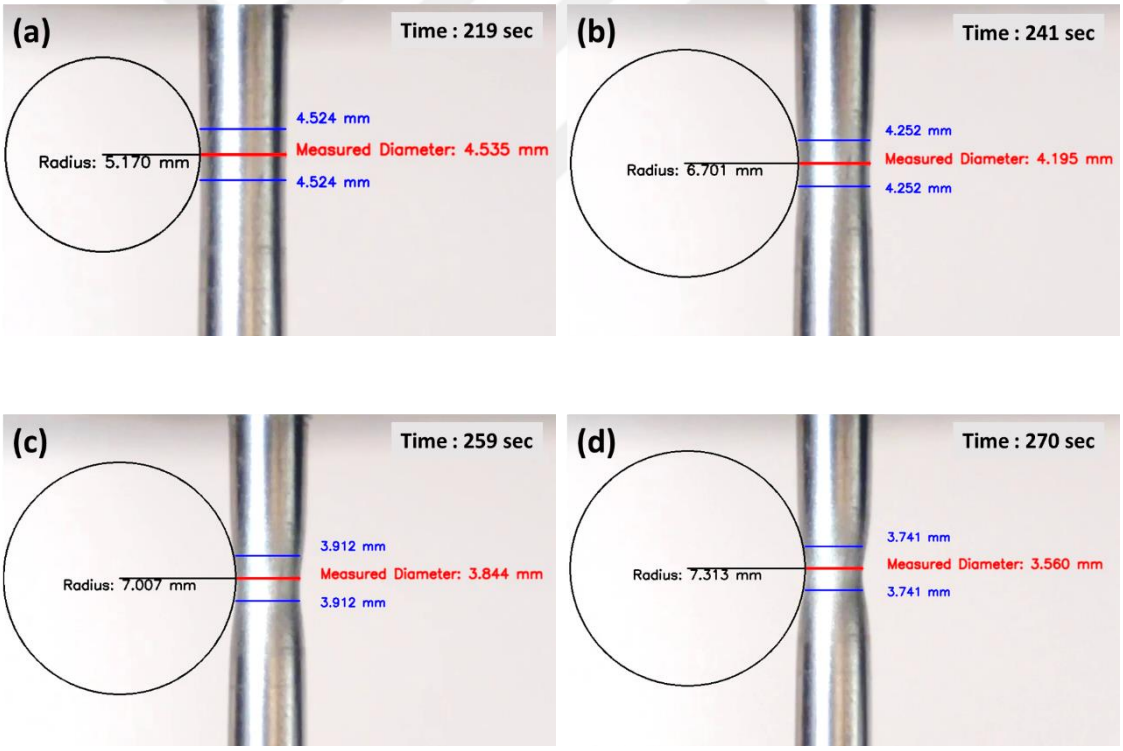

(cont. on next page)

Figure 5.33. Image taken at certain intervals through the program and sample display of diameter and radius measurement on the image at different times

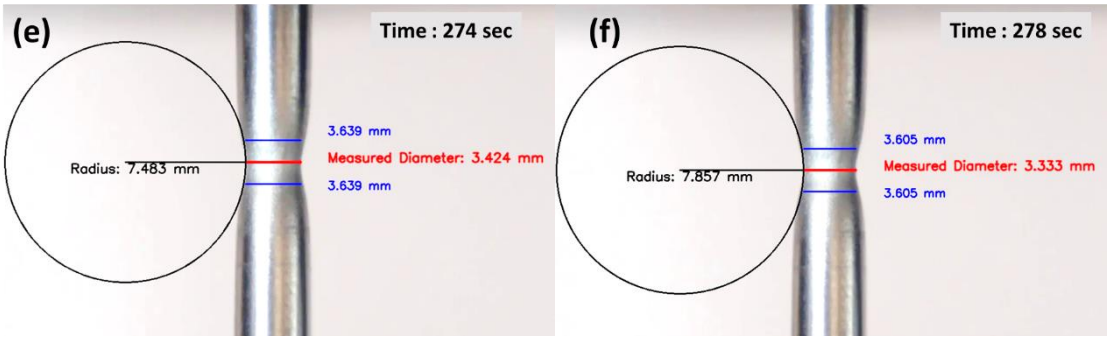

Figure 5.33 (cont.)

Based on the tensile test video of the 316L material at a strain rate of 1 x 10^{-3} s^{-1}, measurements were taken at 20 equally spaced points between the start of necking and the breaking time. These measurements include the diameter and radius values in the necking area, average stress, equivalent stress using the Bridgman method, and equivalent stress results using the MLR method, as shown in Figure 5.34(a-c). To assess material behavior before necking, diameter measurements were made from snapshots at 10 equally spaced points between the start of the test and the onset of necking. Average true stress values were calculated based on the force values corresponding to these points in the experimental test data. Following the onset of necking, the necessary calculations were performed using the appropriate formulas. The JC (JC) strength model parameters were determined based on the resulting curves for each measurement.

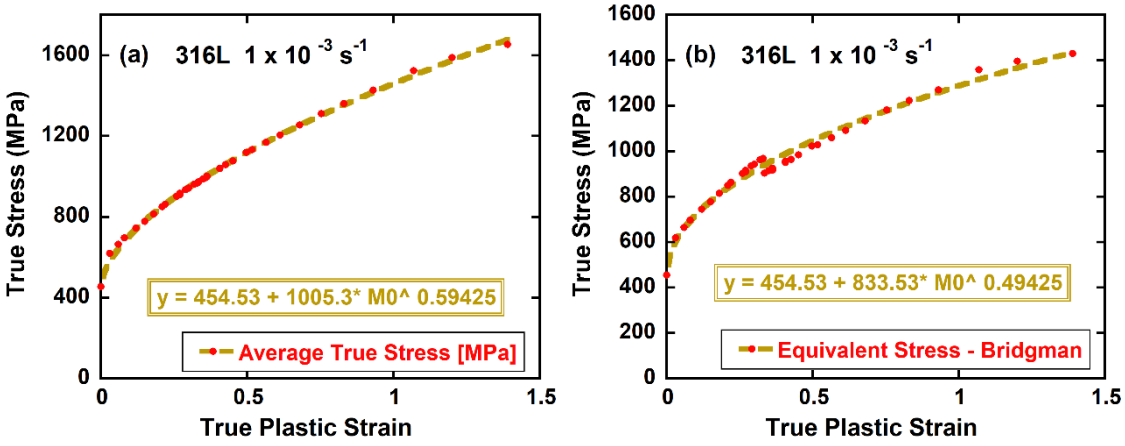

(cont. on next page)

Figure 5.34. Average true stress and equivalent stress graph results and determination curves of the JC, *A, B and n* parameters with test videos of 316L material through the program.

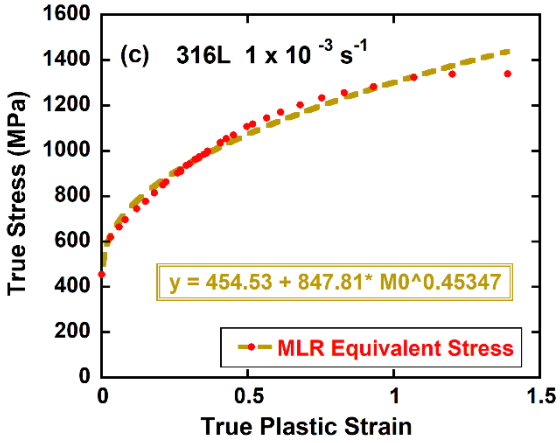

Figure 5.34 (cont.)

Based on the tensile test video of the AISI 4340 material at 1 x 10^{-3} s^{-1} strain rate, the snapshot of the material at *20* points equal between the necking start time and the breaking time, measurements of the diameter and radius values in the necking area, average stress, equivalent stress with the Bridgman method. and equivalent stress results with the MLR method are shown in Figure 5.35(a-c).

To determine the material behavior before necking, diameter measurements were made from snapshots at *10* equal points between the necking start time and the test start moment. Average true stress values were calculated according to the force values in the periods corresponding to these points, according to the force values in the experimental test data. After the necking start time was calculated in the same way. After the measurements, it was calculated with the necessary formulas. The JC strength model parameters were determined based on the result curves. JC parameter determination was carried out for each curve determined.

In Figure 5.35(a), the determination of Johnson-Cook (JC) strength model parameters (*A, B, and n*) for the Average True Stress-True Plastic Strain curve was conducted using the fit method. Figure 5.35 (b) illustrates the equivalent stress values obtained using the Bridgman correction method, where stress values before necking were considered as average true stress values. Figure 5.35 (c), the result curve of the MLR equation and equivalent stress values is shown.

Determined *A, B and n* values and average true stress, Bridgman equivalent stress and MLR Equivalent stress values for *1000* points with strain values between *0* and *1*, together with the experimental true stress-true plastic strain graph for the 1x10^{-3} s^{-1} test Comparison of *A, B and n* parameter result curves is shown in Figure 5.36(a) and (b).

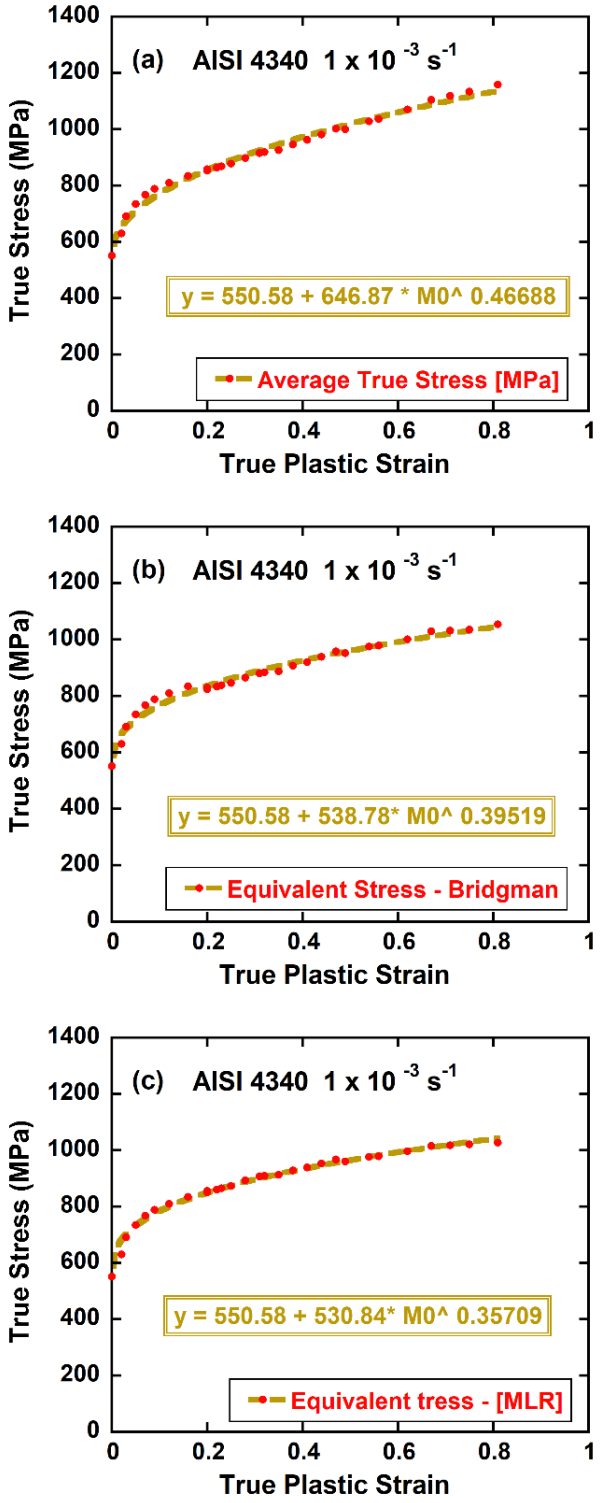

Figure 5.35.Average true stress and equivalent stress graphs, along with the determination of JC parameters *A, B, and n*, using test videos of AISI 4340 material through the program

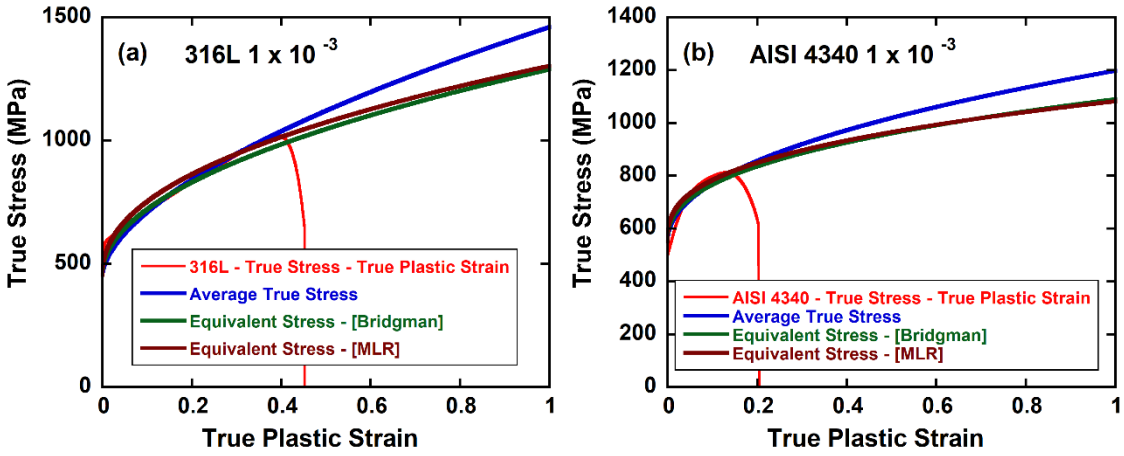

Figure 5.36. Test videos of (a) 316L and (b) AISI 4340 material and determination results of Johnson-Cook, *A*, *B* and *n* parameters of average true stress and equivalent stress graphs with program

The JC strength equation's strain rate coefficient *C* is not determined within the program. Instead, the *C* parameter was calculated from test data based on the stress value at *0.1* strain for 316L material. Since this value is before the onset of necking, the average true stress values at *0.1* strain correspond to experimental true stress data. The previously determined *C* value for *0.1* strain was *0.019439*. Using this *C* value, the *A*, *B*, *and n* parameters were calculated, and the stress-strain curves of the alloys at strain rates of $1x10^{-3}$, $1x10^{-2}$, $1x10^{-1}$, and 1500 s^{-1} are shown in Figure 5.37(a-c), respectively.

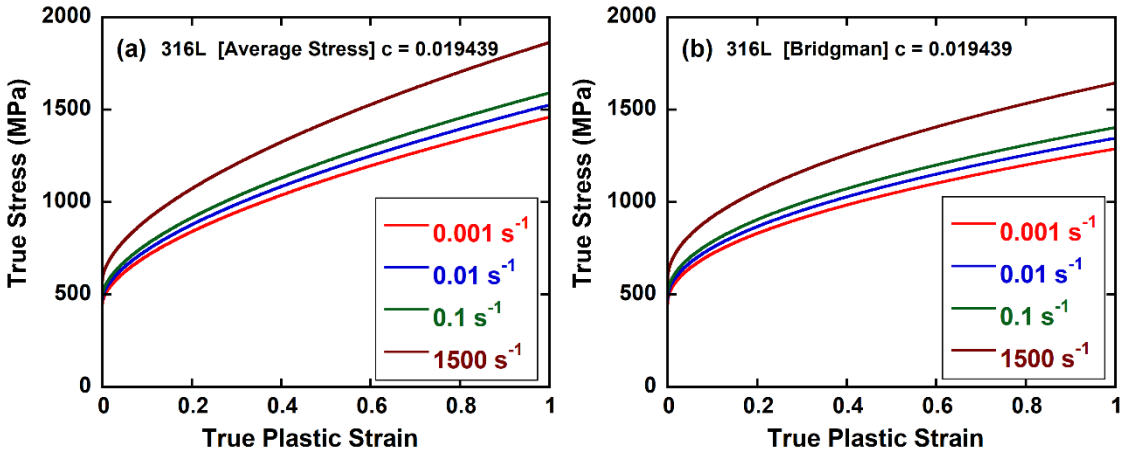

(cont. on next page)

Figure 5.37. Stress-strain behavior of 316L material at various strain rates using the JC parameters *A*, *B*, *n*, and a *C* value from calculated video program of 0.019439 determined from 0.1 strain

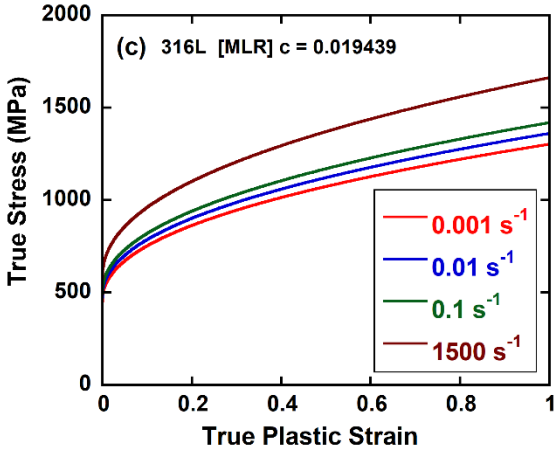

Figure 5.37 (cont.)

The parameter *C* was also calculated from test data based on the stress value of *0.05* strain of AISI 4340 material in the program. Since the *0.05* strain value is a value before the necking starting point, our average true stress values at that strain point will be experimental true stress data. The *C* value previously determined through the program for *0.05* on the test data was assigned a value of *0.013755*. The *A*, *B* and *n* values calculated by including the determined *C* value into the equation and the stress-strain behavior of the material at $1x10^{-3,}$ $1x10^{-2}$, $1x10^{-1}$ and 1622 s^{-1} are shown in Figure 5.38(a-c), respectively.

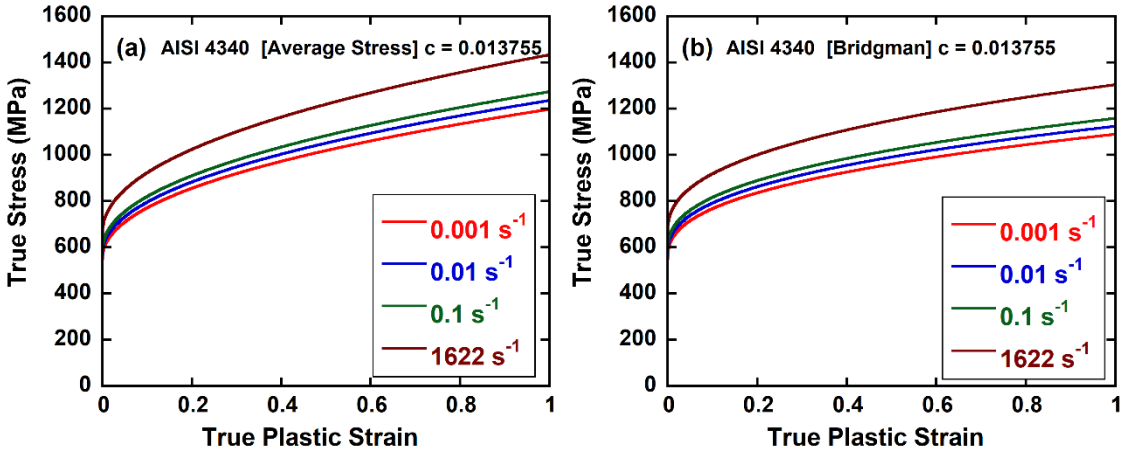

(cont. on next page)

Figure 5.38. Stress-strain behavior of AISI 4340 material at different strain rates using JC parameters *A*, *B*, *n*, and *C* value of 0.013755 determined from 0.05 strain in the video program

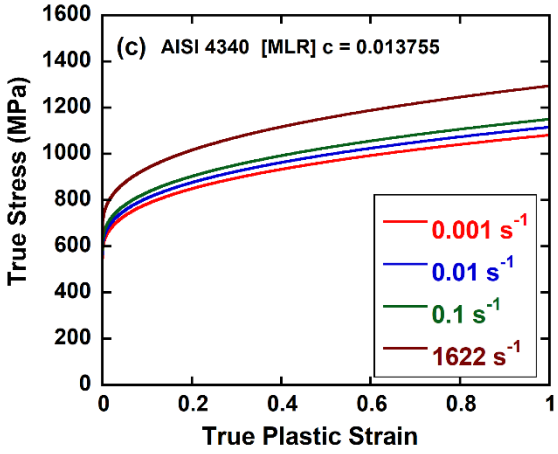

Figure 5.38 (cont.)

In Figure 5.39(a-c), the determined average true stress-true plastic strain at a reference strain rate of $1x10^{-3}$ s^{-1} for 316L material is shown. The equivalent stress using the Bridgman method and the MLR method, along with the *A*, *B*, *n*, and *C* values, are presented. The stress-strain behavior curves of the material at strain rates of $1x10^{-2}$, $1x10^{-1}$, and 1500 s^{-1} are also drawn. A comparison of the experimental true stress-true plastic strain curves from tensile tests at these strain rates and the test-model fit is illustrated.

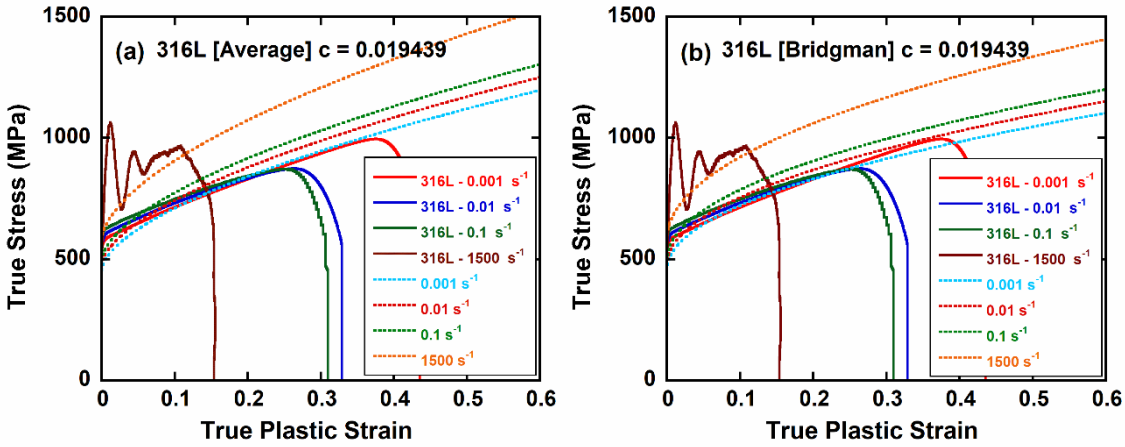

(cont. on next page)

Figure 5.39. Equivalent stress results for 316L material at a strain rate of $1x10^{-3}$ s^{-1}, determined from the test video using average true stress-true plastic strain, Bridgman method, and MLR method, based on measurements made in the program

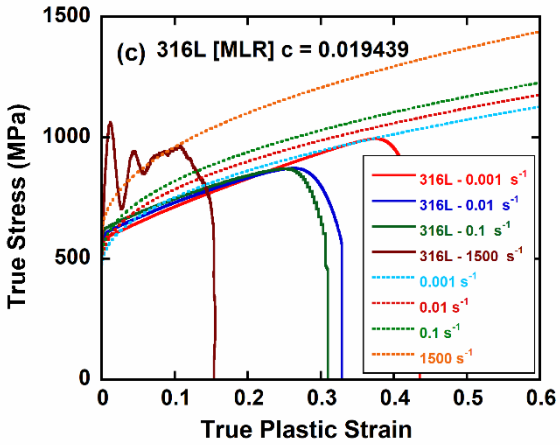

Figure 5.39 (cont.)

In Figure 5.40(a-c), the stress-strain behavior of 316L material is analyzed. The graphs include the average true stress-true plastic strain curve at a reference strain rate of $1x10^{-3}$ s^{-1}, as well as the equivalent stress curves determined using the Bridgman method and the MLR method. The *A, B, n, and C* values are calculated and used to plot the material's behavior at additional strain rates of $1x10^{-2}$, $1x10^{-1}$, and 1622 s^{-1}. These figures also compare the experimentally obtained true stress-true plastic strain curves from tensile tests at these various strain rates with the model predictions, illustrating how well the model fits the experimental data.

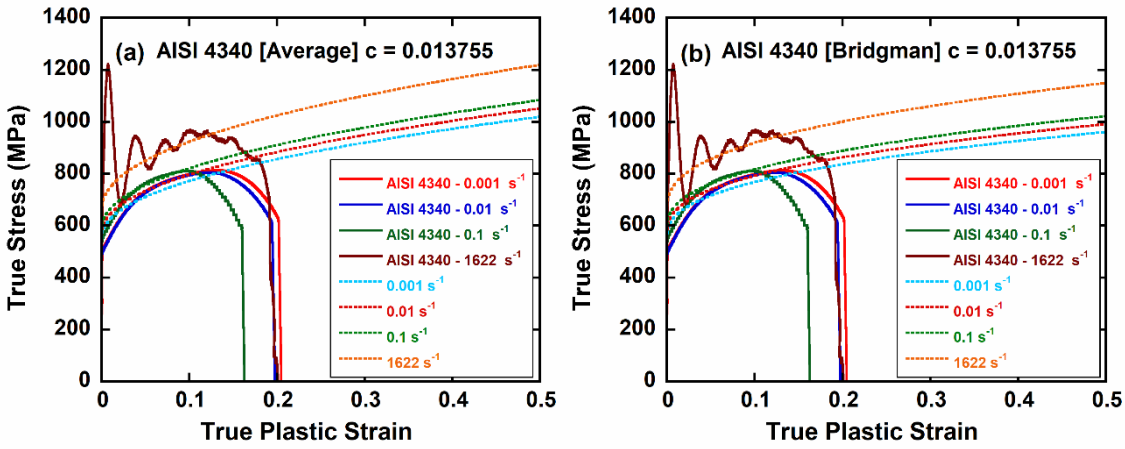

(cont. on next page)

Figure 5.40. Equivalent stress result curves determined by average true stress-true plastic strain, equivalent stress [Bridgman] and MLR method of the test video of AISI 4340 material at $1x10^{-3}$ s^{-1} strain rate, as a result of the measurements made on the program

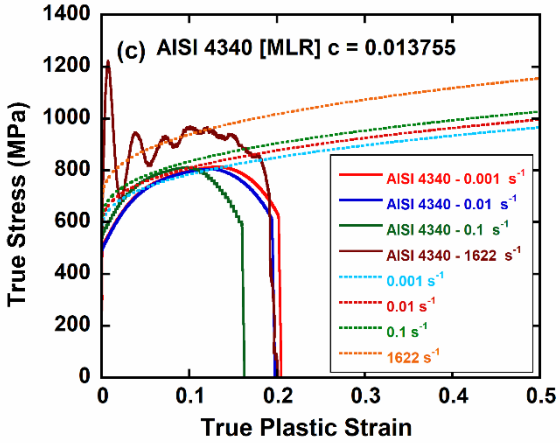

Figure 5.40 (cont.)

Figure 5.41 shows graphical representations of the values obtained as a result of calculating the JC failure model equation parameters with the developed program. In the program, the parameters D_1, D_2, D_3, D_4 were determined from the JC failure equation constants, which are the equivalent fracture plastic strains of 316L and AISI 4340 materials. The data of the tests with *4* different stress triaxiality values were entered into the program and the fracture strain value of each data was calculated. To determine the D_1, D_2 and D_3 values, the calculated fracture strain values were plotted against the stress triaxiality values. The damage equation parameters found for the 316L material by the fit method to the plotted data are shown in Figure 5.41 (a-b). In Figure 5.41 (a), D_1 and D_2 parameters were determined by assigning *-1.5* value to D_3 parameter to the program. According to the program output, when the D_3 value was determined as *-1.5*, the program found the values of the D_1 and D_2 parameters as *0.7601 and 1.1704*, respectively. In Figure 5.41 (b), as a result of calculating the D_1, D_2 and D_3 parameters without assigning a value to the D_3 value, the program values are *0.99203, 2.10198 and -4.19385*, respectively. The D_4 parameter in the damage equation is determined with the D_1, D_2 and D_3 parameter values determined in the program. Quasi-static and dynamic tests of samples with a stress triaxiality value of *0.33* were used. The parameter D_4 was found by performing linear curve fitting on the fracture strain-strain rate curve drawn on a logarithmic basis. The D_4 damage parameter found by determining the D_3 value of the 316L material as *-1.5* is shown in Figure 5.41(c). D_4 parameter was obtained as *-0.0399*. The graph in Figure 5.41(d) shows the determination of D_4 with the results calculated without entering a value into the D_4 parameter value. Accordingly, the D_4 value was obtained as *-0.0414*. Figure 5.41 (e-h) shows the graphs of determining the equivalent

fracture plastic deformations of the AISI 4340 material and the parameters D_1, D_2, D_3, D_4 from the JC fracture equation constants, according to the data processing results in the program. Figure 5.41(e) shows the determination of D_1 and D_2 parameters according to the compatibility equation by assigning a value of *-1.5* to the D_3 parameter of the AISI 4340 material according to the program output. When the D_3 value is *-1.5*, the values of the D_1 and D_2 parameters are *0.3202 and 0.90537*, respectively. The graph shown in Figure 5.41 (f) shows the results of parameter determination without assigning an input to D_3 in the program. According to the created fit equation, the values of D_1, D_2 and D_3 parameters are *0.47122, 1.2098 and -3.175*, respectively. According to the program output, the $D4$ damage parameter found with the input of *-1.5* of the D_3 value of the AISI 4340 material is shown in Figure 5.41(g). As a result of this input, the D_4 parameter was calculated as *-0.0004*. The value of parameter D_4 determined in the graph in Figure 5.41(h) shows the determination of D_4 in the program calculation when no value input is assigned to the value D_3. Accordingly, the D_4 value was obtained as *-0.0026*. The program calculates the JC failure model parameters D1, D2, D3, and D4 for 316L and AISI 4340 materials using test data at different stress triaxiality values. It compares methods with and without predetermined D3 values, providing insights into fracture behavior. Figure 5.41 demonstrates the differences in parameter values, showcasing the program's ability to accurately fit and determine JC failure parameters for predicting material failure.

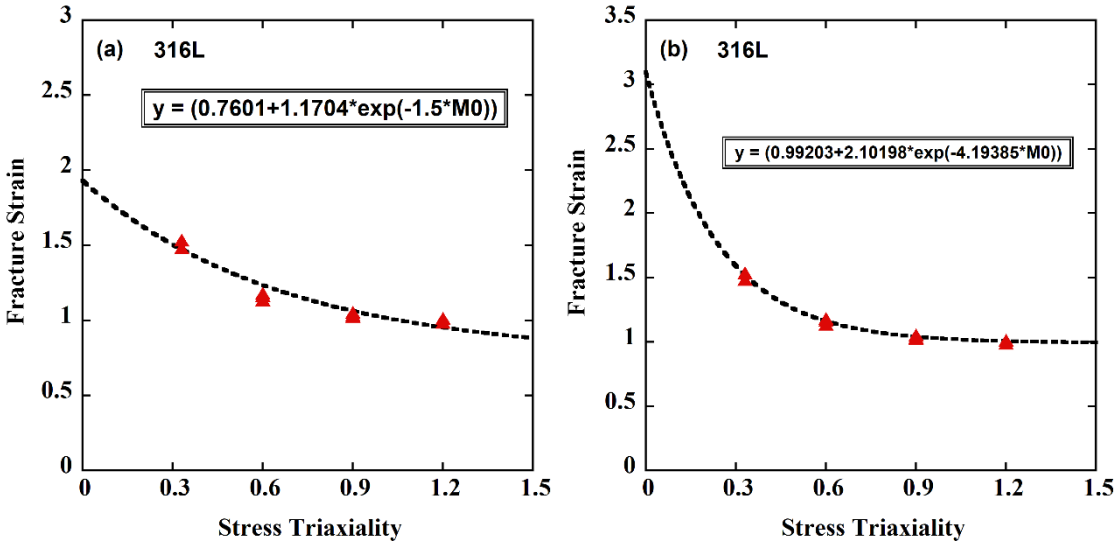

(cont. on next page)

Figure 5.41. Determination of JC failure model parameters D_1, D_2, D_3, D_4 values for (a-d) 316l and (e-f) AISI 4340 materials through the program

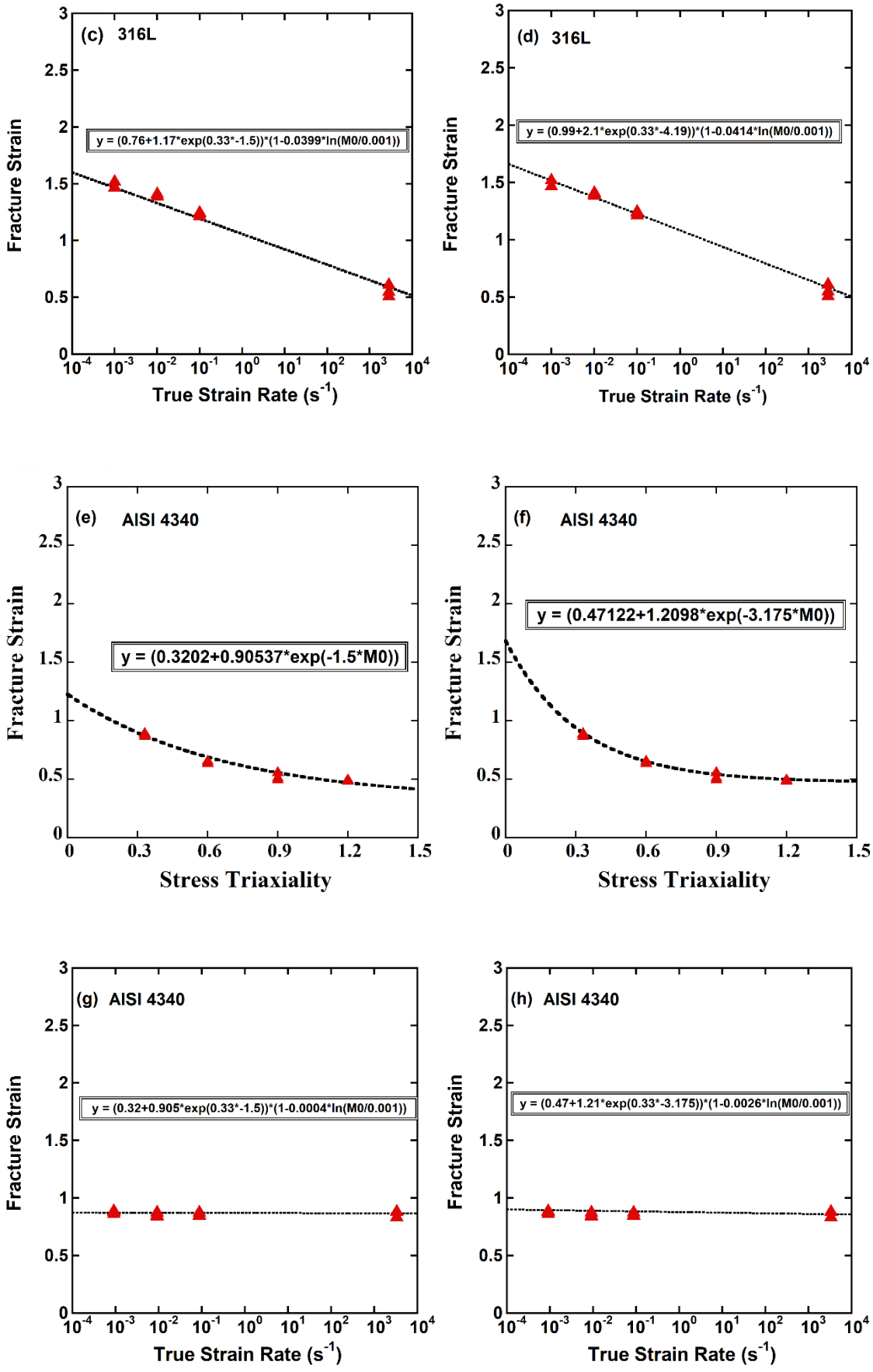

Figure 5.41 (cont.)

Finally, a comparison of experimentally determine JC flow stress and damage model parameters of 316L and AISI 4340 with the ones determined by the used code are shown in Figures 5.42 and Figure 5.43, respectively. The code found parameters are seen in the same figures approach well with those of experimentally determined values. This further proves the capability of the code in predicting the JC parameters.

	Experimental Results of JC Strength Model Parameters For 316L				Program Results of JC Strength Model Parameters For 316L					
	A (MPa)	B (MPa)	n	C	A (MPa)	B (MPa)	n	C	m	$\dot{\varepsilon}_0$ (s^{-1})
Tension Direct Fitting	580	1025.77	0.86	0.019491	582.9764	1022.418	0.8782	0.019439	-	10^{-3}
Average True Stress Values	479.7	992.15	0.62849	0.019491	454.53	1005.3	0.59425	0.019439	-	10^{-3}
Equivalent Stress Values [Bridgman]	479.7	863.15	0.51458	0.019191	454.53	833.53	0.49425	0.019439	-	10^{-3}
Equivalent Stress Values [MLR]	479.7	837.06	0.48364	0.019491	454.53	847.81	0.45347	0.019439	-	10^{-3}

JC Damage Model Parameters For 316L

	D_1	D_2	D_3	D_4	D_5
Experimental Results	0.76	1.17	-1.5	-0.0393	-
	0.992	2.1	-4.19	-0.0413	-
Program Results	0.7601	1.1704	-1.5	-0.0399	-
	0.99203	2.10198	-4.19385	-0.0414	-

Figure 5.42. A comparison of experimentally determine JC flow stress and damage model parameters of 316L with the ones determined by the used code

	Experimental Results of JC Strength Model Parameters For AISI 4340				Program Results of JC Strength Model Parameters For AISI 4340					
	A (MPa)	B (MPa)	n	C	A (MPa)	B (MPa)	n	C	m	$\dot{\varepsilon}_0$ (s^{-1})
Tension Direct Fitting	460	815	0.38	0.01315	504.86	756.6	0.44756	0.01351	-	10^{-3}
Average True Stress Values	549.99	650.68	0.47396	0.01315	550.58	646.87	0.46688	0.01351	-	10^{-3}
Equivalent Stress Values [Bridgman]	549.99	437.46	0.31476	0.01315	550.58	538.78	0.39519	0.01315	-	10^{-3}
Equivalent Stress Values [MLR]	549.99	537.23	0.37032	0.01315	550.58	530.84	0.35709	0.01315	-	10^{-3}

JC Damage Model Parameters For AISI 4340

	D_1	D_2	D_3	D_4	D_5
Experimental Results	0.32022	0.90539	-1.5	-0.00036	-
	0.47124	1.21	-3.1763	-0.00253	-
Program Results	0.32	0.905	-1.5	-0.0004	-
	0.471	1.21	-3.175	-0.0026	-

Figure 5.43. A comparison of experimentally determine JC flow stress and damage model parameters of AISI with the ones determined by the used code

CHAPTER 6

CONCLUSIONS

In this thesis, a comprehensive methodology has been investigated in order to improve the accuracy and reliability of finite element models used to predict the response of structures under external loadings. The key objective was to minimize the variations and errors introduced during the experimental data processing stage, particularly in determining material model parameters for flow stress and damage models. The developed computer code successfully automates the calculation of Bridgman's correction factor, equivalent stress-strain curves, and JC flow stress and damage model parameters. By automating these processes, we have significantly reduced the extent of human error, ensuring more consistent and accurate results. The integration of a library of JC parameters for common engineering materials further enhances the utility and applicability of the code. The experimental validation was conducted on 316L and AISI 4340 alloys, demonstrating the effectiveness of the developed methodology. The code's accuracy in predicting equivalent stress-strain curves and model parameters was verified against experimental data, showing a high degree of reliability. The results further indicate that the automation of data processing in material parameter determination is not only feasible but also beneficial in achieving more precise finite element model predictions. This advancement holds significant potential for improving the design and analysis of structures in engineering applications.

As future work, the code's applicability could be expanded to a wider range of materials and constitutive equations, further enhancing its variability and impact. Additionally, incorporating more advanced image analysis techniques and machine learning algorithms could refine the accuracy of measurements and parameter estimations even further. Overall, this thesis contributes a valuable tool for the engineering community, facilitating more accurate and efficient material modeling and structural analysis.

REFERENCES

1. ASTM, E8/E8M− 15a. In *Standard test Methods for Tension Testing of Metallic Materials,* 2015.

2. Świłło, S.; Cacko, R., A New Approach for Evaluation True Stress–Strain Curve from Tensile Specimens for DC04 Steel with Vision Measurement in the Post-Necking Phases. *Materials* **2023,** *16* (2), 558.

3. Mondal, C.; Podder, B.; Ramesh Kumar, K.; Yadav, D., Constitutive description of tensile flow behavior of cold flow-formed AFNOR 15CDV6 steel at different deformation levels. *Journal of materials engineering and performance* **2014,** *23*, 3586-3599.

4. Eraslan, A. N., Inelastic deformations of rotating variable thickness solid disks by Tresca and von Mises criteria. *International Journal of Computational Engineering Science* **2002,** *3* (01), 89-101.

5. Bridgman, P., The stress distribution at the neck of a tension specimen. *Trans. ASM* **1944,** *32*, 553-574.

6. Mirone, G.; Corallo, D., A local viewpoint for evaluating the influence of stress triaxiality and Lode angle on ductile failure and hardening. *International Journal of Plasticity* **2010,** *26* (3), 348-371.

7. Shield, R., On the plastic flow of metals under conditions of axial symmetry. *Proceedings of the Royal Society of London. Series A. Mathematical and Physical Sciences* **1955,** *233* (1193), 267-287.

8. Murata, M.; Yoshida, Y.; Nishiwaki, T., Stress correction method for flow stress identification by tensile test using notched round bar. *Journal of Materials Processing Technology* **2018,** *251*, 65-72.

9. La Rosa, G.; Risitano, A.; Mirone, G., Postnecking elastoplastic characterization: degree of approximation in the Bridgman method and properties of the flow-stress/true-stress ratio. *Metallurgical and Materials Transactions A* **2003,** *34*, 615-624.

10. Mirone, G., A new model for the elastoplastic characterization and the stress–strain determination on the necking section of a tensile specimen. *International Journal of Solids and Structures* **2004,** *41* (13), 3545-3564.

11. Hancock, J.; Brown, D., On the role of strain and stress state in ductile failure. *Journal of the Mechanics and Physics of Solids* **1983,** *31* (1), 1-24.

12. Mirone, G., Approximate model of the necking behaviour and application to the void growth prediction. *International Journal of Damage Mechanics* **2004,** *13* (3), 241-261.

13. Mirone, G.; Corallo, D.; Barbagallo, R., Experimental issues in tensile Hopkinson bar testing and a model of dynamic hardening. *International Journal of Impact Engineering* **2017,** *103*, 180-194.

14. Mirone, G.; Barbagallo, R.; Giudice, F., Locking of the strain rate effect in Hopkinson bar testing of a mild steel. *International Journal of Impact Engineering* **2019,** *130*, 97-112.

15. Yao, Z.; Wang, W., Full-range strain-hardening behavior of structural steels: Experimental identification and numerical simulation. *Journal of Constructional Steel Research* **2022,** *194*, 107329.

16. Versaillot, P. D.; Wu, Y.-F.; Zhao, Z.-L., Experimental study on the evolution of necking zones of metallic materials. *International Journal of Mechanical Sciences* **2021,** *189*, 106002.

17. Meyers, M. A., *Dynamic behavior of materials*. John wiley & sons: 1994.
18. Langrand, B.; Geoffroy, P.; Petitniot, J.-L.; Fabis, J.; Markiewicz, E.; Drazetic, P., Identification technique of constitutive model parameters for crashworthiness modelling. *Aerospace Science and Technology* **1999,** *3* (4), 215-227.

19. Johnson G, R., A Constitutive Model and Data for Metals Subjected to Large Strains, High Strain Rates and High Temperatures. *Presented at the Seventh International Symposium on Ballistics, The Hague, The Netherlands, April, 1983* **1983**.

20. Zerilli, F. J.; Armstrong, R. W., Dislocation‐mechanics‐based constitutive relations for material dynamics calculations. *Journal of applied physics* **1987,** *61* (5), 1816-1825.

21. Noble, J.; Goldthorpe, B.; Church, P.; Harding, J., The use of the Hopkinson bar to validate constitutive relations at high rates of strain. *Journal of the Mechanics and Physics of Solids* **1999,** *47* (5), 1187-1206.

22. Kay, G., *Failure modeling of titanium 6AI-4V and aluminum 2024-T3 with the Johnson-Cook material model*. Office of Aviation Research, Federal Aviation Administration: 2003.

23. Nemat-Nasser, S.; Guo, W.-G., Thermomechanical response of DH-36 structural steel over a wide range of strain rates and temperatures. *Mechanics of materials* **2003,** *35* (11), 1023-1047.

24. Klepaczko, J. R.; Rusinek, A.; Rodríguez-Martínez, J. A.; Pęcherski, R.; Arias, A., Modelling of thermo-viscoplastic behaviour of DH-36 and Weldox 460-E structural steels at wide ranges of strain rates and temperatures, comparison of constitutive relations for impact problems. *Mechanics of Materials* **2009,** *41* (5), 599-621.

25. Scapin, M.; Peroni, L.; Peroni, M., Parameters identification in strain-rate and thermal sensitive visco-plastic material model for an alumina dispersion strengthened copper. *International Journal of Impact Engineering* **2012,** *40*, 58-67.

26. Deb, S.; Muraleedharan, A.; Immanuel, R.; Panigrahi, S.; Racineux, G.; Marya, S., Establishing flow stress behaviour of Ti-6Al-4V alloy and development of constitutive models using Johnson-Cook method and Artificial Neural Network for quasi-static and dynamic loading. *Theoretical and Applied Fracture Mechanics* **2022,** *119*, 103338.

27. Jaspers, S.; Dautzenberg, J., Material behaviour in conditions similar to metal cutting: flow stress in the primary shear zone. *Journal of Materials Processing Technology* **2002,** *122* (2-3), 322-330.

28. Lee, W.-S.; Lin, C.-F., High-temperature deformation behaviour of Ti6Al4V alloy evaluated by high strain-rate compression tests. *Journal of Materials Processing Technology* **1998,** *75* (1-3), 127-136.

29. Lee, W.-S.; Lin, C.-F., Plastic deformation and fracture behaviour of Ti–6Al–4V alloy loaded with high strain rate under various temperatures. *Materials Science and Engineering: A* **1998,** *241* (1-2), 48-59.

30. Manes, A.; Peroni, L.; Scapin, M.; Giglio, M., Analysis of strain rate behavior of an Al 6061 T6 alloy. *Procedia Engineering* **2011,** *10*, 3477-3482.

31. Banerjee, A.; Dhar, S.; Acharyya, S.; Datta, D.; Nayak, N., Determination of Johnson cook material and failure model constants and numerical modelling of Charpy impact test of armour steel. *Materials Science and Engineering: A* **2015,** *640*, 200-209.

32. Grązka, M.; Janiszewski, J.; Kruszka, L.; Cadoni, E.; Forni, D.; Riganti, G., Identification methods of parameters for Johnson-Cook constitutive equation–comparison. *Applied Mechanics and Materials* **2014,** *566*, 97-103.

33. Meyer Jr, H. W.; Kleponis, D. S., Modeling the high strain rate behavior of titanium undergoing ballistic impact and penetration. *International Journal of Impact Engineering* **2001,** *26* (1-10), 509-521.

34. Seo, S.; Min, O.; Yang, H., Constitutive equation for Ti–6Al–4V at high temperatures measured using the SHPB technique. *International journal of impact engineering* **2005,** *31* (6), 735-754.

35. Kotkunde, N.; Deole, A. D.; Gupta, A. K.; Singh, S. K., Comparative study of constitutive modeling for Ti–6Al–4V alloy at low strain rates and elevated temperatures. *Materials & Design* **2014,** *55*, 999-1005.

36. Wang, F.; Zhao, J.; Zhu, N.; Li, Z., A comparative study on Johnson–Cook constitutive modeling for Ti–6Al–4V alloy using automated ball indentation (ABI) technique. *Journal of Alloys and Compounds* **2015,** *633*, 220-228.

37. Johnson, G. R.; Cook, W. H., Fracture characteristics of three metals subjected to various strains, strain rates, temperatures and pressures. *Engineering fracture mechanics* **1985,** *21* (1), 31-48.

38. Chen, G.; Ren, C.; Yang, X.; Jin, X.; Guo, T., Finite element simulation of high-speed machining of titanium alloy (Ti–6Al–4V) based on ductile failure model. *The International Journal of Advanced Manufacturing Technology* **2011,** *56*, 1027-1038.

39. Liu, J.; Bai, Y.; Xu, C., Evaluation of ductile fracture models in finite element simulation of metal cutting processes. *Journal of Manufacturing Science and Engineering* **2014,** *136* (1), 011010.

40. Rice, J. R.; Tracey, D. M., On the ductile enlargement of voids in triaxial stress fields∗. *Journal of the Mechanics and Physics of Solids* **1969,** *17* (3), 201-217.

41. Majzoobi, G.; Dehgolan, F. R., Determination of the constants of damage models. *Procedia Engineering* **2011,** *10*, 764-773.

42. Džugan, J.; Španiel, M.; Prantl, A.; Konopík, P.; Růžička, J.; Kuželka, J., Identification of ductile damage parameters for pressure vessel steel. *Nuclear Engineering and Design* **2018,** *328*, 372-380.

43. Zhang, X.; Wu, S.; Wang, H.; Liu, C. R., Predicting the effects of cutting parameters and tool geometry on hard turning process using finite element method. **2011**.

44. Buzyurkin, A.; Gladky, I.; Kraus, E., Determination and verification of Johnson–Cook model parameters at high-speed deformation of titanium alloys. *Aerospace science and technology* **2015,** *45*, 121-127.

45. Lesuer, D. R. *EXPERIMENTAL INVESTIGATIONS OF MATERIAL MODELS FOR TI-6A1-4V TITANIUM AND 2024-T3 ALUMINUM*; 2000.

46. Khan, A. S.; Suh, Y. S.; Kazmi, R., Quasi-static and dynamic loading responses and constitutive modeling of titanium alloys. *International journal of plasticity* **2004,** *20* (12), 2233-2248.

47. Calamaz, M.; Coupard, D.; Girot, F., A new material model for 2D numerical simulation of serrated chip formation when machining titanium alloy Ti–6Al–4V. *International Journal of Machine Tools and Manufacture* **2008,** *48* (3-4), 275-288.

48. Özel, T.; Karpat, Y., Identification of constitutive material model parameters for high-strain rate metal cutting conditions using evolutionary computational algorithms. *Materials and manufacturing processes* **2007,** *22* (5), 659-667.

49. Dorogoy, A.; Rittel, D., Determination of the Johnson–Cook material parameters using the SCS specimen. *Experimental mechanics* **2009,** *49*, 881-885.

50. Dumitrescu, M.; Elbestawi, M.; El-Wardany, T., Mist coolant applications in high speed machining of advanced materials. *Metal cutting and high speed machining* **2002**, 329-339.

51. Dabboussi, W.; Nemes, J., Modeling of ductile fracture using the dynamic punch test. *International journal of mechanical sciences* **2005,** *47* (8), 1282-1299.

52. Raut, N.; Shinde, S.; Yakkundi, V., Determination of Johnson Cook parameters for Ti-6Al-4 V Grade 5 experimentally by using three different methods. *Materials Today: Proceedings* **2021,** *44*, 1653-1658.

53. Pittalà, G.; Monno, M., A new approach to the prediction of temperature of the workpiece of face milling operations of Ti-6Al-4V. *Applied Thermal Engineering* **2011,** *31* (2-3), 173-180.

54. Guo, X.; Heuzé, T.; Othman, R.; Racineux, G., Inverse Identification at Very High Strain Rate of the Johnson‐Cook Constitutive Model on the Ti‐6Al‐4 V Alloy With a Specially Designed Direct‐impact Kolsky Bar Device. *Strain* **2014,** *50* (6), 527-538.

55. Tao, Z.-j.; Fan, X.-g.; He, Y.; Jun, M.; Heng, L., A modified Johnson–Cook model for NC warm bending of large diameter thin-walled Ti–6Al–4V tube in wide ranges of strain rates and temperatures. *Transactions of Nonferrous Metals Society of China* **2018,** *28* (2), 298-308.

56. Hammer, J. T. Plastic deformation and ductile fracture of Ti-6Al-4V under various loading conditions. The Ohio State University, 2012.

57. Huang, J.; Guo, Y.; Qin, D.; Zhou, Z.; Li, D.; Li, Y., Influence of stress triaxiality on the failure behavior of Ti-6Al-4V alloy under a broad range of strain rates. *Theoretical and Applied Fracture Mechanics* **2018,** *97*, 48-61.

58. Wang, C.; Suo, T.; Li, Y.; Xue, P.; Tang, Z., A new experimental and numerical framework for determining of revised JC failure parameters. *Metals* **2018,** *8* (6), 396.

59. Perosanz, S.; Viscasillas, M.; Piris, N. M.; Hokka, M.; Barba, D. In *On the effect of the microstructure on the dynamic behaviour of Ti-6Al-4V*, EPJ Web of Conferences, EDP Sciences: 2021; p 02013.

60. Verleysen, P.; Peirs, J., Quasi-static and high strain rate fracture behaviour of Ti6Al4V. *International Journal of Impact Engineering* **2017,** *108*, 370-388.

61. Harzallah, M.; Pottier, T.; Senatore, J.; Mousseigne, M.; Germain, G.; Landon, Y., Numerical and experimental investigations of Ti-6Al-4V chip generation and thermo-mechanical couplings in orthogonal cutting. *International Journal of Mechanical Sciences* **2017,** *134*, 189-202.

62. Lin, B.; Lupton, C.; Spanrad, S.; Schofield, J.; Tong, J., Fatigue crack growth in laser-shock-peened Ti–6Al–4V aerofoil specimens due to foreign object damage. *International Journal of Fatigue* **2014,** *59*, 23-33.

63. Chen, G.; Ren, C.; Qin, X.; Li, J., Temperature dependent work hardening in Ti–6Al–4V alloy over large temperature and strain rate ranges: Experiments and constitutive modeling. *Materials & Design* **2015,** *83*, 598-610.

64. Wu, H. M.; Shu, Y. M., Stress-stain response of PVC geomembrane under uniaxial tension test. *Advanced Materials Research* **2014,** *936*, 1582-1586.

65. Wu, S.; Zhou, C.; Shi, Y.; Hu, A.; Xiao, X., Plasticity, ductile fracture and ballistic impact behavior of Ti-6Al-4V Alloy. *International Journal of Impact Engineering* **2023,** *174*, 104493.

66. Yang, S.; Xu, J.; Fu, Y.; Wei, W., Finite element modeling of machining of hydrogenated Ti-6Al-4V alloy. *The International Journal of Advanced Manufacturing Technology* **2012,** *59*, 253-261.

67. Hu, H.; Xu, Z.; Dou, W.; Huang, F., Effects of strain rate and stress state on mechanical properties of Ti-6Al-4V alloy. *International Journal of Impact Engineering* **2020,** *145*, 103689.

68. Yatnalkar, R. S. Experimental investigation of plastic deformation of Ti-6Al-4V under various loading conditions. The Ohio state university, 2010.

69. Perez, J. A.; Eguía, V. M.; Sobrino, J. C.; Martínez, A. M., Experimental results and constitutive model of the mechanical behavior of Ti6Al4V alloy at high temperature. *Procedia Manufacturing* **2019,** *41*, 723-730.

70. Peng, Y.-Q.; Jia, D.; Wang, L.-B.; Wei, L.-M., Determination of the tensile and fracture properties of ductile materials by small punch testing. *Journal of Nuclear Science and Technology* **2021,** *58* (7), 735-743.

71. Karkalos, N. E.; Markopoulos, A. P., Determination of Johnson-Cook material model parameters by an optimization approach using the fireworks algorithm. *Procedia Manufacturing* **2018,** *22*, 107-113.

72. Chandrasekaran, H.; M'saoubi, R.; Chazal, H., Modelling of material flow stress in chip formation process from orthogonal milling and split Hopkinson bar tests. *Machine Science and Technology* **2005,** *9* (1), 131-145.

73. Umbrello, D.; M'saoubi, R.; Outeiro, J., The influence of Johnson–Cook material constants on finite element simulation of machining of AISI 316L steel. *International Journal of Machine Tools and Manufacture* **2007,** *47* (3-4), 462-470.

74. Tounsi, N.; Vincenti, J.; Otho, A.; Elbestawi, M., From the basic mechanics of orthogonal metal cutting toward the identification of the constitutive equation. *International Journal of Machine Tools and Manufacture* **2002,** *42* (12), 1373-1383.

75. Tamer, Y.; Toros, S.; Ozturk, F., Numerical and Experimental Comparison of Fractural Characteristics of 316L Stainless Steel. *Journal of Materials Engineering and Performance* **2023,** *32* (3), 1103-1118.

76. Li, Y.; Ge, Y.; Lei, J.; Bai, W., Mechanical Properties and Constitutive Model of Selective Laser Melting 316L Stainless Steel at Different Scanning Speeds. *Advances in Materials Science and Engineering* **2022,** *2022*.

77. Svoboda, A.; Wedberg, D.; Lindgren, L.-E., Simulation of metal cutting using a physically based plasticity model. *Modelling and Simulation in Materials Science and Engineering* **2010,** *18* (7), 075005.

78. Dharavath, B.; Morchhale, A.; Singh, S. K.; Kotkunde, N.; Naik, M., Experimental determination and theoretical prediction of limiting strains for ASS 316L at hot forming conditions. *Journal of Materials Engineering and Performance* **2020,** *29*, 4766-4778.

79. Klocke, F.; Lung, D.; Buchkremer, S.; Jawahir, I., From orthogonal cutting experiments towards easy-to-implement and accurate flow stress data. *Materials and manufacturing processes* **2013,** *28* (11), 1222-1227.

80. Yang, Z.; Yu, Y.; Wei, Y.; Huang, C., Crushing behavior of a thin-walled circular tube with internal gradient grooves fabricated by SLM 3D printing. *Thin-Walled Structures* **2017,** *111*, 1-8.

81. Liu, S.; Wang, B.; Li, W.; Liu, J., Investigation of cold drawing process of thin-walled ribbed steel tube. *Journal of Manufacturing Processes* **2021,** *70*, 376-388.

82. Alkhatib, S. E.; Xu, S.; Lu, G.; Karrech, A.; Sercombe, T. B., Dynamic constitutive behavior of LPBFed metal alloys. *Journal of Materials Research and Technology* **2023**.

83. Flores-Johnson, E.; Muránsky, O.; Hamelin, C.; Bendeich, P.; Edwards, L., Numerical analysis of the effect of weld-induced residual stress and plastic damage on the ballistic performance of welded steel plate. *Computational Materials Science* **2012,** *58*, 131-139.

84. Benmeddour, A., Experimental Investigation and Numerical Prediction of the Effects of Cutting Tool Geometry During Turning of AISI 316L Steel. *Periodica Polytechnica Mechanical Engineering* **2021,** *65* (4), 293-301.

85. Wang, L.; Wang, Z.; Zhang, S.; Lin, Y.; Fu, M.; Sun, C., Spiral metal tube multi-roller bending springback prediction model based on dynamic deformation enhancement analysis. *International Journal of Solids and Structures* **2022,** *254*, 111940.

86. Meng, J.; He, G., Predict the flow stress of the hardness for AISI 4340. *The International Journal of Advanced Manufacturing Technology* **2020,** *111*, 2499-2506.

87. Lee, W.-S.; Yeh, G.-W., The plastic deformation behaviour of AISI 4340 alloy steel subjected to high temperature and high strain rate loading conditions. *Journal of materials processing technology* **1997,** *71* (2), 224-234.

88. Sulaiman, S.; Roshan, A.; Ariffin, M. In *Finite Element Modelling of the effect of tool rake angle on tool temperature and cutting force during high speed machining of AISI 4340 steel*, IOP Conference Series: Materials Science and Engineering, IOP Publishing: 2013; p 012040.

89. Gopikrishnan, P.; Akbar, A.; Asokan, A.; Bhaskar, B.; Sumesh, C., Numerical modelling and optimization of surface finish during peripheral milling of AISI 4340 steel using RSM. *Materials Today: Proceedings* **2018,** *5* (11), 24612-24621.

90. Rule, W. K., A numerical scheme for extracting strength model coefficients from Taylor test data. *International journal of impact engineering* **1997,** *19* (9-10), 797-810.

91. Ning, J.; Liang, S. Y., Evaluation of an analytical model in the prediction of machining temperature of AISI 1045 steel and AISI 4340 steel. *Journal of Manufacturing and Materials Processing* **2018,** *2* (4), 74.

92. Joo, J. H.; Lee, C. H.; Choi, J. H. In *A Numerical Research on the Penetration into a Semi-Infinite Rolled Homogeneous Armor by a Medium-Caliber Kinetic Energy Projectile*, Materials Science Forum, Trans Tech Publ: 2011; pp 197-202.

93. Sattouf, C.; Pantalé, O.; Caperaa, S., A methodology for the identification of constitutive and contact laws of metallic materials under High Strain Rates. *Advances in Mechanical Behaviour, Plasticity and Damage; Elsevier: Tours, France* **2000**, 621-626.

94. Goh, W.; Zheng, Y.; Yuan, J.; Ng, K., Effects of hardness of steel on ceramic armour module against long rod impact. *International Journal of Impact Engineering* **2017,** *109*, 419-426.

95. Chen, G.; Ren, C.; Lu, L.; Ke, Z.; Qin, X.; Ge, X., Determination of ductile damage behaviors of high strain rate compression deformation for Ti-6Al-4V alloy using experimental-numerical combined approach. *Engineering Fracture Mechanics* **2018,** *200*, 499-520.

96. Bobbili, R.; Madhu, V., Flow and fracture characteristics of near alpha titanium alloy. *Journal of Alloys and Compounds* **2016,** *684*, 162-170.

97. Chen, M. Research on Mechanical properties test and dynamic material model of Ti6Al4V titanium alloy. Nanjing University of Aeronautics and Astronautics Nanjing, China, 2012.

98. Sancho, R.; Galvez, F.; Garrido, C.; Perosanz-Amarillo, S.; Barba, D. In *On the mechanical behaviour of additively manufactured metamaterials under dynamic conditions*, EPJ Web of Conferences, EDP Sciences: 2021; p 05006.

99. Benson, D. J., A mixture theory for contact in multi-material Eulerian formulations. *Computer methods in applied mechanics and engineering* **1997,** *140* (1-2), 59-86.

100. Lau, S. S.; Ranji, S.; Mukherjee, A. K.; Thomas, G.; Dorn, J. E., Dislocation mechanisms in single crystals of tantalum and molybdenum at low temperatures. *Acta Metallurgica* **1967,** *15* (2), 237-244.

101. Klepaczko, J., Thermally activated flow and strain rate history effects for some polycrystalline FCC metals. *Materials Science and Engineering* **1975,** *18* (1), 121-135.

102. Mukherjee, A.; Mote, J.; Dorn, J., Strain hardening of single aluminum crystals during polyslip. **1965**.

103. Xue, Q.; Meyers, M.; Nesterenko, V., Self-organization of shear bands in titanium and Ti–6Al–4V alloy. *Acta materialia* **2002,** *50* (3), 575-596.

104. Zerilli, F. J.; Armstrong, R. W., Description of tantalum deformation behavior by dislocation mechanics based constitutive relations. *Journal of Applied Physics* **1990,** *68* (4), 1580-1591.

105. Zerilli, F.; Armstrong, R., Dislocation mechanics based analysis of material dynamics behavior: enhanced ductility, deformation twinning, shock deformation, shear instability, dynamic recovery. *Le Journal de Physique IV* **1997,** *7* (C3), C3-637-C3-642.

106. Harding, J. In *The development of constitutive relationship for material behaviour at high rates of strain*, Conference series-Institute of physics, 1989; pp 189-203.

107. Holmquist, T.; Johnson, G., Determination of constants and comparison of results for various constitutive models. *Le Journal de Physique IV* **1991,** *1* (C3), C3-853-C3-860.

108. Cowper, G. R.; Symonds, P. S. In *STRAIN-HARDENING AND STRAIN-RATE EFFECTS IN THE IMPACT LOADING OF CANTILEVER BEAMS*, 1957.

109. Škrlec, A.; Klemenc, J., Estimating the strain-rate-dependent parameters of the Cowper-Symonds and Johnson-Cook material models using Taguchi Arrays. *Strojniški vestnik-Journal of Mechanical Engineering* **2016,** *62* (4), 220-230.

110. Huh, H.; Kang, W., Crash-worthiness assessment of thin-walled structures with the high-strength steel sheet. *International Journal of Vehicle Design* **2002,** *30* (1-2), 1-21.

111. Allen, D.; Rule, W.; Jones, S., Optimizing material strength constants numerically extracted from Taylor impact data. *Experimental mechanics* **1997,** *37*, 333-338.

112. Liu, W.; Lin, Y.; Meng, Z.; Li, J.; Huang, S. In *Constitutive model and forming limit prediction of AA5182-O aluminium alloy sheet in electromagnetic forming*, IOP Conference Series: Materials Science and Engineering, IOP Publishing: 2022; p 012047.

113. Sarıkaya, M. K., The development of constitutive equations of polycarbonate and modeling the impact behavior. **2023**.